μSR and AC Susceptibility as a probe of Frustrated Pyrochlore Magnets and Type-1 Superconductivity

Muon Spin Rotation, Relaxation, and Resonance, and AC Susceptibility as a probe of Frustrated Pyrochlore Magnets and Type-I Superconductivity

By James Beare, B.Sc., M.Sc.

A Thesis Submitted to the School of Graduate Studies in the Partial Fulfillment of the Requirements for the Degree Ph.D. Thesis

McMaster University
Ph.D. Thesis (2021)
Hamilton, Ontario (Physics and Astronomy)

TITLE: Muon Spin Rotation, Relaxation, and Resonance, and AC Susceptibility as a probe of Frustrated Pyrochlore Magnets and Type-I Superconductivity
AUTHOR: James Beare (McMaster University)
SUPERVISOR: Dr. Graeme Luke
NUMBER OF PAGES: xii, 118

Abstract

In this thesis, we use Muon Spin Rotation, Relaxation, and Resonance (μSR) as a probe for three frustrated pyrochlore systems; Gd_2ScNbO_7 (GSNO), Nd_2ScNbO_7 (NSNO) and $Sm_2Ti_2O_7$ (STO), as well as the type-I superconductor BeAu. We grew all of the pyrochlore samples at McMaster using the Optical Floating Zone method. We make use of Direct Current (DC) and Alternating Current (AC) susceptibility, powder x-ray diffraction and Laue x-ray diffraction to characterize our samples. We make use of AC susceptibility measurements to explore the dynamics of the classical spin-ice $Dy_2Ti_2O_7$ (DTO) and find that the system acts as a supercooled magnetic liquid, analogous to glass-forming dielectric liquids. We find GSNO is a dense spin-glass based on our μSR and AC susceptibility measurements. NSNO is a moment fragmentation candidate where spin-ice, as well as all-in all-out magnetic ordering, are observed simultaneously. Our μSR measurements on this material show a strong similarity to another moment fragmentation candidate, $Nd_2Zr_2O_7$, suggesting NSNO may be in a similar state. STO is a closely related compound that fully orders into a magnetic state which we study using μSR. We find subtle evidence of this magnetic transition along with persistent spin dynamics which we suggest has a common, but as of yet unexplained, origin as other frustrated pyrochlores measured in μSR. Finally, we use μSR to measure the temperature dependence of the critical field in the type-I superconductor BeAu. Using an ellipsoid of BeAu and a pressure cell, we study the magnetic properties of the sample under pressure.

Acknowledgements

First I would like to acknowledge and thank my family for their support over my Ph.D.; Mom, Dad, Tina, Chris, Maddie, Angela, Giacamo, Ava, Filip, Joe, and Liz. Without you, this would not have been possible.

I have benefited tremendously from working with research scientists, technicians, and laboratory managers at both McMaster and TRIUMF. The guidance I have received and the knowledge in material science I have gained from our lab managers, Hanna Dabkowska and Casey Marjerrison, cannot be overstated. Paul Dube has provided enormous assistance with the operation of the SQUID over the years and has always provided good advice in solving any technical issue. At TRIUMF, the technical support of Bhassam Hitti, Donald Arseneau, Iain McKenzie, Rahim Abasalti, Deepak Vyas, and Syd Kreitzman has been terrific. Kenji Kojima and Gerald Morris, in addition to providing technical support, have provided invaluable scientific discussion. Last, but certainly not least, I must thank Sarah Dunsiger for the immeasurable support she has provided the McMaster group with. While many of the TRIUMF support staff have gone above and beyond the call of duty, Sarah has been instrumental in ensuring many of our experiments are performed at the highest level. I would like to thank all of these people for their service, discussion, and transfer of knowledge.

I have had the pleasure of collaborating with many great undergraduate and graduate students during my time at McMaster. In particular, Yipeng Cai, Melissa Henderson, Sudarshan Sharma, Evan Smith, and Murray Wilson have contributed greatly to my research projects.

I would like to thank my committee members, Professors Bruce Gaulin and Takashi Imai, for the guidance they have provided during my Ph.D. In addition, I have benefited tremendously from collaborations and interactions with Professors Patrick Clancy, John Greedan, Alannah Hallas, and Yasutomo Uemura.

Lastly, I would like to thank my supervisor, Professor Graeme Luke, for the guidance they have provided during my Ph.D. Their knowledge and experience have proved invaluable in shaping me into a scientist.

Contents

List of Figures

List of Tables

Declaration of Authorship

I, James Beare, declare that this thesis titled, "Muon Spin Rotation, Relaxation, and Resonance, and AC Susceptibility as a probe of Frustrated Pyrochlore Magnets and Type-I Superconductivity" and the work presented in it are my own. I confirm that:

This thesis is an original report of my research, has been written by me, and has not been submitted for any previous degree. I have been a major contributor to all of the experimental work, except where noted, and collaborative contributions have been indicated clearly and acknowledged below. Due references have been provided on all supporting literature and resources. Specifically, I performed all bulk measurements and analysis except where noted below. I grew all samples with assistance from those noted below. I participated in all μSR experiments with guidance from G. Luke in all experiments. B. Hitti, D. Arseneau, and G. Morris provided additional technical support at TRIUMF for all experiments.

Chapter 3 presents the results of measurements on Gd_2ScNbO_7. A. Kayssi and C. Marjerisson participated and assisted in the growth of this material. μSR measurements presented in this thesis were performed with assistance from M. Nugent, M. Rutherford and S. Sharma with guidance from S. Dunsiger.

The results of measurements on Nd_2ScNbO_7 are presented in chapter 4. Single crystals of this sample were grown in collaboration with G. Johnstone, N. Platti, and C. Marjerrison. μSR measurements presented in this thesis were performed with assistance from M. Feig, M. Nugent, M. Rutherford, and S. Sharma with guidance from S. Dunsiger.

Chapter 5 presents the results of measurements on $Sm_2Ti_2O_7$. μSR measurements presented in this thesis were performed with assistance from M. Nugent, M. Rutherford, S. Sharma, and G. Zhao with guidance from S. Dunsiger.

Chapter 6 presents the results of measurements on $Dy_2Ti_2O_7$. Paul Dube assisted with the AC susceptibility measurements and provided technical support for these measurements. Three of the single crystals were grown by myself and the O_2 grown sphere by A. Ghukasyan and H. Dabkowska.

As chapter 7, this thesis includes the published manuscript "μSR and Magnetometry Study of the Type-I Superconductor BeAu" [8]. For this work, I wrote the manuscript, performed all data analysis, and performed SQUID measurements at ambient and high pressure in collaboration with P. Dube and M. Nugent. I lead the μSR experiment in collaboration with M. Wilson with guidance from G. Luke and E. Svanidze, while Y. Cai, Z.Gong, S.L. Guo, Z. Guguchia, T.J.S. Munsie, and Y.J. Uemura assisted in running the experiment. A. Amon, A. Leithe-Jasper, Y. Grin, and E. Svanidze provided the samples for the experiments and collaborated in publishing the manuscript.

For my parents

Chapter 1

Theory and Background

1.1 Introduction

This thesis is broadly divided into two separate topics; frustrated magnetism and superconductivity. In this chapter, we will review relevant material for both subjects starting with frustrated magnetism. Pyrochlores offer a rich playground for the exploration of frustrated magnetism and we will review important experimental and theoretical aspects for various pyrochlore materials here. We will also examine some aspects of superconductivity with a focus on demagnetization effects in Type-I superconductivity.

1.2 Magnetism in Condensed Matter

Magnetism of all types requires the presence of magnetic moments, $\vec{\mu}$. Electronic moments arise from the angular momentum of ions with unpaired electrons while nuclear moments arise from the protons and neutrons within a nucleus. Spin, $\vec{S}$, and orbital, $\vec{L}$, angular momenta combine to give the total angular momentum operator $\vec{J} = \vec{S} + \vec{L}$. The total angular momentum is given by $\vec{G} = \hbar\vec{J}$, with magnitude,

$$G = \sqrt{J\left(J+1\right)}\hbar, \tag{1.1}$$

where J can take values, $J = \left(L-S\right), \left(L-S+1\right) ... \left(L+S\right)$. In general, $\vec{L}$ and $\vec{S}$ are not individually conserved due to spin-orbit coupling but their sum, $\vec{J}$, is conserved. The magnetic moment induced by the angular momentum of a magnetic ion is given by,

$$\vec{\mu} = -g_L\mu_B\vec{G}, \tag{1.2}$$

where $\mu_B = \frac{\hbar e}{2m_e c}$ is the Bohr magneton and $g_L = \frac{3}{2} + \frac{S(S+1)-L(L+1)}{2J(J+1)}$ is the Landé g-factor. We will now examine some general aspects of magnetism in materials.

Materials that have full electron shells are often diamagnetic (repelled by a magnetic field), although metals will have a contribution from conduction electrons that is paramagnetic (attracted by a magnetic field). Both of these contributions are roughly

temperature independent and for this reason, materials exhibiting only (temperature-independent) diamagnetism or paramagnetism are referred to as nonmagnetic. Insulating materials with partially filled shells usually exhibit either ferromagnetism, where nearest neighbour moments tend to align, or antiferromagnetism, where nearest neighbours tend to anti-align. To build a picture of conventional magnets for localised electrons we will examine the nearest neighbour Heisenberg Hamiltonian,

$$\mathbf{H} = -2J^{ex} \sum_{i>j} \vec{S}_i \cdot \vec{S}_J, \tag{1.3}$$

where J^{ex} is the exchange parameter. If J^{ex} is positive spins tend to align with their nearest neighbours (ferromagnetism) while if J^{ex} is negative spins tend to anti-align with their nearest neighbours (anti-ferromagnetism). Calculating J^{ex} even in this model is a non-trivial task that involves overlap integrals of electron wave-functions (direct-exchange) or, in the case of superexchange, the Goodenough-Kanamori rules can give the sign of J^{ex} [54, 71]. J^{ex} can often be estimated by fitting the dispersion relation measured with neutron or x-ray scattering data to a theoretical model, while magnetic susceptibility measurements can give an estimate.

Magnetic susceptibility is a measure of the bulk (the culmination of all the individual spins) magnetism of the material with the magnetic susceptibility tensor, χ_{ij}, given by,

$$M_i = \chi_{ij} H_j \tag{1.4}$$

for magnetization M_i in an applied field H_j. The anisotropy of the susceptibility may be negligibly small in some materials, in which case the indices may be dropped. In a localized electron picture, for temperatures $k_B T > |J^{ex} S\,(S+1)|$ the system is in a paramagnetic state, and for temperatures well above θ_{CW} while neglecting crystal electric field effects the susceptibility is described by the Curie-Weiss law,

$$\chi = \frac{C}{T - \theta_{CW}}, \tag{1.5}$$

where C is the Curie Constant and θ_{CW} the Curie-Weiss temperature [6]. The Curie-Weiss constant gives a mean-field theory energy scale of the magnetic interaction in 3 dimensions,

$$\theta_{CW} = \frac{2S\,(S+1)}{3K_B} \sum_n z_n J_n^{ex} \tag{1.6}$$

where z_n is the number of nth nearest neighbours. The Curie constant can also be used to estimate the magnetic moment of the ions. For conventional magnets, the ordering temperature T_c or T_N is close to $|\theta_{CW}|$. The sign of θ_{CW} is the same as the sign of the exchange coupling and therefore a negative θ_{CW} indicates antiferromagnetic exchange interactions while a positive θ_{CW} indicates ferromagnetic interactions. Just above θ_{CW} short-range magnetic correlations develop and as the temperature is lowered through θ_{CW} in a conventional magnet, rotational symmetry is broken, that is, the magnetic moments choose a preferred direction and "order". For conventional magnets,

the magnetization (or sublattice magnetization) is normally the order parameter in a Landau theory of phase transitions describing the system.

Far more interesting is the case where there are strong magnetic interactions but no magnetic ordering at the Curie-Weiss temperature. These types of systems will be the focus of most of this thesis.

1.2.1 Frustrated Magnetic Systems

A frustrated magnetic system is one where all pairwise magnetic interactions cannot be simultaneously satisfied. This can be caused by geometric frustration, where the geometry of the crystal lattice on which magnetic ions sit prevents a pairwise minimization of the energy, or by competing interactions of approximately the same strength. Figure 1.1 shows 3 frustrated systems; the Kagomé and Pyrochlore lattice are examples of a 2-dimensional and 3-dimensional geometrically frustrated lattice, while the square lattice with interactions J_1^{ex} and J_2^{ex} may be frustrated based on the signs and strengths of the interactions. Geometrically frustrated systems are commonly formed from tri-

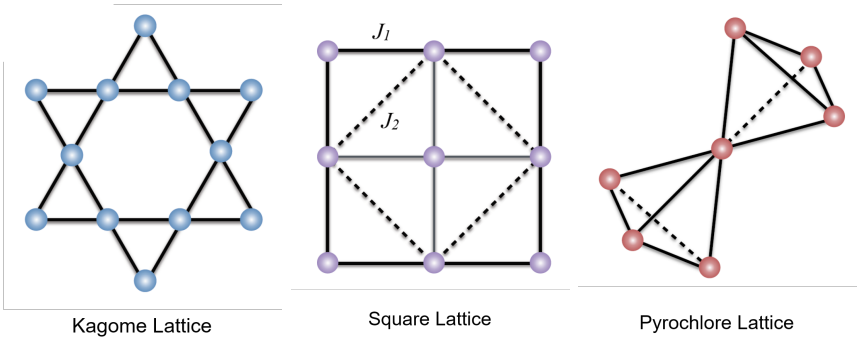

FIGURE 1.1: Frustrated Magnetic Lattices. Left: Kagomé lattice, Center: Square lattice with competing interactions and Right: Pyrochlore lattice. Reused from [59, 60] with permissions.

angles in 2-dimensions or tetrahedra in 3-dimensions that can either be corner-sharing (Kagomé/Pyrochlore lattice) or edge-sharing (triangular/FCC lattice). The level of frustration in a magnetic system is expressed by the frustration parameter,

$$f = \left| \frac{\theta_{CW}}{T_C} \right|, \tag{1.7}$$

with $f \geq 10$ loosely defining a frustrated system [102].

1.3 Pyrochlores

Pyrochlores are a class of materials with the chemical formula $A_2B_2O_7$ where the A ions and B ions each form a set of corner-sharing tetrahedra as shown in Fig. 1.2 [52]. Crystallographically, the pyrochlore structure has space group $Fd\bar{3}m$ with the A and B

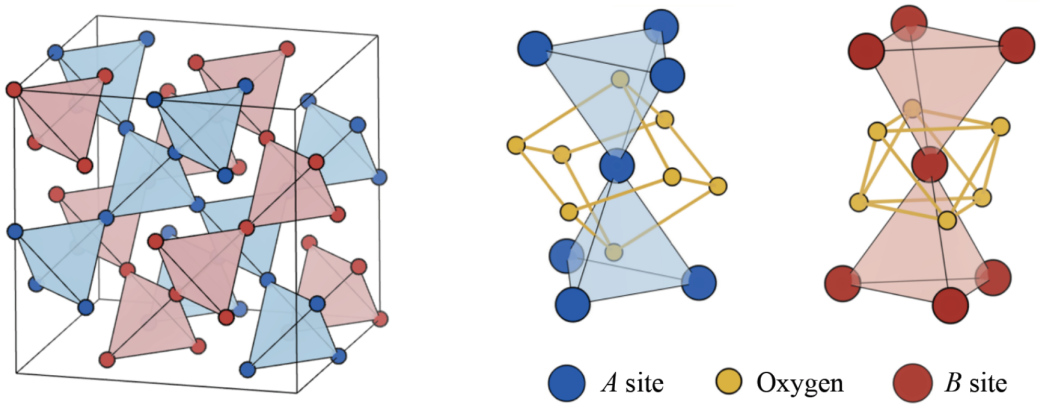

Figure 1.2: Left: Network of corner-sharing tetrahedra formed by the A and B sites in a pyrochlore lattice, Center: A site with the local oxygen configuration and Right: B site with local oxygen configuration. Figure reproduced from [60] with permissions.

sites on Wyckoff positions 16c and 16d respectively. The chemical formula is sometimes written as $A_2B_2O_6O'$ due to the two crystallographically inequivalent oxygen sites. The O' oxygen sits at the 8b Wyckoff position in the center of the A sublattice tetrahedra. The point group of the A site is D_{3d} which has as elements a three-fold rotation axis, an inversion center, two two-fold rotation axis, and a mirror plane. The three-fold rotation defines a local z-axis which we will refer to as the local [111] axis, while the two-fold rotation axes define the x and y-axes. This will have important consequences for crystal electric field splitting.

There are over 150 materials that form in the pyrochlore structure which for oxides may be further divided into $A_2^{3+}B_2^{4+}O_7$ and $A_2^{2+}B_2^{5+}O_7$ families [52]. In this thesis, we focus on the $A_2^{3+}B_2^{4+}O_7$ family with a magnetic rare-earth ion on the A site and a non-magnetic ion on the B site. A portion of this degree was spent examining the effect of B-site disorder by substituting an equal mixture of Sc^{3+} and Nb^{5+} onto the B-site. This causes distortions of the local oxygen environment and in general, but not always, will reduce the point group symmetry of the A site. The effects of the local oxygen environment are encompassed in what is referred to as single-ion physics to which we turn to now.

Rare-earth pyrochlores exhibit a wide range of magnetic ground states due to their markedly different single ion physics as well as exchange and dipolar interactions. For most pyrochlores there are well separated energy scales for the spin-orbit coupling ($\approx$ 1 eV), crystal electric field (CEF $\approx$ 100 meV), and exchange interaction (0.1-1 meV), allowing for a perturbative approach to describing their physics.

Rare-earth ions are heavy, resulting in a large spin-orbit coupling, $\lambda \propto Z^4$. The spin-orbit coupling energy has a magnitude given by,

$$\left\langle \lambda \vec{L} \cdot \vec{S} \right\rangle = \frac{\lambda}{2} \left(J\left(J+1\right) - L\left(L+1\right) - S\left(S+1\right) \right) \tag{1.8}$$

which splits the (2L+1)(2S+1) levels into well defined J manifolds, each with degeneracy 2J+1. It can be shown that the energy difference between states with angular momentum J and J-1 is given by λJ, meaning the ground state is well separated from excited states. Hund's rules are used to determine the ground state J for a given ion. The first rule is to maximize the spin angular momentum S. In this way, all electron orbitals are singly occupied before placing two electrons in the same orbital. The second rule is to maximize the orbital angular momentum meaning for the f-electrons in the rare earths, the orbitals are filled from 3+ to 3- in decreasing order. Hund's first and second rules serve to minimize the Coulomb repulsion between electrons. The last rule is to minimize the spin-orbit coupling by choosing J = L+S for ions with shells that are less than half filled and J = |L-S| for ions with shells that are more than half filled. Hund's rules work very well for rare earth ions but fail to capture the behaviour of transition metals. In transition metals the spin-orbit coupling is much weaker due to a smaller Z, usually resulting in orbital quenching with L=0 and J=S.

The next energy scale to consider comes from the electric field due to ions surrounding the rare earth. For pyrochlore oxides, this crystal electric field (CEF) is most strongly due to the surrounding oxygen ions and splits the 2J+1 degeneracy. The CEF causes a large splitting relative to the exchange interactions except for Gd^{3+} which due to a half full shell the CEF has no effect to first order. The crystal electric field approximation is to replace the oxygen ions with a point charge of -2e then use the D_{3d} point symmetry to write a crystal field Hamiltonian of the form,

$$H_{CEF} = B_2^0 \hat{O}_2^0 + B_4^0 \hat{O}_4^0 + B_4^3 \hat{O}_4^3 + B_6^0 \hat{O}_6^0 + B_6^3 \hat{O}_6^3 + B_6^6 \hat{O}_6^6, \tag{1.9}$$

where $\hat{O}_j^i$ are Steven's operator equivalents [121], polynomials of order i in the total angular momentum J. The B_j^i are CEF parameters that approximate the Coulomb potential from neighbouring ions [105]. The CEF parameters can be determined from inelastic neutron scattering. Once the CEF parameters are determined the ground state wave function, $\left|\phi_0^{\pm}\right\rangle$ can be written in terms of the J_z basis, $|m_J\rangle$ where m_J ranges from -J to J. The anisotropic g-tensor is then given by,

$$g_z = 2g_J \left\langle \phi_0^{\pm} \right| J_z \left| \phi_0^{\pm} \right\rangle \tag{1.10}$$

and

$$g_\perp = g_J \left\langle \phi_0^{+} \right| J_+ \left| \phi_0^{-} \right\rangle = g_J \left\langle \phi_0^{-} \right| J_- \left| \phi_0^{+} \right\rangle. \tag{1.11}$$

For g_z much greater than $g_\perp$ the spins are Ising-like while for $g_\perp$ much greater than g_z the spins are XY like with respect to the local [111] axis. For a well-isolated ground state, that is, a CEF configuration where the first excited state has a large separation from the

ground state, the low-temperature properties are completely determined by the ground state. For rare-earth pyrochlore systems, the CEF ground state is most often a doublet forming a pseudo-spin 1/2 system. It is then important to consider if the rare-earth ion has an odd or even number of electrons. For an odd number of electrons, Kramers theorem says that each energy level must be at least doubly degenerate; in particular for our current treatment, the ground state. For this reason, ions with an odd number of electrons are referred to as Kramers ions while ions with an even number of electrons are referred to as non-Kramers ions. Non-Kramers ions may also have a ground state doublet but it is not guaranteed.

Following Rau *et al.* [105] there are three cases of interest for a ground state doublet; an effective spin-1/2 doublet, a dipole-octupole doublet, and the non-Kramers doublet. In each case, pseudo-spins are found by projecting from the total J-manifold to the CEF ground state. Applying the allowed local symmetry operations of the D_{3d} point group to the pseudo-spins elucidates their behaviour; the effective spin-1/2 pseudo-spin behaves exactly like a spin-1/2 particle in regards to symmetry, for the dipole-octupole doublet the x and z components of the pseudo-spin transform like dipoles but the y component transforms like an octupole while for the non-Kramers doublet the transverse pseudo-spin components transform like electric quadrupoles and the z component transforms like a dipole [105]. All three types of doublets produce interesting physics and have found realizations in nature. In this thesis we are most interested in Dipolar-Ocutopolar doublets of which $Sm_2Ti_2O_7$, $Dy_2Ti_2O_7$, and several Nd based pyrochlores are examples.

1.3.1 Classical Spin Ices

An intriguing phase that may arise on the pyrochlore lattice is that of the classical spin ice. A physical realization of this phase is found in $Dy_2Ti_2O_7$. In this section, we review the theoretical development of the spin ice phase.

The first model proposed to have a spin ice ground state was due to Anderson [4] which placed antiferromagnetically coupled Ising spins on a spinel lattice (equivalent to the A site of the pyrochlore lattice) restricted to point along the global [001] direction. Considering only nearest neighbour interactions, the Hamiltonian of such a system is given by[69],

$$\mathrm{H} = J^{ex} \sum_{\langle i,j \rangle} \sigma_i \sigma_j, \tag{1.12}$$

where the energy is minimized by having two up spins and two down spins on each tetrahedron. This problem may be mapped to the common ice phase of water where there are two hydrogen atoms close to an oxygen atom and two hydrogen atoms far away from an oxygen atom; one of the two ice rules proposed by Bernal and Fowler [68]. Out of the 16 possible ways of placing spins on a tetrahedron, 6 satisfy the ice rules. Each spin belongs to two tetrahedra so tetrahedra are not independent; choosing a direction for every spin on a tetrahedron automatically constrains the 4 adjacent tetrahedra, reducing the number of states by a factor of 4. Not considering the ice rules this would lead to 4^N states per tetrahedron. Further, we can divide tetrahedra into tetrahedra

that have a vertex pointing in the global [111] direction (up tetrahedra) surrounded by tetrahedra with a vertex pointing in the [11-1] direction (down tetrahedra). For a system of N tetrahedra, this leads to $(4)^{N/2}(6/16)^{N/2} = (3/2)^{N/2}$ microstates within the ground state [68]. Therefore, the ground state is massively degenerate as the number of tetrahedra increases. Heat capacity measurements on $Dy_2Ti_2O_7$ produce an entropy that is reduced from $R\ln(2)$ by $\frac{R}{2}\ln\left(\frac{3}{2}\right)$ and leads to the analogy with ice. $Dy_2Ti_2O_7$ is however not described by this model but one with the same result for the entropy.

If we consider CEF effects, it can be shown that for quite a few pyrochlores the moments are constrained to lie along the local <111> directions,

$$\vec{S}_1 = \frac{\sigma_1}{\sqrt{3}}\begin{pmatrix}-1\\-1\\+1\end{pmatrix}, \vec{S}_2 = \frac{\sigma_2}{\sqrt{3}}\begin{pmatrix}+1\\+1\\+1\end{pmatrix}, \vec{S}_3 = \frac{\sigma_3}{\sqrt{3}}\begin{pmatrix}+1\\-1\\-1\end{pmatrix}, \vec{S}_4 = \frac{\sigma_4}{\sqrt{3}}\begin{pmatrix}-1\\+1\\-1\end{pmatrix} \tag{1.13}$$

where $\sigma_i = \pm 1$. We refer to each vector as the local z-axis for a given spin. It is readily seen that $\vec{S}_i \cdot \vec{S}_j = -\frac{1}{3}\,(i \neq j)$ and therefore the Hamiltonian for the system may be rewritten as,

$$\mathrm{H} = -J^{ex}\sum_{\langle i,j\rangle}\vec{S}_i \cdot \vec{S}_j = \frac{J^{ex}}{3}\sum_{\langle i,j\rangle}\sigma_i\sigma_j. \tag{1.14}$$

That is, ferromagnetically coupled spins in this model are equivalent to the antiferromagnetically coupled spins of the Anderson model with a reduced exchange parameter and therefore may also host a spin ice phase. With the spins constrained in this way, antiferromagnetic interactions lead to long-range all-in all-out order where on a tetrahedron all spins point in (out) and spins on neighbouring tetrahedra point out (in).

$Dy_2Ti_2O_7$ (J_z=15/2) and $Ho_2Ti_2O_7$ (J_z=8) both display spin ice phases at low temperatures, however, they both have antiferromagnetic nearest neighbour exchange interactions and would naively enter a long range ordered phase at low temperatures. The crux with these materials is the very large magnetic moments of $\approx 10\ \mu_B$ which lead to (ferromagnetic) dipole-dipole interactions with strength, $D \approx J^{ex}$. As the moments are strictly Ising and the full moment lies along the local z-axis we may replace $\vec{S}_i = \langle J_z\rangle\,\sigma_i\hat{z}_i$ and arrive at the classical nearest neighbour Dipolar Spin Ice Model (DSIM),

$$\mathrm{H} = \frac{-J^{ex}}{2}\sum_{(i,j)}\sigma_i^{z_i}\sigma_j^{z_j}\hat{z}_i\cdot\hat{z}_j + \frac{D}{2}\sum_{(i,j)}\frac{(\hat{z}_i\cdot\hat{z}_j - 3\hat{z}_i\cdot\hat{r}_{ij}\hat{r}_{ij}\cdot\hat{z}_j)}{(r_{ij}/r_{nn})}\sigma_i^{z_i}\sigma_j^{z_j}, \tag{1.15}$$

where we have redefined $J^{ex} = J^{ex}\langle J_z\rangle^2$, $D = \mu_0\left(g_L\mu_B\langle J_z\rangle\right)^2/\left(4\pi r_{nn}^3\right)$, $\hat{r}_{ij}$ is a vector pointing between spins i and j, r_{ij} is the distance between spins i and j, and r_{nn} is the nearest neighbour distance. Note that σ just takes values ± 1 depending on whether the moment points in or out of the tetrahedron and the factor of 2 cancels out double counting of spins [68]. Calculating the dot products and adding in a term for dipolar

interactions beyond nearest neighbour we arrive at,

$$H = \left(\frac{J^{ex}}{3} + \frac{5D}{3}\right) \sum_{(i,j)} \sigma_i^{z_i} \sigma_j^{z_j} + H^{dip}_{>r_{nn}}. \tag{1.16}$$

In this way, dipolar interactions stabilize the spin ice phase [65] and only modify the magnetic correlations at short distances compared to the nearest neighbour spin ice model.

If we consider a coarse-grained magnetic field, $M(r)$, on each tetrahedron and regard the 4 spins on a tetrahedron as local sources of magnetic flux, the spin ice rules correspond to a divergence-free condition, $\nabla \cdot M(r) = 0$. This leads to magnetic correlations that are similar to the ones generated by a dipole-dipole interaction [69]. Phases that satisfy a divergence-free condition are called Coulomb phases [68] in analogy with electromagnetism. These correlations lead to pinch points in diffuse neutron scattering measurements.

Much interest in these materials was generated when Castelnovo *et al.* [27] showed that by considering a dumbbell model for the spins on a tetrahedron, the spin ice state may be mapped to a vacuum state for magnetic monopoles and the excitations of the spin ice state, 3-in spins and 1-out spin (or 1-out 3-in), correspond to magnetic monopoles. In the model, the dipole spins on each vertex of a tetrahedron are stretched out into a pair of oppositely charged monopoles that sit in the center of a tetrahedron. Appropriately scaling the interactions, it can be shown that an excited state of the spin ice phase on a pyrochlore lattice corresponds to two oppositely charged magnetic monopoles on adjacent tetrahedra. The monopoles exist on the diamond lattice generated from the center of the tetrahedra and it may be shown that the dipole-dipole interaction between spins corresponds to a Coulomb interaction between magnetic monopoles, meaning there is a finite energy cost to move monopoles infinitely far away. In this model, a single spin-flip therefore generates two oppositely charged monopoles on adjacent tetrahedra and, once created, move freely and independently using a series of spin-flips. This leaves a tension-less string of spin-flips between monopoles known as a Dirac string. Differences between this model and the DSIM, are of the order $1/\mathrm{r}^5$.

The study of these materials at the lowest temperatures is prohibited by the extremely long time to reach thermal equilibrium [101]. The spins fall out of equilibrium on the time scale of an experiment making it practically impossible to study the dynamics of the systems below ≈ 0.5 K. In this thesis, we consider the possibility that $Dy_2Ti_2O_7$ acts as a supercooled magnetic liquid, in analogy with the supercooled state of dielectric glass forming liquids.

1.3.2 Dipolar-Octupolar Doublets

The Dipolar-Octupolar doublet is of special importance to this thesis as this is the CEF ground state for both $Dy_2Ti_2O_7$ and $Sm_2Ti_2O_7$ as well as several Neodymium based pyrochlores [105]. As mentioned previously, this doublet includes ground states formed

solely by $|J_z| = 3/2$, $9/2$, and $15/2$ states, or some combination thereof. Not only does this doublet include an all-in all-out ordered phase and the classical spin-ice phase but it also includes two distinct quantum spin-ice phases [67]. In these phases, transverse couplings (couplings which include the J_x and J_y components of the magnetic moments, both between themselves and J_z) act to perturb the classical spin-ice phase, allowing for quantum oscillations between different spin-ice states. This leads to a highly fluctuating ground state; a quantum spin liquid known as a quantum spin ice. Later it was shown that the quantum spin ice phase can be further divided into states which have 0 or π units of flux penetrating plaquettes [12, 11]. Ref. [104] shows that the transverse interactions for $Dy_2Ti_2O_7$ are negligible due to the ground state being dominated by the $J_z = 15/2$ state.

What is special about the Dipolar-Octupolar doublet (as the name suggests) is that transforming the pseudo-spin 1/2 states through the allowed D_{3d} symmetry operations shows that the x and z components of the pseudo-spins transform like magnetic dipole moments while the y component transforms like a magnetic octupole moment. In terms of the pseudo-spin 1/2 states $|+\rangle$ and $|-\rangle$ the spin-operators have the usual construction [105];

$$S^z = |+\rangle\langle+| - |-\rangle\langle-|, \tag{1.17}$$

and

$$S^{\pm} = |\pm\rangle\langle\mp|. \tag{1.18}$$

The states $\left|\pm\frac{15}{2}\right\rangle$, $\left|\pm\frac{9}{2}\right\rangle$, and $\left|\pm\frac{3}{2}\right\rangle$ do not mix under the C_3 operation, allowing the most general Hamiltonian to be simplified to,

$$H^{DO} = \sum_{\langle i,j\rangle} J_{zz} S_i^z S_j^z + J_{xx} S_i^x S_j^x + J_{yy} S_i^y S_j^y + J_{xz}\left(S_i^x S_j^z + S_i^z S_j^x\right), \tag{1.19}$$

for Dipolar-Octupolar doublets. A global pseudo-spin rotation removes the J_{xz} term [67, 10, 105], leading to the XYZ Hamiltonian,

$$H_{xyz}^{DO} = \sum_{\langle i,j\rangle} \tilde{J}_x \tilde{S}_i^{\tilde{x}} S_j^{\tilde{x}} + \tilde{J}_{\tilde{y}} \tilde{S}_i^{\tilde{y}} \tilde{S}_j^{\tilde{y}} + \tilde{J}_{\tilde{z}} \tilde{S}_i^{\tilde{z}} S_j^{\tilde{z}}. \tag{1.20}$$

For details of this procedure see [67] and [10]. Huang *et al.* [67] showed that this model hosts the aforementioned ordered phases, classical spin-ice phase as well as a Dipolar and Octupolar quantum spin-ice phase. It was later shown [10] that the Dipolar-Octupolar doublet can simultaneously host an ordered all-in all-out phase and spin-ice phase in a process known as moment fragmentation, to which we turn to now.

1.3.3 Moment Fragmentation

In this section, we review moment fragmentation which is relevant for our study of Nd_2ScNbO_7. Moment fragmentation is the idea that the magnetic field from a moment can fractionalize into a divergence-full and a divergence-free part [18]. A Helmholtz decomposition of the magnetic field, M, into a divergence-free and a divergence-full part

leads to,

$$M(r) = M_m + M_d = \nabla\Psi + \nabla \times A, \tag{1.21}$$

where Ψ and A are a scalar and vector field, respectively, M_m is a divergence-full field, while M_d is a divergence-free field. We strictly focus on this possibility for the pyrochlore lattice. In states obeying the ice rules $M_m = 0$ while breaking the ice rules will introduce a divergence-full field. Brooks-Bartlett *et al.* were able to show that the existence of monopoles does not fully suppress the divergence-free field [18]. For instance, if we consider a 3-in 1-out state as,

$$\vec{M} = (-1,-1,-1,1) = (-1/2,-1/2,-1/2,-1/2) + (-1/2,-1/2,-1/2,3/2)\,, \tag{1.22}$$

then the first part is a divergence-full field and the second part is a divergence-free field. The first part has all moments pointing inwards while the second part corresponds to a Coulomb phase (however, it is not a spin ice phase). Working within the dumbbell model they show that a monopole crystal, where there are alternating positive and negative monopoles on every tetrahedron, could be decomposed into an all-in all-out ordered phase in combination with a Coulomb phase. Neutron scattering measurements would then display Bragg peaks from the all-in all-out order along with diffuse scattering and pinch points from the Coulomb phase.

This combination was measured by Petit *et al.* in the dipole-octupole pyrochlore $Nd_2Zr_2O_7$ [99]. Later studies point to a quantum spin ice phase above T_N which acts to suppress the order [140]. Returning to our description of Dipolar-Octupolar doublets (see section 1.3.2) in terms of rotated pseudo-spin states, the magnetic moment in the (physical) z-direction is given by,

$$m_i = g_z\mu_B \cos(\nu)\, \tilde{S}_i^{\tilde{z}} z_i + g_z\mu_B \sin(\nu)\, \tilde{S}_i^{\tilde{x}} z_i, \tag{1.23}$$

where ν is the rotation angle which removes the J_{xz} term in Eq. 1.3.2. For $Nd_2Zr_2O_7$ it turns out that $\tilde{S}_i^{\tilde{z}}$ orders antiferromagnetically while fluctuations of $\tilde{S}_i^{\tilde{x}}$ are shifted to finite energy. Benton [10] was able to show that fluctuations of both $\tilde{S}^{\tilde{x}}$ and $\tilde{S}^{\tilde{y}}$ are dynamically decoupled into a divergence-free and divergence-full part. This is done by considering the Heisenberg equations of motion and linearising around the all-in all-out ground state. The divergence-free part of the fluctuations forms a flat band at finite energy while the divergence-full part forms two dispersive bands. The magnetisation field of $Nd_2Zr_2O_7$, therefore, has 3 components; an all-in all-out statically ordered component, a divergence-free component with Coulomb like correlations, and an additional divergence-full component corresponding to finite energy dispersive bands. This particular model has relevance to Nd_2ScNbO_7 which displays Coulomb-like pinch points in combination with magnetic Bragg peaks in neutron scattering measurements [86].

1.4 Spin Glasses

Mydosh gives a working definition of a spin glass as "a random, mixed interacting, magnetic system characterized by a random, yet cooperative, freezing of spins at a well-defined temperature T_g, below which a highly irreversible, metastable frozen state occurs without the usual long range spatial magnetic order" [92]. The canonical spin glasses are mixed alloys with a small percentage of magnetic impurities, such as CuMn and AuFe. Here the RKKY (Ruderman-Kittel-Kasuya-Yosida) interaction, which oscillates as a function of distance and falls off as $1/r^3$, provides randomness in the interactions of the magnetic impurities as the impurities are randomly distributed throughout the alloy. These systems are collectively called dilute spin glasses. In this thesis we are interested in dense, insulating, spin glasses where magnetic ions form a repeating lattice and the RKKY interaction, due to the polarization of *conduction* electrons around a magnetic impurity, plays no role. The site randomness has been (mostly) removed in these materials and normally there is some randomness in the bond strength [49]. Randomness in the bond strength can be caused by slight variations in the bond length and/or bond angle between ions which can effect direct exchange, super-exchange and, dipolar interactions, leading to disorder and glassy behaviour in dense, insulating spin glass systems. These spin glass systems also typically, but not always, include competing interactions and frustration.

A spin glass has a complicated energy landscape with many local energy minima. As such they are normally formed of many metastable states and while having no long-range order, exhibit magnetic correlations in both time and space. As the temperature is lowered through the glass transition the system falls into a local energy minimum, selecting one of the metastable states in a region of, or throughout, a material. Transitions between metastable states cause dynamic magnetism even below the "freezing" or glass transition. This important quality is most readily seen in AC susceptibility measurements where the freezing temperature changes as a function of the driving frequency of the magnetic field. In DC susceptibility a splitting of the field cooled (FC) and zero field cooled (ZFC) susceptibility is observed due to the field providing a preferred direction for the spins to point along as they freeze during cooling. After waiting an infinite amount of time, the ZFC and FC susceptibilities should be the same as the metastable states fluctuate to point along the preferred direction of the applied field. Measuring the DC magnetization as a function of time is another way to probe spin glass systems but may depend on the field cooling protocol and cooling rate. In heat capacity measurements of spin glasses, a broad hump is observed at $\approx$1.5-2 T_g while well below T_g there is usually a linear relationship between temperature and heat capacity with an occasional quadratic component [92]. In neutron scattering no magnetic Bragg peaks are observed, consistent with a lack of long range order, however as the temperature is reduced from high temperature to the freezing transition, intensity is transferred from the quasi-elastic channel to the elastic channel as the spins appear to become static on time scales that a neutron experiment can probe.

In this thesis, we probe the candidate spin glass system Gd_2ScNbO_7 using AC susceptibility and Muon Spin Rotation, Relaxation, and Resonance (μSR).

1.5 Supercooled Liquids

There is evidence that, at low temperatures, the characteristic relaxation time of magnetic excitations in $Dy_2Ti_2O_7$ is super-Arrhenius, i.e. it increases faster than Arrhenius behaviour. It is found that the relaxation time increases even faster than predicted from Debye-Huckle theory for a free monopole gas or the Dipolar spin-ice model [147, 73, 45]. It is well known that supercooling a liquid produces a state with super-Arrhenius behaviour and there has been success in describing the dynamic magnetism of $Dy_2Ti_2O_7$ as analogous to a supercooled liquid [73, 45]. Here we review the basic theory of supercooled liquids to apply this theory to $Dy_2Ti_2O_7$.

When a homogeneous liquid of a single material is cooled to its melting temperature, T_m, it normally undergoes a first-order transition to a solid state with global ordering. This does not have to occur however as the formation of solid crystals depends on free energy differences and time. If the material is cooled down faster than the time it takes to form a nucleation site, the material can remain in the liquid state below T_m, in a process known as supercooling. Below T_m nucleation involves two energy contributions; an energy cost due to configurational mismatches at a domain wall (an effective surface tension) and an energy gain due to the lower free energy of the crystalline state compared to the liquid state [28]. The change in energy when a crystalline domain of radius, R, is created is $\Delta G(R) = \sigma R^2 - \delta g R^3$, where σ is the surface tension and δg is the free energy difference between the liquid and solid phase. There is a critical radius R_c which maximizes $\Delta G(R)$ and this is the energy that must be overcome for a solid to order out of a liquid region. As there is a simple energy barrier to be overcome, nucleation is a thermally activated process with an Arrhenius form for the nucleation time, $\tau \propto \exp\left(\frac{\Delta G(R)}{K_B T}\right)$ which diverges both at T_m and as T $\to$ 0. Near T_m, there is a wide range of cooling rates that avoid a transition into the ordered state as well as a dynamical transition into a glass state. Cooling in this way the system remains in a metastable, disordered state with many of the properties of the initial liquid.

Fig. 1.3 shows the nucleation time as a function of temperature in red. Cooling along the dashed line allows the system to avoid a transition into the ordered state. However, as the temperature is lowered substantially below T_m, correlations in the liquid state substantially alter the microscopic relaxation processes (e.g. shear relaxation). The relaxation times associated with these processes generally increase faster than Arrhenius [14, 5, 80], that is, the relaxation time diverges at some temperature, $0 \leq T_0 \leq T_m$. This leads to relaxation times that are longer than the timescales of an experiment. Once the relaxation time is longer than the experimental time-scale, the system can no longer explore its full phase-space and undergoes a dynamical transition out of equilibrium into a glass state. In this state, the system constantly undergoes ultra-slow relaxation, with no long range order, that is effectively unchanged on experimental time scales. Time

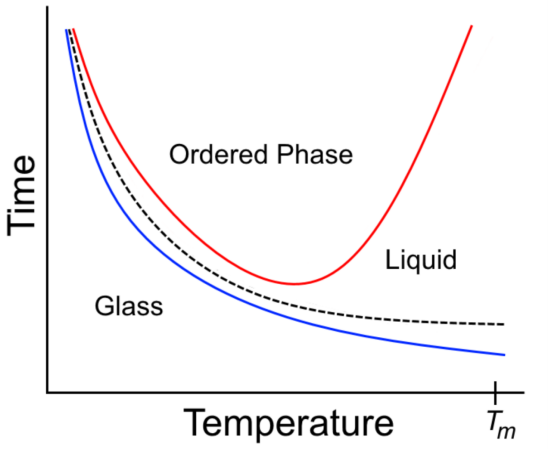

FIGURE 1.3: Sketch of the nucleation time (red) to form crystalline regions in a liquid. Microscopic relaxation times within the liquid phase are shown in blue. The dashed line shows a cooling protocol that allows the material to remain a liquid well below T_m. Relaxation times begin to diverge quickly at low temperatures making it practically impossible to avoid a dynamical transition to an out of equilibrium glass phase or to a first-order transition into a solid phase. Reused from [72] under fair-use/dealing.

translation invariance is lost and properties of the system depend upon the initial time, t_0, as well as the difference in time between two measurements $t - t_0$ [28].

In this thesis, we are interested in the relaxation time and the response of a frequency-dependent perturbation. The relaxation times of supercooled liquids follow a Vogel-Tamman-Fulcher trajector [28, 14, 5],

$$\tau = \tau_0 \exp\left(\frac{DT_0}{T - T_0}\right), \tag{1.24}$$

where D is the "fragility" of the material and T_0 is the temperature at which the relaxation time diverges. The fragility characterizes how similar or different the relaxation is from Arrhenius law, with large fragility ($D \approx 100$) being similar to Arrhenius relaxation and small fragility ($D \approx 10$) showing large deviations from Arrhenius behaviour.

The relaxation time can be measured in the frequency domain by considering the complex dielectric function, $\epsilon(\omega, T)$, which for a supercooled liquid follows a Havriliak-Negami form [62],

$$\epsilon(\omega, T) = \epsilon_\infty + \frac{\epsilon_0}{(1 + (i\omega\tau_{HN})^\alpha)^\gamma}, \tag{1.25}$$

where ϵ_0 is the relaxation amplitude, τ_{HN} is the relaxation time, α is a stretching parameter, and γ is an asymmetry parameter. ϵ_∞ is a real number that gives the relaxation in the $\omega \to \infty$ limit which is non-zero due to non-instantaneous heat transfer between dipoles and the lattice they reside on [25].

For the magnetic system $Dy_2Ti_2O_7$, we test if the complex magnetic susceptibility follows a Havriliak-Negami form in an applied AC field. We note that for $\alpha = \gamma = 1$ we recover the Debye form for a relaxation process with a single relaxation time.

1.6 Superconductivity

Superconductivity is a state of matter characterized by perfect electrical conductivity and perfect diamagnetism. Perfect electrical conductivity was first observed by Onnes in Mercury [94] while perfect diamagnetism was observed by Meissner and Ochsenfeld in 1933 [87] and has been termed the "Meissner Effect". A theoretical explanation for superconductivity did not occur until 1957 when Bardeen, Cooper, and Schrieffer introduced BCS theory. Cooper proved the instability of the Fermi surface to pair formation meaning that any net attractive interaction between electrons at the Fermi surface would cause them to form Cooper pairs. The Cooper pairs act as bosons and can flow through a material with no resistance [7]. It was pointed out that the attractive interaction could be mediated by phonons and was confirmed for several type-I superconductors by studying isotopes of the same element. The BCS theory provided the basis of "conventional" superconductivity and opened the door for their microscopic study.

In this section, we review important concepts and quantities from BCS and Ginzberg-Landau theory. We discuss how these quantities are measured experimentally. Finally, we explain how a transverse field μSR experiment can measure the critical field of a type-I superconductor.

Superconductors can be characterized by two length scales; the coherence length, ξ, and the penetration depth, λ. Roughly speaking, the (Pippard) coherence length is the size of the Cooper pair while the penetration depth is the distance a magnetic field can penetrate a superconductor. The Ginzberg-Landau coherence length is the characteristic length over which the Ginzberg-Landau order parameter can vary without an undue energy increase [131]. Both quantities are temperature-dependent and Abrikosov showed that $\kappa = \frac{\lambda}{\xi} = \frac{1}{\sqrt{2}}$ separates superconductors into two classes, type-I and type-II [1]. Neglecting demagnetization effects, the full volume of a type-I superconductor will be in the Meissner state below the critical temperature T_c and critical field H_c. Above the T_c and/or H_c superconductivity is lost. A type-II superconductor on the other hand has two critical fields, H_{c1}, below which the entire material is in the Meissner state, and H_{c2}, where for applied fields between H_{c1} and H_{c2} magnetic fields penetrate through the sample as vortex lines. Above H_{c2} superconductivity is lost. Fig. 1.4 shows the interface between a normal and superconducting region where the square of the Ginzburg-Landau order parameter is the density of superconducting Cooper pairs, n_s.

Forming Cooper pairs lowers the free energy of the system by an amount called the condensation energy, proportional to H_c^2. The energy required to break a Cooper pair into two quasi-particle excitations is called the superconducting energy gap, Δ. This energy gap leads to a low-temperature exponential behaviour in the specific heat, $C_p \propto \exp(-\Delta/k_B T)$, and a discontinuity at T_c as shown in Fig. 1.5, which is also

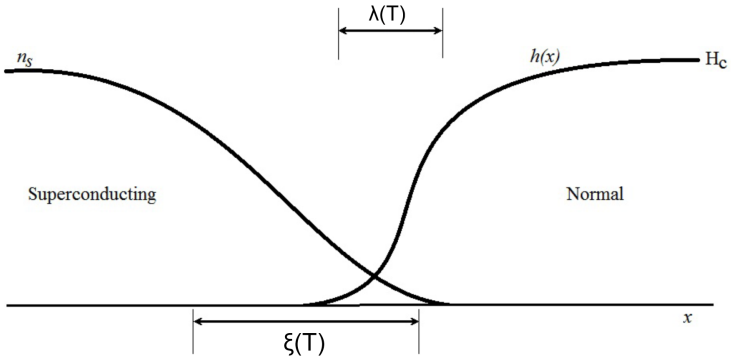

FIGURE 1.4: The interface between a superconducting and normal region illustrating how a magnetic field penetrates the superconductor and how the Ginzburg-Landau order parameter changes. Adapted from [135] and [131].

predicted by BCS theory. For BCS theory, $\Delta(T)$ is the order parameter and may be determined from a self-consistency equation [131].

The London penetration depth is given by,

$$\lambda_L^2 = \frac{m^* c^2}{4\pi n_s e^{*2}}, \tag{1.26}$$

where m^* and e^* are the mass and charge of the Cooper pairs and c is the speed of light. In the London theory, a magnetic field exponentially decays over a distance λ_L in a superconductor. The effective penetration depth, λ_{eff}, which is experimentally measured reduces to λ_L at zero temperature in the local, infinite wavelength, and infinite mean free path limit. The current response to a vector potential, which in general will have a q-dependence, is normally assumed to be able to be replaced by the infinite wavelength response. Under this assumption λ_L^2, and hence the supercurrent density is related to the energy gap through an integral equation [131]. In the following, we will consider how the experimentally measured λ_{eff} is related to λ_L.

In a metal, the current density response to an electromagnetic field is reduced due to electrons scattering off of defects. Electrons on average travel a distance, l, the mean free path, before encountering a defect. The response of the current density to distant fields is assumed to be exponentially reduced with a characteristic length of l. Pippard argued that a superconductor should have an analogous length scale for scattering off defects. Pippard was able to estimate this length scale and BCS theory gives the Pippard coherence length as,

$$\xi_0 = \frac{\hbar v_F}{\pi \Delta(0)}, \tag{1.27}$$

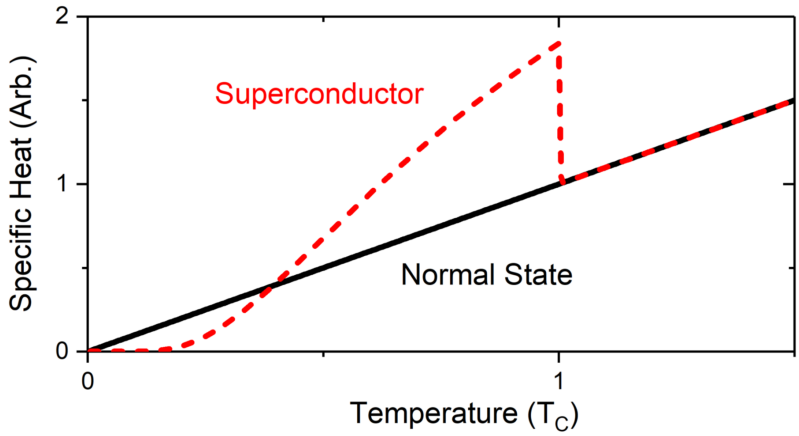

FIGURE 1.5: The specific heat of a superconductor showing exponential behaviour with a discontinuity at T_c compared to the linear behaviour expected for a metal. Reused from [137] under fair-use/dealings.

where v_F is the Fermi velocity. The Cooper pairs should also scatter off of the impurities of the metal and this results in a decreased coherence length,

$$\frac{1}{\xi} = \frac{1}{\xi_0} + \frac{1}{l}. \tag{1.28}$$

This defines two regimes; the clean limit with $\xi_0 \ll l$ and the dirty limit $\xi_0 \gg l$. The exponential decay with characteristic length ξ is a dimensionless "range function" for the Pippard theory which limits the effect of an electromagnetic field. BCS theory has a very similar dimensionless range function but with a very minor temperature dependence; it ranges from 1 at T=0 to 4/3 at $T = T_c$. The slight modification with temperature introduces some numerical value, C, in Eq. 1.28. The preceding work is all done so that λ_{eff} can be related to λ_L by,

$$\lambda_{eff} = \lambda_L \sqrt{1 + \frac{C\xi_0}{l}}, \tag{1.29}$$

and we can relate the measured penetration depth to the superconducting gap. Often the value C is assumed to be 1 for $0 \leq T \leq T_c$ when measuring λ_{eff} as a function of temperature.

The critical fields are related to the microscopic length scales by,

$$\sqrt{2} H_c \, \xi_{GL} \, \lambda_{eff} = \frac{\Phi_0}{2\pi}, \tag{1.30}$$

$$H_{c1} = \frac{\Phi_0}{4\pi\lambda_{eff}^2} \ln(\kappa), \lambda_{eff} \gg \xi, \tag{1.31}$$

and

$$H_{c2} = \frac{\Phi_0}{2\pi\xi_{GL}^2} = \sqrt{2}\kappa H_c, \tag{1.32}$$

where Φ_0 is the magnetic flux quanta and ξ_{GL} is the Ginzburg-Landau coherence length. As was mentioned, this is the distance over which the order parameter can change without undue energy increase and also the distance over which a disturbance to the order parameter is exponentially decaying. The second equation shows the importance of $\kappa = 1/\sqrt{2}$ in separating type-I and type-II superconductors. The temperature dependence of the critical fields, coherence length, and penetration depth has been suppressed in these equations. The empirically found critical field temperature dependence is,

$$H_c\left(T\right) = H_c\left(0\right)\left(1 - \left(\frac{T}{T_c}\right)^2\right) \tag{1.33}$$

which type-I, conventional superconductors follow, however, strong deviations from this may indicate an unconventional gap.

We have tacitly assumed, as in the original BCS theory, that the energy gap is isotropic i.e. it has no wavevector dependence. When the gap has no wavevector dependence, or a wavevector dependence that has the same symmetry as the crystal structure of the material, it is known as s-wave superconductivity. However, the gap can have lower symmetry than the crystal structure, examples of which are p-wave and d-wave superconductors. Both of these types of superconductivity have "nodes" where the gap goes to zero, the effect of which is to modify the temperature dependence of the penetration depth.

An excellent way to measure the penetration depth of type-II superconductors is through a transverse field μSR experiment. In type-II superconductors with an applied magnetic field between H_{c1} and H_{c2}, magnetic fields penetrate the sample in vortex lines, around which there is a core where the supercurrent density is zero. The size of the core is proportional to ξ_{GL} while the magnetic field decays away from these cores with characteristic length λ_{eff}, creating muon stopping sites with different field strengths. A single muon precesses in the local magnetic field at a site and decays into a positron. An ensemble of muons precessing in the field probability distribution produced by a vortex line or a vortex lattice produces a relaxing muon asymmetry. Both the size of the cores and the length over which the field decays affects the relaxation of the muon asymmetry and there is a relationship between the relaxation rate, coherence length, and penetration depth. H_{c2} measurements provide an estimate of the coherence length, and using the relationship between the relaxation rate, coherence length, and penetration depth allows the penetration depth of type-II superconductors to be determined from μSR measurements.

At first glance, it might appear that μSR would not be very useful in measuring type-I superconductors. Naively the entire sample would be in the Meissner state with zero internal field and zero variation in the internal field. A transverse field μSR measurement would therefore measure a constant asymmetry and little information would be gained.

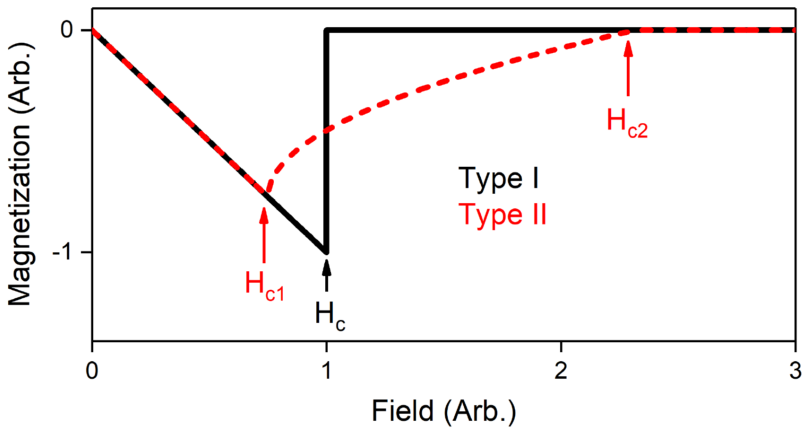

FIGURE 1.6: The magnetization as a function of applied field for a type-I (Black) and type-II (red) superconductor without considering demagnetization effects. Reused from [137] under fair-use/dealings.

The situation changes when demagnetization effects are considered. Demagnetization effects cause areas of the superconductor to experience a field that is stronger than the applied field. When these areas experience a field that is larger than the critical field they enter the normal state and allow magnetic fields to pass through the sample. Evaluating the penetrating magnetic field which minimizes the free energy it is found that in the normal regions the magnetic field is approximately equal to H_c, everywhere. This situation where parts of the material are normal and parts are superconducting is known as the intermediate state of a type-I superconductor.

Demagnetisation will skew the magnetisation as a function of applied field in a type-I superconductor by allowing fields to penetrate through the sample. Without considering demagnetization effects, the magnetization should discontinuously change at H_c for a type-I superconductor while a type-II superconductor will have a kink at H_{c1} and will decay continuously to zero at H_{c2} as shown in Fig. 1.6. Including demagnetising effects, a type-I superconductor will enter the intermediate state when the applied field is between $\approx (1-N)\,H_c$ and $\approx H_c$ and distorts the magnetization, giving a similar appearance as to what is expected in a type-II superconductor. Below $\approx (1-N)\,H_c$ the material is in the Meissner state while above H_c superconductivity is lost.

Correcting for demagnetisation effects can recover the M versus H behaviour with a discontinuity at $H_c(T)$. Alternatively, $H_c(T)$ can be measured in a transverse field μSR measurement. The field inside of the normal regions is nearly constant at $\approx H_c$ while in the superconducting regions the field is zero. This leads to a non-precessing signal from the Meissner state and, as the field takes a single value of approximately H_c within the normal regions, a precessing signal with frequency $\omega \approx \gamma_\mu H_c$. It turns out that the domain wall thickness, δ between normal and superconducting regions is of the order $\delta \approx \xi - \lambda$ [131], and, the relaxation will be related to this distance. It is however

hard to extract information about this distance because the superconducting/normal structure which minimizes the free energy changes as a function of field, cooling rate, and geometry (c.f. Ref [33] of Chapter 7) which also influences the exact details of how δ depends on ξ and λ. The interface energy between the superconducting and normal regions acts to slightly reduce the thermodynamic critical field in the normal regions from H_c to a value known as H_{cI}, however, for sample dimensions much larger than δ the difference becomes negligible. For more discussion of these effects see Chapter 7 of this thesis.

Chapter 2

Experimental Methods

2.1 Introduction

The work presented in this thesis required the use of several different experimental techniques and methods. To create powder oxide samples we employed solid-state reactions with stoichiometric amounts of the constituent oxide insulators. For BeAu our collaborators used an arc melt method to create polycrystalline samples. We used the Optical Floating Zone method to form single crystals from sintered rods of the requisite material. To confirm the phase purity of both powder and single-crystal samples we made use of Powder X-ray Diffraction. A Superconducting Quantum Interference Device was used to measure the Magnetisation and Magnetic Susceptibility of the samples. Finally, Muon Spin Rotation, Relaxation, and Resonance was used to probe the internal magnetic fields of most samples.

2.2 Optical Floating Zone

Crystal Growth is an inherently non-equilibrium process in which a phase transition from a disordered structure to an ordered structure occurs [120]. A variety of methods are employed to disturb a system from equilibrium; most notably for our purposes the application of temperature and temperature gradients. Crystals can be grown using Solid-Solid, Liquid-Solid, or Vapour-Solid transitions, of which the Optical Floating Zone (OFZ) technique uses a Liquid-Solid transition. Any Liquid-Solid crystal growth requires three things: supersaturation or supercooling, nucleation, and growth of nuclei into large single crystals [120].

The OFZ technique makes use of Halogen or Xenon lamps and ellipsoidal mirrors to focus light at the ends of two ceramic rods. The setup for a growth in the OFZ at McMaster is shown in Fig. 2.1. The rods are mounted vertically with the top end of the bottom (seed) rod and the bottom end of the top (feed) rod situated in one focal point of the mirrors. Inside both mirrors, a halogen lamp is located at the other focal point which, when the mirrors are closed together, allows intense light to be focused onto a circular area with a diameter of a few millimeters. Depending on the lamps used,

temperatures can range from 200-2000°C for halogen lamps and up to 3000°C for Xenon lamps in this narrow area.

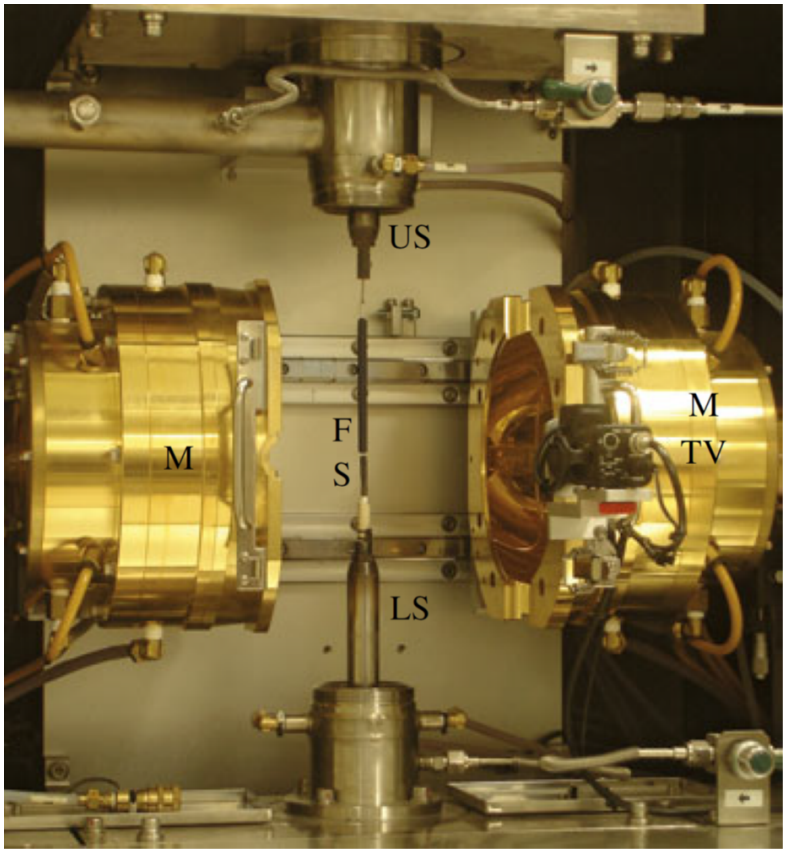

Figure 2.1: Optical Floating Zone at McMaster University. Halogen lamps are situated at one focal point of the two mirrors while the rods are situated at the other focal point when the mirrors are closed together. The acronyms are; M-Mirrors, US-Upper Shaft, LS-Lower Shaft, F-Feed rod, S-Seed Rod, TV- TV Camera

At the beginning of a growth, the tips of the rods are heated just until melting and gently moved together, resulting in a liquid zone floating between the two solid rods. As nothing is touching the zone other than the growth material itself, there is no possibility of impurities being introduced as is the case for methods that require a crucible. The upper and lower shafts are set to rotating in the same or opposite directions in the frequency range of 0-50 revolutions per minute. This allows for even heating of the zone as well as convection in the zone in the case of opposite rotation. The zone is then moved along the feed rod by either lowering the rods or raising the mirror at a rate of a few millimeters per hour to tens of centimeters per hour depending on the material. Just outside the focal point, the temperature can be several hundred degrees cooler, allowing for supercooling of the liquid melt just outside the zone. At defects, whether structural or an impurity in the material, microscopic crystals will nucleate and begin to grow as

the zone is moved. These crystals grow upwards and towards the center of the rods where they will meet and hopefully a dominant grain will develop, leading to a single crystal after a few millimeters of growth in the ideal case. As a grain can nucleate at any defect during growth, it is vitally important that the material is phase pure and a stable liquid zone is developed and maintained as quickly as possible. Accomplishing this can allow for the growth of single crystals that are a few millimeters to a centimeter in width and up to ten centimeters long.

An advantage of this method of crystal growth is the ability to grow crystals in a sealed environment of Oxygen, Argon, or mixes of gasses such as Argon and Hydrogen to promote the oxidation or reduction of ions. High pressures (up to 10 atm at McMaster while 300 atm can be achieved in state-of-the-art instruments) may be used to help stabilize a zone or promote a phase transition that is unfavourable at lower pressure. Depending on the buoyancy of impurities in the zone, impurities may float to the top of the zone and be filtered out of the material.

The OFZ technique does have limitations; it is unsuitable for materials with high vapour pressure, low viscosity, or those that undergo a phase transition during cooling. In general Liquid-Solid crystal growth methods of oxide materials can produce crystals that are slightly off stoichiometric. This can be due to the evaporation of constituent material or incongruently melting materials. A common practice to combat evaporation is to start from ceramic rods that are non-stoichiometric, in the hopes of making a stoichiometric crystal. Another option that can combat both evaporation and viscosity issues as well as to help maintain a congruent melt is to use a solvent (flux) in the zone. In this case, the solvent material is placed on top of the seed rod before growth and the crystal is grown very slowly, maintaining the flux within the molten zone as the growth progresses. After the growth is finished the crystal must be characterized to determine phase purity and crystallinity.

2.3 Powder X-Ray Diffraction

Powder X-ray Diffraction (PXRD) is a technique that can be used to verify the structure and phase purity of a material. A powdered sample is placed on a rotating disk at the joint of a goniometer. An X-Ray source is held stationary on one end of the goniometer, focused at the sample, while a detector sweeps an angle and records the scattered intensity of light at each angle. For PXRD a collimated, monochromatic X-ray source must be used. At McMaster, the X-ray source is a copper anode that produces Kα_1, Kα_2, and Kβ radiation. A nickel filter is used to absorb Kβ while a germanium crystal excludes Kα_2, leaving only the Kα_1 = 1.541 $\mathring{A}$ radiation. Scattering can only occur when the scattered wave-vector, $\Delta k = k_i - k_f$ is equal to a reciprocal lattice vector (here k_i and k_f are the initial and final wavevectors, respectively) [6]. This is a restatement of the Bragg condition,

$$n\lambda = d\sin\theta, \tag{2.1}$$

where n is an integer, λ is the wavelength of light, d is the interplanar spacing in the crystal structure and θ is the diffraction angle [6]. Hence the intensity of light detected as a function of angle reveals important information about the crystal structure and position of atoms within the material. This data is compared to known crystal structures and can be fit to a structural model using a Rietveld refinement program such as Fullprof [109].

2.4 SQUID Magnetometry

A Superconducting Quantum Interference Device (SQUID) is an extremely sensitive flux-to-voltage transducer capable of measuring magnetic flux up to a small fraction ($\approx 10^{-5}$) of a magnetic flux quantum, $\Phi_0 = \frac{h}{e}$ [31]. The name is related to the "interference pattern" in the current in a SQUID as a function of flux, analogous to the interference pattern in the intensity of light in a slit experiment. The device makes use of Faraday's law to induce a current in a superconducting loop of wire in response to changes in a magnetic field, namely, the magnetic field due to a magnetic sample as it is moved through a (few) detection coil(s). The flux through the superconducting loop is quantized and only able to change by multiples of a magnetic flux quantum. At least one weak link, known as a Josephson junction, is incorporated into a loop through which Cooper pairs can tunnel. A DC SQUID makes use of two Josephson junctions and time-independent currents while an RF SQUID makes use of one Josephson junction and oscillating currents. There are several types of materials that can be used to make a weak link; an insulating material, a normal metal, a constriction of the superconducting material, or the use of a bicrystal high-temperature superconductor where the junction is a single crystal whose axes are rotated with respect to the crystal the rest of the loop is formed from. Most high-temperature superconducting Josephson junctions today are some type of the last example [46].

2.4.1 Josephson Junctions

As discussed above, a Josephson junction is some kind of weak link separating two superconductors. In appendix A1 we will examine the case of a superconducting-insulating-superconducting Josephson junction, for which Josephson's original work is based on. Similar results are found for other types of Josephson junctions [31].

One main result, assuming both a uniform magnetic field and voltage in the junction, is that the supercurrent density, J_S, across a Josephson junction is given by,

$$J_S = J_c \sin(\gamma) \tag{2.2}$$

where the gauge-invariant superconducting phase difference, γ, is given by,

$$\gamma = \theta_2 - \theta_1 - \frac{2\pi}{\Phi_0} \int \vec{A}(t) \cdot d\vec{l}, \tag{2.3}$$

for magnetic vector field, $\vec{A}(r,t)$, superconducting phase difference at the junction boundaries, $\theta_2 - \theta_1$, and critical current, J_c, which depends upon the superconducting material, weak link material and the geometry of the weak link. This is known as the DC Josephson effect because it shows when there is no magnetic field or voltage, there is a constant supercurrent across the junction. The other main result is that

$$\frac{\partial \gamma}{\partial t} = \frac{2\pi}{\Phi_0} V(t), \tag{2.4}$$

for applied voltage, $V(t)$. This is known as the AC Josephson effect because it shows a constant voltage produces a sinusoidal supercurrent. The Resistively and Capacitively Shunted Junction (RCSJ) model, where a Josephson junction is set up in parallel with a resistor and a capacitor, is then used to build differential equations through the simple application of Kirchhoff's laws. Josephson junctions are often resistively shunted to avoid hysteresis and will often have a small self-capacitance so the model is physically relevant.

For use in measurements, a Josephson junction (or two) interrupts a superconducting loop. There are two important cases for the inductance, L of the loop; the inductive mode, where $\frac{I_c R^2 C}{\Phi_0} \ll 1$, and the dissipative mode, where $\frac{I_c R^2 C}{\Phi_0} \geq 1$. In the inductive mode, the Josephson junction acts as an inductor and is usually the mode DC SQUIDS are used in. In the dissipative mode, a bias current provides enough flux for the flux in the SQUID to increase by one or more magnetic flux quanta. A plot of the voltage across the loop versus applied current shows the voltage increases in steps called Shapiro steps (see Fig. 2.5(a)), demonstrating that energy is being dissipated. An RF SQUID is normally used in the dissipative mode. For the inductive mode the voltage is given by,

$$V = R\sqrt{I^2 - I_c^2}, I > I_c \tag{2.5}$$

and V = 0 for a bias current less than the critical current, I_c. We can now examine how a SQUID measures magnetic flux.

2.4.2 DC SQUID

A direct current (DC) SQUID is formed from a loop of a superconducting wire with two Josephson junctions as shown in Fig. 2.2. A bias current, I, flows through the loop with half of the current traveling through each junction. A magnetic field, B, is applied and induces a current, J, around the loop. Using the RSCJ model it can be shown (appendix 2.4.3) that the sum of the currents through the two Josephson junctions is given by,

$$I = 2I_c \sin(\gamma) \cos\left(\frac{\pi \Phi_a}{\Phi_0}\right). \tag{2.6}$$

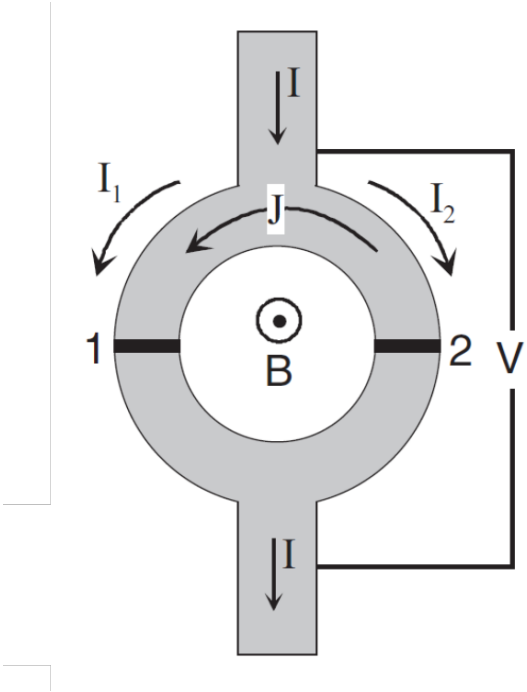

FIGURE 2.2: DC SQUID in an applied magnetic field B. The bias current, I, is split equally across the two branches of the loop while the magnetic field induces a current J around the loop. Reused from [50] with permissions

When the SQUID loop has no inductance and the Josephson junctions have no capacitance, the voltage across the loop is given by

$$V = R\sqrt{I^2 - I_c^2 \cos^2\left(\frac{\pi\Phi_a}{\Phi_0}\right)}, \tag{2.7}$$

where R is the resistance of the resistor in parallel with the Josephson Junction, I_c is the critical current of the Josephson junction, and ϕ_a is the applied flux. That is, the voltage is periodic in the applied flux with period Φ_0. It can be shown that the peak-to-peak voltage is largest when the bias current is equal to $2\ I_c^2 \cos^2\left(\frac{\pi\Phi_a}{\Phi_0}\right)$ and it is readily seen that the derivative attains a maximum at $(2n+1)\frac{\Phi_0}{4}, n = 0, 1, 2...$. Including capacitance and inductance does not change that the voltage is periodic in the applied flux with period Φ_0 but the functional form of the I-V curve is slightly modified.

We will now describe how to measure the magnetic flux due to a sample with a DC SQUID. The bias current across the SQUID is fixed to maximize the peak-to-peak voltage while a feedback loop is inductively coupled to the SQUID and used to maintain the applied flux at $\frac{\Phi_0}{4}$, to produce what is known as a flux-locked loop. As a sample is moved through the detection coils, a current in the feedback loop produces a negative

flux in the (SQUID) loop to cancel the flux from the sample. Measuring the feedback current (or voltage required to produce this current) allows the magnetic flux from a sample to be determined to $\approx 10^{-5}\Phi_0$. This requires the use of fast electronics to change the feedback current. DC SQUIDs will also incorporate a modulation coil driven with an alternating current of a few kHz[46]. Fig. 2.3 shows a block diagram of a DC SQUID. Note that the detection coil, through which a sample travels, is not shown but it would be attached to the input coil. This is done so that the SQUID is not exposed to temperatures/fields which may damage the device.

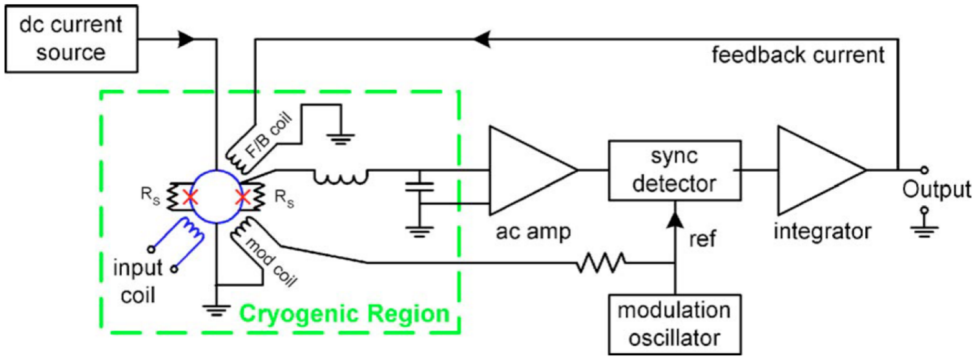

Figure 2.3: A block diagram of a DC SQUID. The input coil, feedback coil, and modulation coil are all inductively coupled to the SQUID. Josephson junctions are represented as red X's that are resistively shunted. Reused from [46] with permissions

2.4.3 RF SQUID

A radio-frequency (RF) SQUID makes use of a loop with a single Josephson junction inductively coupled to an AC circuit incorporating an inductor, capacitor(s), and resistor(s), depending on the setup. Historically and in many modern SQUIDS, the AC tank is driven near the fundamental frequency, ω_f of the circuit for which $1/\omega_f$ is much less than the time scales associated with the SQUID device. This is known as the adiabatic regime [31]. The system is also run in what is known as the dissipative regime where the amplitude of the current, I_{RF}, is chosen such that $2\pi L I_{RF} \geq \Phi_0$. Just above this current the SQUID flux discontinuously increases and then decreases by one flux quantum during each 1/2 AC cycle, while absorbing energy from the AC tank. If the AC drive is sinusoidal and the DC flux is an integer number of flux quanta then, during one cycle, the total flux as a function of applied flux will follow a double hysteresis loop, indicated by the path ABCDEFGHA shown in Fig. 2.4(a). A sketch of the Gibbs free energy is shown in Fig. 2.4(b) to help the reader understand the double hysteresis loop behaviour. After the double hysteresis loop, the current of the AC tank is lowered, requiring approximately Q cycles, where Q is the quality factor of the circuit, to increase the current back to the desired I_{RF}. The current in the tank is reduced during the first hysteresis loop so, in reality, the current amplitude needs to be large enough to drive the SQUID around

the double hysteresis loop including losses. Increasing the current amplitude sufficiently causes more hysteresis loops to occur during each AC cycle. To understand why this is

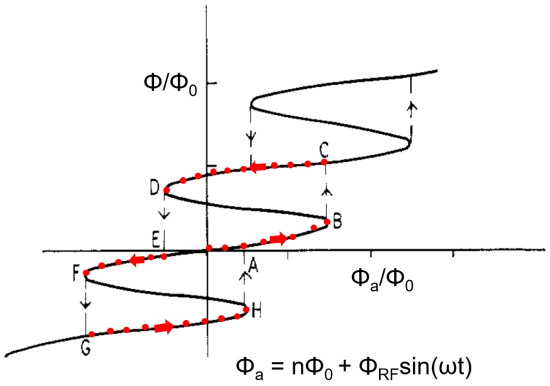

(A) Flux in the SQUID loop as a function of Φ_{RF} (I_{RF}) when the amplitude of I_{RF} is large enough to drive the SQUID through a double hysteresis loop. Red arrows and dots indicate the path traced out ABCDEFGHA. Adapted from [50].

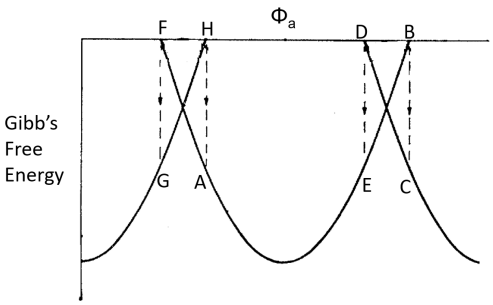

(B) Sketch of the Gibbs Free Energy as a function of Φ_a. Adapted from [116].

called the dissipative mode, a plot of RF voltage as a function of current amplitude is shown in Fig. 2.5(a), demonstrating plateau's, known as Shapiro steps [31, 131], where the SQUID is effectively dissipating energy from the AC tank. Point 3 in Fig. 2.5(a) corresponds to the double hysteresis loop previously discussed. During use, the current amplitude is chosen such that the voltage lies on a plateau, and examining the voltage as a function of DC flux for different values of the current amplitude (Fig. 2.5(b)) allows us to choose the best value. We can see that for current amplitudes 2 and 4, there is no sensitivity to the DC flux we would like to measure. Current amplitudes 1, 3, and 5 have the largest peak-to-peak voltage as a function of DC flux and therefore offer the most sensitivity. Operation of an RF SQUID is usually as follows; the AC amplitude is chosen such that one double hysteresis loop occurs during an AC cycle (3 in figures

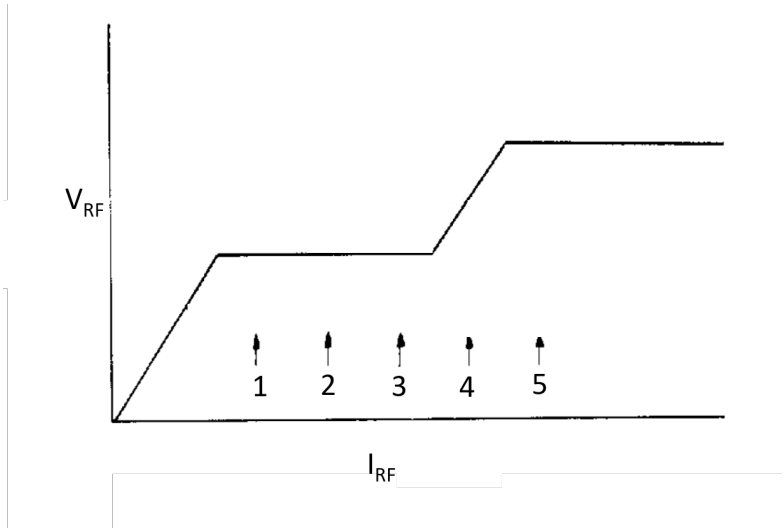

(A) Amplitude of the detected V_{RF} as a function of the current amplitude I_{RF} showing Shapiro steps. The SQUID effectively dissipates energy when operated on a plateau. Adapted from [50].

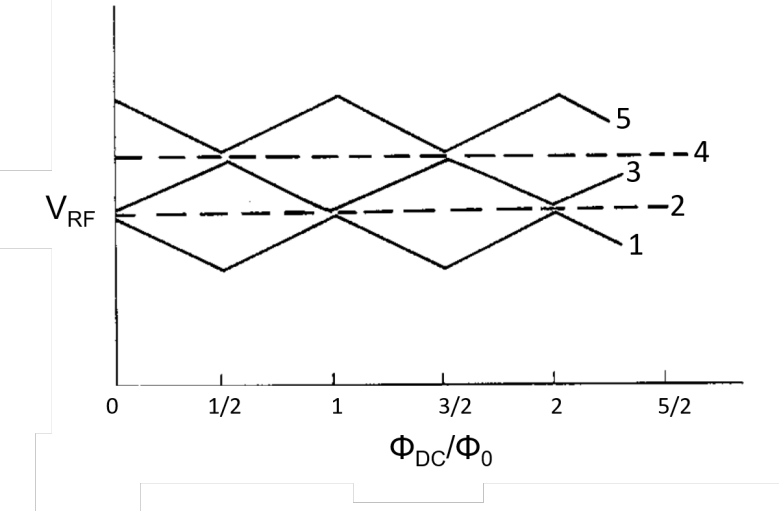

(B) The detected voltage amplitude, V_{RF} as a function of Φ_{DC} for the current amplitudes indicated in (a). Adapted from [50].

2.5(a) and 2.5(b)) while a DC feedback current is used to cancel the flux produced by the sample, and is the quantity measured. The SQUID is flux-locked at a working point $\frac{n\Phi_0}{2}$ for integer n, where $\frac{\partial V_{RF}}{\partial \Phi_{DC}}$ is discontinuous. This allows for a sensitive measurement of the DC feedback current and hence magnetic flux due to the sample. A block diagram of an RF SQUID is shown in Fig. 2.6.

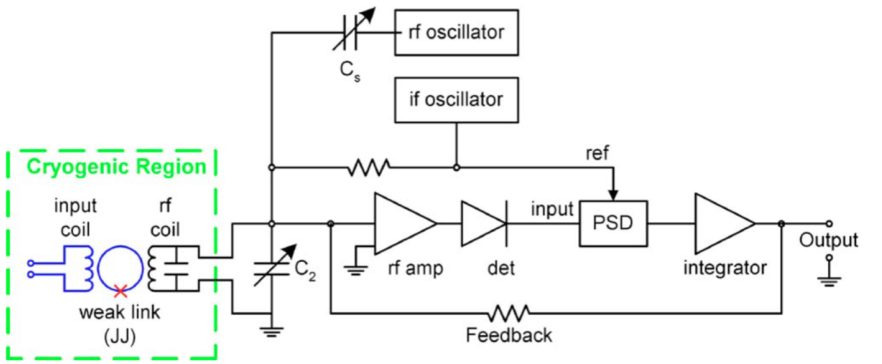

FIGURE 2.6: Block diagram of an RF SQUID. The RF oscillator produces the MHz RF signal while the IF oscillator modulates the signal in the kHz range and provides a reference for phase-sensitive detection (PSD). The RF coil and input coil are both inductively coupled to the SQUID loop where the Josephson junction is shown as a red X. Reused from [46] with permissions. .

2.4.4 SQUID Measurements at McMaster

At McMaster, a Quantum Design MPMS 5 RF SQUID is used for magnetometry and susceptibility measurements with applied fields from 0 to 7 Tesla with temperatures ranging from 2 to 400 K. A He^3 insert may be placed into the sample space to allow for measurements down to 0.5 K. An AC option is included allowing for measurements in an oscillating field of up to 3 Oe from 0.1 to 1000 Hz. Finally, measurements as a function of pressure may be performed using a GC10/3 gas pressure cell from the Institute of High Pressure Physics, Polish Academy of Sciences, inserted into the MPMS allowing for magnetometry measurements under pressure up to 700 MPa, above 2 K.

In a direct current (DC) measurement, a constant magnetic field is applied to the sample and detection coil and the sample is moved through the detection coil. The detection coil in this system is a second-order gradiometer where a clockwise oriented loop is placed in series with two counter-clockwise loops 3 cm away followed by another clockwise loop 3 cm away as shown in Fig.2.7. The advantage of a second-order gradiometer is that it will cancel out the flux due to a spatially homogeneous field as well as the flux due to a field that varies linearly with distance, thus removing almost all of the flux due to an applied magnetic field. The output of the measurement is the voltage required to keep the SQUID flux-locked at the desired working point as a function of distance, shown on the right in Fig. 2.7. This voltage curve is then compared to carefully calibrated voltage curves for a known magnetic sample, usually a specific cylinder size of palladium. From this comparison, the magnetic moment of the sample is given in emu.

In an alternating current (AC) measurement, where the applied field varies with some frequency, the sample is held in the center of the detection coil as the field varies over one

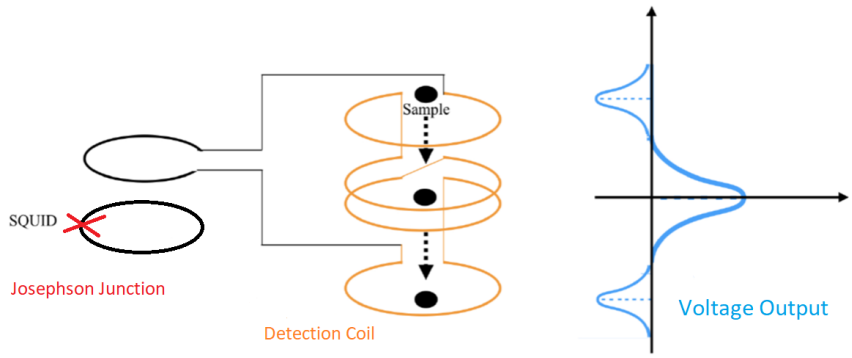

FIGURE 2.7: DC SQUID measurement showing the detection coil (orange), SQUID (black), Josephson junction (red X), and voltage output (blue) as the sample is moved through the detection coil. Adapted from [20].

or more periods. The sample is then moved away from the detection coil and a measurement is taken for use as background subtraction and comparison. There is a hierarchy of time/frequency scales that limits the maximum frequency that can be measured. The SQUID cutoff frequency is $\frac{R_{SQUID}}{L_{SQUID}}$ where, R_{SQUID} is the resistance of the SQUID and L_{SQUID} the inductance, while the characteristic frequency of the Josephson junction is $\frac{2\pi R_{SQUID} I_0}{\Phi_0}$. The parameters of the SQUID are usually chosen so that the lower of these two frequencies is ≈ 10 GHz. Therefore to be in the adiabatic regime the AC tank inductively coupled to the SQUID should be made to have a fundamental frequency $\approx$ 10 MHz, at maximum. The oscillating applied field needs to be approximately constant during one double hysteresis loop of the SQUID which occurs with the same frequency as the AC tank is driven (MHz). This limits the applied field to frequencies below about 1 kHz. Since the applied field is approximately constant during the double hysteresis loop, an AC measurement is in reality a series of DC measurements taken as the applied field oscillates. The feedback voltage required to cancel the sample flux is measured as a function of time over one or more periods and compared to the feedback voltage required to cancel the flux from only the applied AC field. From this an amplitude and phase shift due to the sample are determined and are related to the real and imaginary susceptibilities of the sample.

2.5 Muon Spin Rotation, Relaxation, and Resonance

Muon Spin Rotation, Relaxation, and Resonance is a technique that is extremely sensitive to the internal magnetic fields of a material. The method relies on the Larmor precession of spin-polarized positive muons that stop in a magnetic material and decay into positrons with a characteristic lifetime of $\tau_\mu = 2.2$ μs. The large gyromagnetic ratio of the muon, $\gamma_\mu = 135.54$ MHz/T, means that it is possible to measure internal fields

as small as ≈50 mG. The muon not only probes the magnitude of the internal field but also the shape of the field distribution, the volume fraction of different magnetic (or non-magnetic) phases, and the dynamics of the magnetism [91].

2.5.1 Muon Production

Muons used in μSR experiments require reasonably sized particle accelerators to be generated. Protons are accelerated and collide into blocks of either graphite or beryllium; a material that will mostly disperse the energy by producing a large number of pions. At TRIUMF in Vancouver, Canada, H^- ions are accelerated by a cyclotron to $\approx$ 520 MeV and collide into graphite. The graphite very quickly strips the two electrons from the proton which then interacts with the nucleons of the graphite to produce pions. Pions are spin-0 particles of which there are three kinds, π^+, π^-, and π^0 that have positive, negative, and neutral electric charges, respectively. Single pion production is the only relevant production method at these energies of which there are two relevant processes to produce positive pions given below.

$$\begin{aligned} \mathrm{p} + \mathrm{p} &\rightarrow \mathrm{p} + \mathrm{n} + \pi^+ \\ \mathrm{p} + \mathrm{n} &\rightarrow \mathrm{n} + \mathrm{n} + \pi^+ \end{aligned}$$

We will ignore the production of π^0 and π^- as their decay products will be steered away from or out of the muon beamlines. π^+ will decay into a positive muon and a muon neutrino via the weak force. The 100% parity-violating weak force demands that the (nearly) massless spin-1/2 neutrino decays with its spin anti-parallel to its momentum and so when a π^+ decays at rest, the spin-1/2 muon must travel in the opposite direction with its spin also anti-parallel to its momentum, to conserve both momentum and angular momentum as shown in Fig. 2.8. The decay results in a unique energy and momenta for the muon of 4.1 MeV and 29.788 MeV/c, respectively. These muons are called surface muons and steering/focusing magnets are used to direct these muons to the sample while non-surface muons and other particles are rejected.

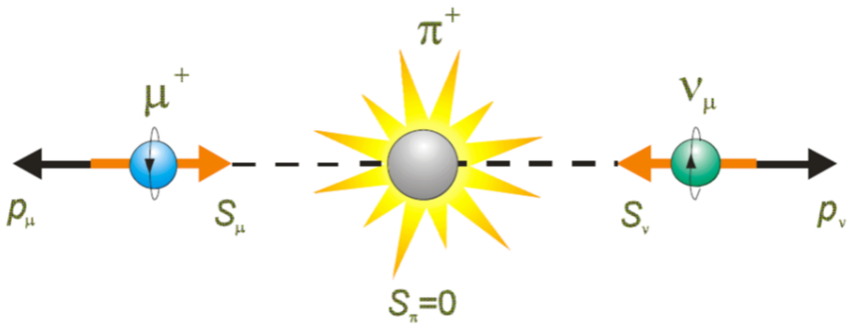

FIGURE 2.8: Positive pion, π^+, decay at rest into a positive muon, μ^+, and a muon neutrino, ν_μ. Adapted from [119].

There are two types of muon sources around the world; pulsed and continuous. Pulsed sources, such as that at ISIS in Oxfordshire UK, deliver a large number of muons (bunches) to a sample within a time window $\Delta t \ll \tau_\mu$ ($\approx$ 80 ns at ISIS). The bunches are delivered with a time separation $\gg \tau_\mu$ (20 ms at ISIS [32]). A timer is started when the bunch enters the sample and detector counts as a function of time are recorded as the muons decay. In a continuous muon source, such as at TRIUMF in Vancouver BC, muons are implanted in a sample one at a time. Events where two muons enter the sample space within $\approx$10 τ_μ, are rejected and the rate of muon implantation is modulated such that 1 muon enters the sample approximately every 10 τ_μ. In this way each positron detected can be identified with a specific muon decay. In a pulsed source, the uncertainty in implantation time (Δt) means that very fast relaxations are hard to measure, however, as the time separation between bunches is very large the beam-borne background is negligible. A pulsed source can therefore measure up to 10 τ_μ or longer depending on how long data is collected, allowing extremely small relaxation rates to be measured. At a continuous source, beam borne background means that the data collected beyond about 10 μs has a relatively low signal-to-noise ratio and therefore cannot measure as small of relaxation rates as a pulsed source. A continuous source however can measure relaxation rates approximately 5-10 times faster than a pulsed source due to the small uncertainty in implantation time.

2.5.2 Muon Decay

An implanted muon decays with a characteristic lifetime of 2.2 μs of which the dominant ($\approx$99%) process is,

$$\mu^+ \rightarrow e^+ + \nu_e + \bar{\nu_\mu},$$

where ν_e and $\bar{\nu_\mu}$ are the electron neutrino and muon antineutrino, respectively. Energy and momentum conservation implies the positron will have a maximum energy, E_{max}, of 52.3 MeV [32] and a calculation from electro-weak theory gives the double differential distribution, $W(\theta, \epsilon)$, of the decay of positrons with respect to the spin of the muon as,

$$d^2W = W(\theta,\epsilon)\, d\epsilon\, d\cos(\theta) = \frac{G^2 m_\mu}{192\pi^3}(3-2\epsilon)\,\epsilon^2\left[1+\frac{2\epsilon-1}{3-2\epsilon}\cos(\theta)\right] d\epsilon\, d(\cos(\theta)), \quad (2.8)$$

where G is a coupling constant, $m_\mu = 105.7$ MeV/c^2 is the muon mass, and $\epsilon = \frac{E}{E_{max}}$. We are interested in the term inside of the square brackets,

$$a(\epsilon) = \frac{2\epsilon-1}{3-2\epsilon}, \quad (2.9)$$

known as the asymmetry parameter. For decay positrons in the same plane as the muon spin the rate, $\frac{dN}{d\theta}$, is proportional to [32],

$$\frac{dN}{d\theta} \propto (1 + a(\epsilon)\cos(\theta)), \tag{2.10}$$

which is shown in Fig 2.9 for various values of ϵ with the distribution of positrons for the highest energy shown in blue. Averaging over all energies gives a = 1/3 and produces

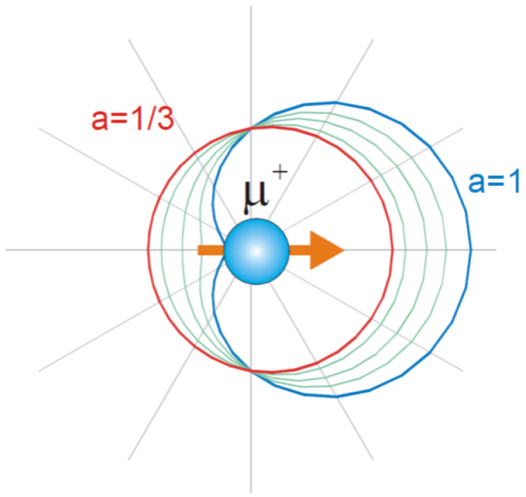

FIGURE 2.9: The positron decay distribution as a function of angle for various energies. Blue is the distribution for the highest energy positrons while averaging over all energies leads to the orange distribution [119]. .

the orange curve in Fig. 2.9, a circle centered at 1/3. Averaging this distribution over all angles leads to a 1/3 excess in the direction of the muon spin. That is, given an ensemble of muons with the same polarization function, P(t), a reduced muon polarization of amplitude 1/3 P(t) is (theoretically) detected.

To probe the longitudinal muon relaxation function, $P_z(t)$ we need to compare the positron counts in two detectors; one detector that is in the opposite direction of the muon momentum, relative to the sample which we label the "backward" detector with detector counts, N_B and the "forward" detector in the opposite direction relative to the sample with detector counts N_F. In an idealized case, we can make the conceptually useful definition of the asymmetry, A(t), of the two detectors as,

$$A(t) = \frac{N_B(t) - N_F(t)}{N_B(t) + N_F(t)} = \frac{1}{3}P_z(t), \tag{2.11}$$

the normalized difference between the two detectors.

This idealized case does not take into account any beam-borne background, B_i, detector efficiency ϵ_i, or intrinsic asymmetry A_i, for detectors i = F, B, the forward and backward detectors. The number of counts in each detector can then be written as,

$$N_{B,F} = B_{B,F} + N_0 \epsilon_{F,B} \left[1 \pm A_{B,F} P_z(t)\right], \tag{2.12}$$

where N_0 is is a common normalisation [32]. Subbing these into Eq. 2.11 and assuming negligible beam-borne background it can be shown [32],

$$A(t) = \frac{N_B(t) - \alpha N_F(t)}{N_B(t) + \alpha N_F(t)} = A_B P_z(t), \tag{2.13}$$

where $\alpha = \frac{\epsilon_F}{\epsilon_B}$ and A_B usually takes values between 0.2-0.27. α is determined experimentally by performing a weak transverse field (wTF) measurement.

2.5.3 Muon Relaxation Functions

We have discussed how muons are produced and how they decay but we have yet to explain what happens to a muon while implanted in a sample. When the muon enters the sample it is very quickly ($\approx 10^{-10}$s) captured through the following successive process; ionisation of atoms and scattering of electrons (4 MeV $\rightarrow \approx$2 keV), muonium formation through successive electron capture and loss (2 keV $\rightarrow$ 50 eV), muonium-atom collisions (50 eV $\rightarrow$ a few eV) and finally the muonium dissociates into a free muon which (normally) stops in the most electronegative site. In insulators, this is near oxygen atoms and therefore the muon stops in an interstitial site. Symmetry is often able to give a general idea of the position of muon stopping sites but to know the number of stopping sites and their position accurately requires density functional theory.

We briefly contrast this with the behaviour of a negative muon which acts like a heavy (negative) electron. In this case, the negative muon implants in the same way as a positive muon except it typically is captured by positive ions. As muons are different particles than electrons, the Pauli exclusion principle does not apply, and the negative muon is free to fall to the lowest excited state. A use of negative muons is to catalyse certain fusion reactions [32]. Everywhere else in the thesis, assume that a muon refers to a positive muon, unless otherwise noted.

The magnetic dipole moment, $\vec{\mu} = \gamma_\mu \vec{S}$, of a muon changes due to the torque, $\vec{G}$, it experiences from a magnetic field. That is,

$$\frac{\partial \vec{\mu}}{\partial t} = \vec{G}, \tag{2.14}$$

where γ_μ is the gyromagnetic ratio of the muon. The torque experienced by the muon is equal to $\vec{G} = \vec{\mu} \times \vec{B}$, leading to the Larmor equation,

$$\frac{\partial \vec{S}}{\partial t} = \gamma_\mu \vec{S} \times \vec{B}. \tag{2.15}$$

If $\vec{B}$ is in some direction with angle θ relative to the S_z axis then [32],

$$S_z = \cos^2(\theta) + \sin^2(\theta)\cos(\gamma_\mu |B| t). \tag{2.16}$$

This is the precession a single muon experiences in a field $\vec{B}$ but what we are interested in is the average behaviour of an ensemble of muons precessing in a local field distribution, $\rho(\mathrm{B}_{loc})$, at the muon site(s). $\rho(\mathrm{B}_{loc})$ is a probability distribution; the probability the sample produces a field $\vec{B_{loc}}$ at the muon site. The muon longitudinal relaxation function is then given by [106],

$$P_z(t) = \int S_z\left(t, \vec{B_{loc}}\right)\rho\left(\vec{B_{loc}}\right) d\vec{B_{loc}}. \tag{2.17}$$

Replacing S_z with $S_{x,y}$ in Eq. 2.17 gives the transverse relaxation function. Note that this is the relaxation function at a single muon site; if there are multiple inequivalent muon sites the relaxation function is a weighted sum of the relaxation functions at each individual muon site.

The simplest case is where the material fully magnetically orders and $|B|$ takes a single, static, value (i.e. $\rho(B_{loc}) = \delta(B - B_{loc})$). In this case, the relaxation function is given by [32],

$$P_z(t) = \frac{1}{3} + \frac{2}{3}\cos(\gamma_\mu |B_{loc}| t). \tag{2.18}$$

Two other important field distributions are the Gaussian and Lorentzian field distributions,

$$\rho_i^{Gaus}(B_{loc}) = \frac{\gamma_\mu}{\sqrt{2\pi}\Delta}\exp\left(-\left(\frac{\gamma_\mu B_i}{\sqrt{2}\Delta}\right)^2\right), \quad i = x, y, z \tag{2.19}$$

and

$$\rho_i^{Lor}(B_{loc}) = \frac{\gamma_\mu}{\pi}\frac{a}{a^2 + \gamma_\mu^2 B_i^2}, \quad i = x, y, z \tag{2.20}$$

respectively. Both distributions have an average value of zero but differ in their shape. The Gaussian distribution function tends to describe concentrated, dense magnetic systems fairly well while the Lorentzian distribution tends to describe dilute magnetic systems well [32]. Substituting the Gaussian distribution into Eq. 2.17 leads to,

$$P_z^{Gaus} = \frac{1}{3} + \frac{2}{3}\left(1 - \Delta^2 t^2\right)\exp\left(-\frac{\Delta^2 t^2}{2}\right) \tag{2.21}$$

while a similar form is found for the Lorentzian distribution [75]. Both functions bear the names of Kubo and Toyabe who derived them in 1966 [75]. The underlying assumption of the model is that the magnetic field is randomly oriented and averages to zero over all muon sites with a spread in the distribution of magnetic fields that has Gaussian width Δ or Lorentzian width a. It turns out that in ZF a 1/3 non-relaxing component and 2/3 relaxing component is common for all randomly, statically ordered magnetic systems. By symmetry, on average 1/3 of the randomly oriented field must lie along the muon

spin direction and therefore cause no relaxation or oscillation. Similarly, on average 1/3 of the randomly oriented field must lie along one of two perpendicular directions, causing relaxation/oscillation. Combining the two directions gives the factor of 2/3 which relaxes or oscillates. The 1/3 component, or "1/3 tail" only relaxes (decays) in the presence of dynamic processes. Dynamic processes are also much more robust against decoupling due to an applied longitudinal magnetic field (LF).

In the presence of an applied LF, the Gaussian Kubo-Toyabe function is modified to [63],

$$P_z^{Gaus}(t,\omega_L) = 1 - \frac{2\Delta^2}{\omega^2}\left(1 - e^{\left(-\frac{1}{2}\Delta^2 t^2\right)}\cos\left(\omega_L t\right)\right) + \frac{2\Delta^4}{\omega_L^3}\int_0^t e^{\left(-\frac{1}{2}\Delta^2\tau^2\right)}\sin\left(\omega_L\tau\right)d\tau, \tag{2.22}$$

where $\omega_L = \gamma_\mu B_L$ is due to the applied LF. As the applied LF gets very large it dominates over any local static fields due to the sample and since the muon polarization is along this direction, very little relaxation occurs. Fig 2.10 shows how the relaxation function changes as the LF is increased. The main consequence of applying an LF to static

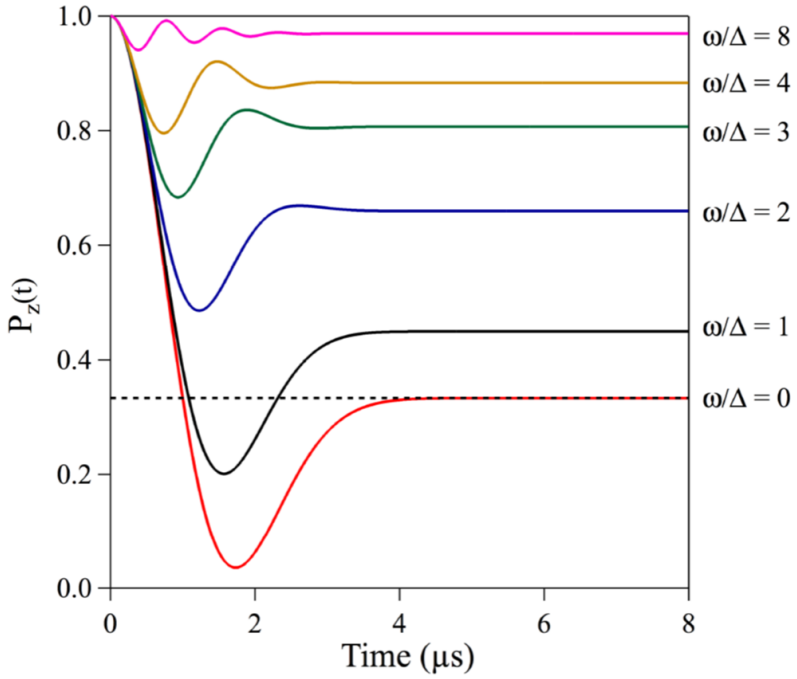

FIGURE 2.10: The effect of applying a longitudinal field, with $\omega = \gamma_\mu B_L$, on the μSR relaxation function. Reproduced from [20] with permission.

magnetic moments is to raise the tail of the relaxation function. This rough result is true across all static magnetic distribution functions, $\rho(B)$ [32].

We now consider the effect of fluctuating magnetic fields with fluctuation rate, ν, on the muon relaxation function. The strong collision approximation is often used to model

the behaviour of fluctuating fields. In this approximation, the local field instantaneously changes its direction at a time, t, with a probability distribution, $\rho(t) \propto \exp(-\nu t)$. The field after such a change is assumed to not correlate with the field beforehand and is chosen randomly from the probability distribution $P(B)$ [32]. The polarisation first decays following the Kubo-Toyabe function until time t_1 where the spin randomly changes and the polarization again follows a Kubo-Toyabe form until time t_2, when another change happens. This process repeats until the muon decays. Mathematically, these operations lead to a series of convolutions multiplied by an exponential decay,

$$G_z^{Gaus}(t,\nu,\Delta) = \exp(-\nu t)\sum_{n=0}^{\infty}\nu^n\left(P_z^{Gaus}(t,\Delta) * P_z^{Gaus}(t,\Delta)\right)^n, \tag{2.23}$$

where $\left(P_z^{Gaus}(t,\Delta) * P_z^{Gaus}(t,\Delta)\right)^n$ is the static Gaussian Kubo-Toyabe function (Eq. 2.21) convoluted with itself n times and we define $\left(P_z^{Gaus}(t,\Delta) * P_z^{Gaus}(t,\Delta)\right)^0 = P_z^{Gaus}(t,\Delta)$. Progress can be made by using properties of the Laplace transform (namely the convolution theorem to turn the above equation into a geometric series) however, in general there is not an analytic solution and numerical evaluation is required. There are

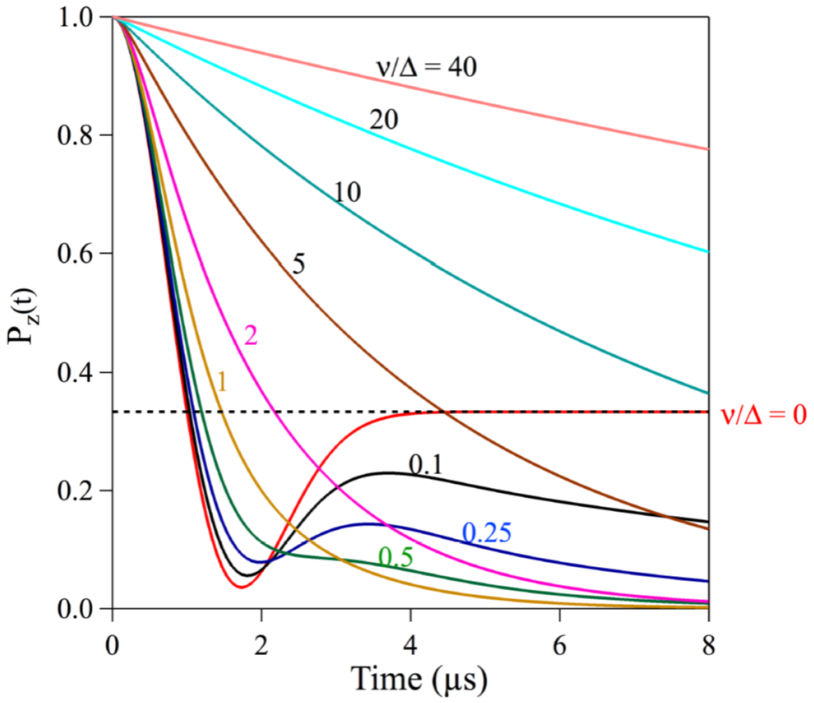

FIGURE 2.11: The effect of a fluctuating local field with fluctuation rate ν on the μSR relaxation function. Reproduced from [20] with permission.

two regimes in which simplifications can be made; the fast fluctuation ($\nu/\Delta \gg 1$) and

the slow fluctuation ($\nu/\Delta \ll 1$) regime. In the fast fluctuation regime, the relaxation function becomes exponential [32],

$$P_z\left(t,\nu,\Delta\right) = \exp\left(\frac{-2\Delta^2 t}{\nu}\right), \tag{2.24}$$

while in the slow fluctuation regime, the 1/3 tail is slowly relaxed out with,

$$P_z\left(t,\nu,\Delta\right) = \frac{1}{3}\exp\left(\frac{-2}{3}\nu t\right) + \frac{2}{3}\left(1-\Delta^2 t^2\right)\exp\left(-\frac{\Delta^2 t^2}{2}\right). \tag{2.25}$$

Fig. 2.11 shows how fluctuations change the relaxation function from a Gaussian Kubo-Toyabe function in the zero fluctuation limit to an exponential relaxation in the fast fluctuation regime. Finally, we consider the effects of applying an LF to a system with a fluctuating internal field shown in Fig 2.12. Comparing the LF required to

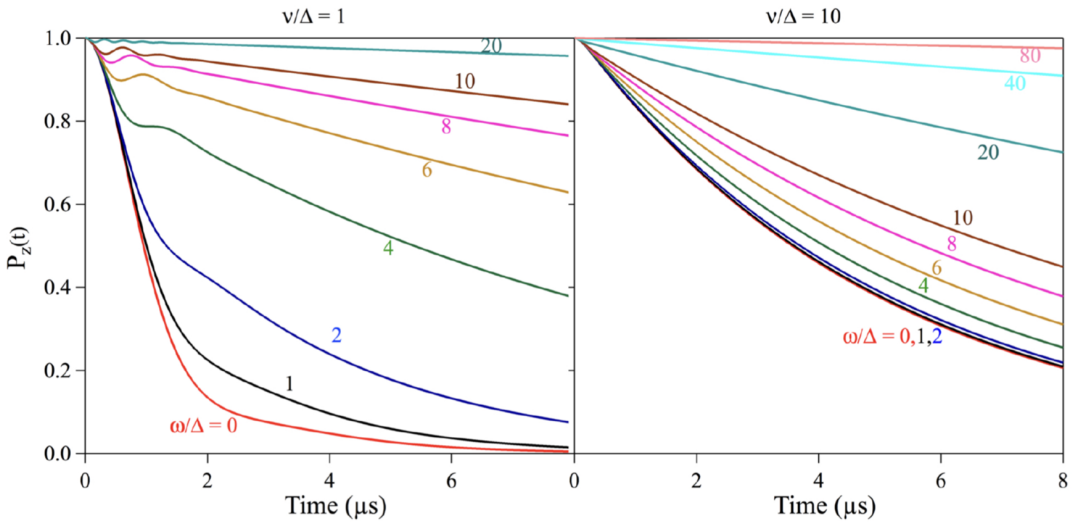

FIGURE 2.12: Left: the effect of a longitudinal field on the relaxation function of a Gaussian distributed, fluctuating local field with $\nu/\Delta = 1$ and right: $\nu/\Delta = 10$. Reproduced from [20] with permission.

decouple a fluctuating field (Fig. 2.12) with the LF required for a static field (Fig. 2.10) shows that dynamic magnetism is much more robust against decoupling than static magnetism. Thus a longitudinal field, ω_L, can be used to distinguish between disordered static magnetism, which may produce an exponential or stretched exponential behaviour, and dynamic magnetism. Further, in the fast fluctuation regime, additional information can be obtained about Δ and ν by measuring an LF sweep through the Redfield formula [32],

$$\lambda = \frac{2\Delta^2\nu}{\nu^2+\omega_L^2}. \tag{2.26}$$

Of special interest to this thesis is the relaxation functions produced by spin glass systems. The canonical spin glass systems are magnetically dilute alloys where the magnetic ion concentration is typically around 1-5%. Due to the variable nature of the spin concentration within a sample, there is a range of random fields associated with each muon site, i.e. there is a different width to the field distribution, Δ_j, at each muon site j which is probed with probability [134],

$$\rho\left(\Delta_j\right) = \sqrt{\frac{2}{\pi}}\frac{a}{\Delta^2}\exp\left(-\frac{a^2}{2\Delta^2}\right). \tag{2.27}$$

Uemura *et al.* [133] showed that in the presence of fluctuating moments with a single fluctuation rate, ν, the relaxation function takes on root-exponential behaviour,

$$P_z(t,\nu,a) = \exp\left(-\sqrt{\frac{4a^2t}{\nu}}\right), \tag{2.28}$$

in the motional narrowing limit $\nu/a \gg 1$. Further, in the presence of coexisting static and dynamic magnetism, where a fraction, Q, of the moments appear static to the muon at any one time, the relaxation function is given by,

$$P_z(t,\nu,a_s,a_d) = \frac{1}{3}\exp\left(-\sqrt{\frac{4a_d^2t}{\nu}}\right) + \frac{2}{3}\left[1 - \frac{a_s^2t^2}{\sqrt{\frac{4a_d^2t}{\nu} + a_s^2t^2}}\right]\exp\left(-\sqrt{\frac{4a_d^2t}{\nu} + a_s^2t^2}\right), \tag{2.29}$$

with $a_s^2 = Qa^2$ due to static magnetism and $a_d^2 = a^2 - a_s^2$ due to dynamic magnetism [133]. This function works well to describe the relaxation of canonical spin glasses [133], however, a key assumption is that there is only one fluctuation rate. While this is roughly true for alloys with dilute magnetic impurities at the % level, it breaks down for dense spin glasses [92]. In this case, there is a distribution of fluctuation rates above T_g, the freezing temperature, and the relaxation function is empirically found to be described by a stretched exponential,

$$P_z(t) = \exp\left(-\left(\lambda t\right)^{\beta}\right), \tag{2.30}$$

where the exponent β is a stretching parameter. Both β and λ are functions of temperature and just above T_g it has been experimentally found that the exponent varies from 1 at high temperatures, where a single relaxation rate is expected in the paramagnetic regime, to 1/3 just above T_g [21, 74, 41, 33, 123, 129]. A Monte Carlo study for 3-dimensional Ising spin glasses [93] found that above the transition, the autocorrelation function, which measures how correlated a spin is with itself at a later time, can be empirically fit by a stretched exponential at long time scales. The stretching exponent in this study varies from 1 at high temperatures and approaches 1/3 at the transition. Similar results exist for other XY and Ising spin-glasses [21].

Chapter 3

Gd_2ScNbO_7

3.1 Introduction

Gadolinium-based pyrochlore magnets originally garnered interest due to the theoretical infinite ground state degeneracy of the Heisenberg pyrochlore antiferromagnet that, to first order, a Gadolinium pyrochlore magnet may be described by [22, 23, 89]. This also applies to Gd_2ScNbO_7 that, in collaboration with Mauws *et. al.*, we study for the first time. The large magnetic moment of $\approx 8\ \mu_B$ for Gd^{3+} ions make dipolar interactions non-negligible and lifts the ground state degeneracy in real Gadolinium pyrochlores. Including dipolar interactions, the system is theoretically expected to order into a 4 sublattice ordered state with ordering wavevector k = (0, 0, 0) [58, 97]. A mixture of the excited ${}^6S_{\frac{7}{2}}$ and ground ${}^8S_{\frac{7}{2}}$ atomic states induces a single-ion anisotropy with energy separation comparable to the exchange interactions [53]. Specific to Gd_2ScNbO_7, we must consider the effect disorder has on these systems which have several different competing interactions. The combination of competing interactions, frustration, and disorder might be expected to induce spin-glass behaviour, which our results strongly support.

The related compounds $Gd_2Sn_2O_7$, $Gd_2Pt_2O_7$, and $Gd_2Ti_2O_7$, along with the theoretical reasons discussed above, motivate the study of disorder on these systems. $Gd_2Sn_2O_7$ is found [136, 16] to order into the theoretically expected state proposed in [97] at around 1 K. $Gd_2Pt_2O_7$ is found to order antiferromagnetically at a slightly higher temperature of 1.6 K, likely due to additional superexchange pathways opened up by empty *d*-shell orbitals in Pt^{4+} compared to Ti^{4+} and Sn^{4+} [58]. In contrast, $Gd_2Ti_2O_7$ has two transitions in zero field at 0.75 K and 1 K into partially ordered states [29, 16, 122]. The ordering wavevector is $\left(\frac{1}{2}, \frac{1}{2}, \frac{1}{2}\right)$ and/or its 3 possible symmetry-related wavevectors. It is experimentally difficult to determine the number of wavevectors that contribute to the magnetic structure. The structures are labeled 1-k, 2-k, 3-k, and 4-k based on the number of wavevectors that contribute. There has been much debate as to which structure this material takes. Originally the 1-k structure was proposed as the low-temperature ground state [29], followed by the 4-k structure [122] and more recently the 2-k structure [96, 70]. The striking difference between the naively expected, similar behaviour of

$Gd_2Ti_2O_7$ and $Gd_2Sn_2O_7$ is due to differences in third nearest neighbour interactions [136, 36].

It is obvious that many different interactions are important in these systems; first, second, and third nearest neighbour interactions, single-ion anisotropy, and dipolar interactions all contribute to the behaviour of the system. Introduction of disorder into the system would seem likely to induce spin-glass behaviour, however, insulating, dense spin-glass systems are less explored than their metallic, dilute counterparts making Gd_2ScNbO_7 an interesting study to probe spin-glass physics. We compare the behaviour of Gd_2ScNbO_7 with the nominally disorder-free spin-glass pyrochlore magnet $Y_2Mo_2O_7$.

3.2 Methods

We have grown large single crystals of Gd_2ScNbO_7 using the optical floating zone technique. Polycrystalline rods were prepared using stoichiometric ratios of Gd_2O_3 (99.99%), Sc_2O_3 (99.999%), and Nb_2O_5 (99.99%). The polycrystalline rods were annealed in air at 1350°C for 48 hours, reground, and annealed an additional 48 hours under the same conditions. We grew a large single crystal from these rods by performing a pre-melt growth at 15 mm/hr in 6 atm of O2, the product of which, we regrew at 4 mm/hr in 6 atm of O_2. We have found that RE_2ScNbO_7 (RE = Gd, Tb, Dy) crystals tend to break apart during growth when grown too slowly ($\leq$10 mm/hr), however slower growth speeds tend to produce higher quality crystals. It was found that Gd2ScNbO7 crystals could be grown at a slower speed if a pre-melt growth was performed first. The phase purity of both powders and (crushed) crystals were confirmed with powder X-ray diffraction.

We performed DC and AC susceptibility measurements using a Quantum Design MPMS 5 Superconducting Quantum Interference Device (SQUID) with AC and ^{3}He options installed, providing a base temperature of 0.5 K. Our DC and AC measurements were performed on a single crystal of mass 49.35 mg. DC susceptibility was measured in a field of 100 Oe. AC susceptibility was measured with a field amplitude of 1 Oe and varying frequencies.

We performed Zero field (ZF) and longitudinal field (LF) μSR measurements on the M15 beamline at the TRIUMF Laboratory in Vancouver, Canada. We used a spectrometer incorporating a dilution refrigerator which allowed for measurements in the temperature range of 0.025-10K. The experimental set-up makes use of a superconducting magnet to allow for fields up to 5 T. We mounted the samples on a silver cold finger using copper grease (copper powder mixed with petroleum jelly) mixed with N grease to ensure good thermal conductivity. Silver gives a well-defined μSR background signal with very little relaxation. The instrument has a time resolution of 0.4 ns. We explored the effect of applied fields anti-parallel to the direction of the initial muon spin polarization (LF). We cut several discs of Gd_2ScNbO_7 from a single crystal such that the normal of the face of each disc lies along the (110) direction. This geometry means the initial muon polarization and any applied fields were along the (110) direction. We used the muSRfit software platform [125] to analyse the collected μSR spectra.

3.3 Results

3.3.1 Characterization

We performed a powder X-ray diffraction measurement on finely ground crystal from a section of our growth. Fig. 3.1(a) shows the results of our measurement with Reitveld refinement to a pyrochlore phase. There are no indications of any phase impurities. Fig 3.1(b) shows the Laue diffraction pattern along the (110) direction of a section of our as grown crystal. The crystal was translated along its length and width with no change to the Laue diffraction pattern, indicating that the sample is single crystal on a surface level. The crystal was then rotated 180 degrees and the same procedure was performed, with no change in the Laue diffraction pattern. The crystal was aligned and cuts were made perpendicular to the (110) direction. After cutting, we checked 3 pieces with Laue diffraction, one from the middle of the crystal and two from either end of the crystal, to confirm both the single crystal nature of the sample, and that alignment was maintained during cutting. Overall these results indicate a phase pure single crystal sample aligned along the (110) direction.

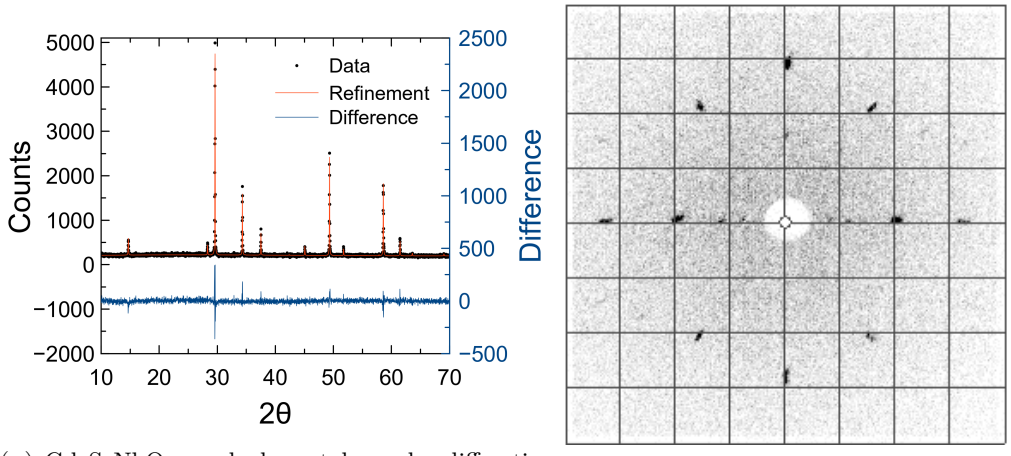

(A) Gd_2ScNbO_7 crushed crystal powder diffraction measurements with Reitveld refinement to the pyrochlore phase.

(B) Laue diffraction pattern from the (110) direction of our Gd_2ScNbO_7 single crystal.

FIGURE 3.1: Gd_2ScNbO_7 structural characterization.

3.3.2 SQUID Susceptibility

As a baseline to compare to other Gd^{3+} pyrochlores we performed DC susceptibility measurements from 0.5 K to 300 K in a field of 100 Oe as well as measurements at 0.5 K varying the Field from 0 to 7 T. The inverse susceptibility at high temperature is shown in Fig. 3.2(b) and is well described at all but the lowest temperatures by the Curie-Weiss law with Curie temperature -7.7 ± 0.1 K, indicating anti-ferromagnetic interactions, and an effective magnetic moment of 8.083 ± 0.006 μ_B. Gd^{3+} ions on the pyrochlore, having a very small single-ion anisotropy, should adhere to Curie-Weiss law over a wide range of

temperatures, as observed here. The low-temperature susceptibility (Fig. 3.2(a)) shows a ZFC/FC splitting at the transition temperature.

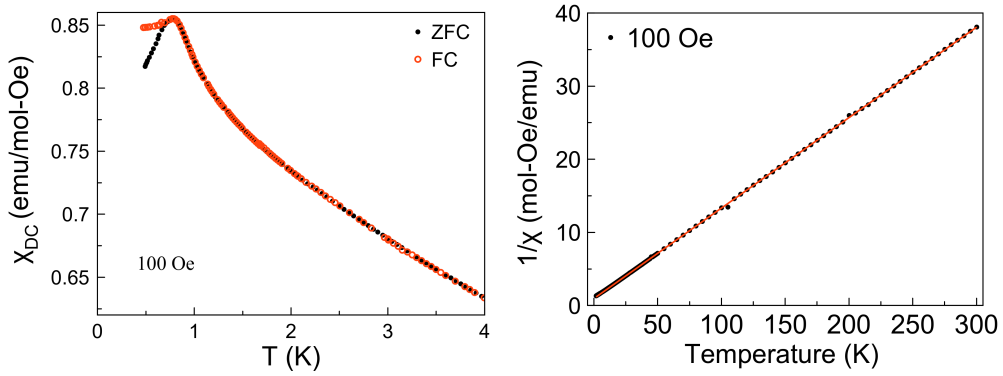

(A) DC Susceptibility from 0.5 K to 2 K measured in a 100 Oe field

(B) Inverse DC Susceptibility from 2K to 300K measured in a 100 Oe field

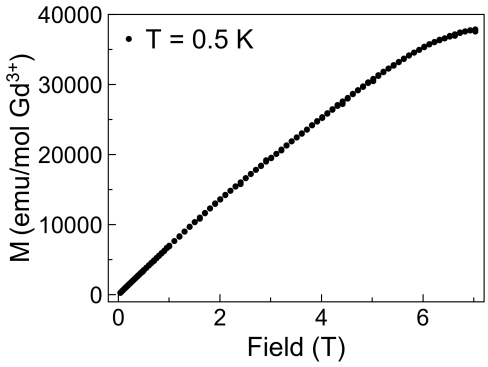

(C) Magnetic moment as a function of field at 0.5 K

FIGURE 3.2: Gd_2ScNbO_7 DC Susceptibility

We performed AC susceptibility measurements to probe the dynamics of the Gd^{3+} magnetic ions. The real part of the susceptibility, shown in figure 3.3(a), has a maximum that shifts to higher temperatures for higher frequencies. The Mydosh parameter is given by the relative shift in the transition temperature as a function of the change in log(frequency) and is used to distinguish between super-paramagnetism, canonical spin glasses, and cluster glasses [92]. We fit the peak in the real part of the susceptibility with a Gaussian function producing a Mydosh parameter of $\frac{\Delta T_F}{T_F \Delta \log(f)} = 0.020 \pm 0.001$ (Fig.3.3(c)), where T_F is the transition temperature and f is the frequency. The imaginary susceptibility, shown in Fig. 3.3(b), has a large increase in the high-frequency measurements below the transition seen in the real part of the susceptibility. The imaginary susceptibility is often related to absorption and dissipation of energy. A small error in the measured phase could mix some of the large signal from the real component into the imaginary component, however, this does not explain the temperature dependence of χ'' as the frequency increases. A peak in χ'' indicates that, at this temperature,

there are processes with an average relaxation time corresponding to 1/frequency [92, 66]. Accompanying a peak in χ'', χ' should exhibit an inflection point, however, our measurements are limited to temperatures above 0.5 K and we are unable to confirm this. In spin glasses, the dynamics of the system can produce a peak in χ'' and does not necessarily imply a thermodynamic transition [92, 66].

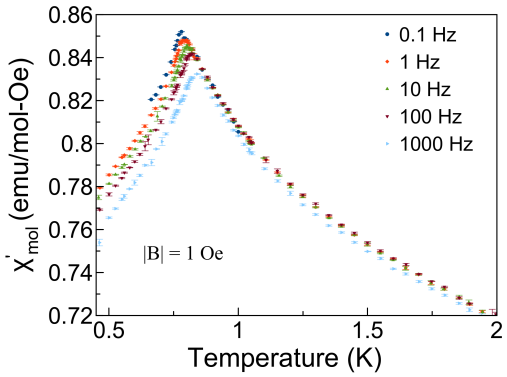

(A) Real susceptibility measured in varying driving frequencies

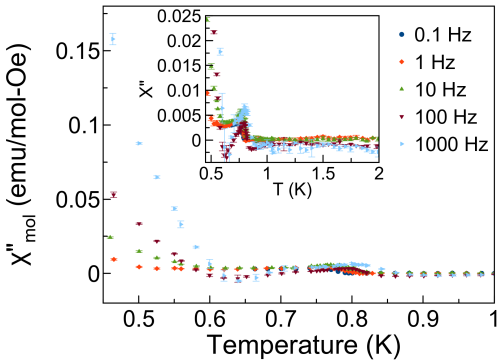

(B) Imaginary susceptibility for the same measurements as in (a)

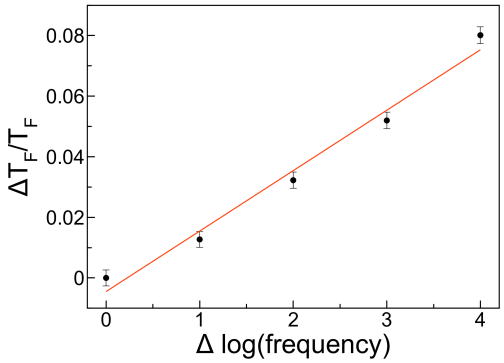

(C) Plot of the change in the normalized freezing temperature as a function of the logarithm of the change in frequency, fit by a straight line. The slope of this fit gives the Mydosh parameter, 0.020 ±0.001

FIGURE 3.3: Gd_2ScNbO_7 AC Susceptibility

3.3.3 μSR

We performed Muon Spin Rotation, Relaxation, and Resonance (μSR) measurements to probe both the static and dynamic magnetism within the sample. The zero-field asymmetries for high and low temperature are shown in Figures 3.4(a) and 3.4(b), respectively. Near the transition, a very fast relaxing component develops, indicative of the development of moments that are static on μSR timescales. This extreme relaxation at early times is also seen in the closely related compounds $Gd_2Ti_2O_7$ [39, 146],

$Gd_2Sn_2O_7$ [15], and $Gd_2Pt_2O_7$ [58]. As the temperature is lowered, the static relaxation becomes so fast that we can not accurately measure it with the μSR technique. We do not observe any Kubo-Toyabe like dip in the early time data nor any oscillations. Across all temperature ranges, the data is well fit by the asymmetry function,

$$A(t) = A_0 \left[\frac{1}{3}\exp(-(\lambda_D t)^\beta) + \frac{2}{3}\exp(-(\lambda_S t)^\beta)\right] + A_{bkg}\exp(-\lambda_{bkg} t), \tag{3.1}$$

where A_0 is the total initial asymmetry, λ_D is the relaxation due to dynamic magnetic moments, λ_S is the relaxation due to static moments, β is a stretching exponent commonly used to fit μSR data [32] and A_{bkg} and λ_{bkg} are the temperature-independent total asymmetry and relaxation of the background, respectively. We could not fit the data using a simple or Gaussian exponential for the dynamic relaxation, while, given the extremely fast relaxation of the static component, we could find a large range of values for β that could fit the data by changing the static relaxation rate. In principle, the exponent, β, does not need to be the same for the dynamic and static components of the relaxation but given that we expect a single component asymmetry in the paramagnetic state above the transition and that there is no strong evidence for a particular exponent for the static relaxation, we have chosen to use a single exponent for both. Above 0.8 K we found (approximately the transition temperature seen in AC susceptibility) the relaxation rates λ_D and λ_S begin to converge and track each other (not shown). Given that the data above 0.8 K is well fit by a single stretched exponential and that above a temperature close to the glass transition we expect only one signal component from fluctuating moments, we forced the relaxation rates λ_D and λ_S to be the same above 0.8 K, with the same exponent, β. It should be noted that a simple exponential can fit the high-temperature measurements but as the transition is approached from above, a simple exponential fails to describe the asymmetry. After imposing these requirements we essentially fit the data above 0.8 K to a single stretched exponential plus a temperature-independent background relaxation,

$$A(t) = A_0\exp(-(\lambda t)^\beta) + A_{bkg}\exp(-\lambda_{bkg} t). \tag{3.2}$$

The results of the fits are shown in Fig. 3.4. We find the relaxation (Fig. 3.4(c)) strongly increases as the transition is approached from above. At the transition, the static and dynamic relaxation rates diverge from one another (this has been confirmed by fitting all of the temperature points to Eq. 3.1), with the static relaxation, λ_S, increasing extremely rapidly until it can no longer be accurately measured. The dynamic relaxation, λ_D, is largest near the transition then decreases and possibly flattens out at low temperature. The stretching exponent, β, (Fig. 3.4(d)) is close to one at the highest temperatures (as would be expected in a fast fluctuating or paramagnetic regime) but as the transition is approached from above it rapidly decreases. Below the transition, the exponent roughly flattens out and forcing the exponent to be temperature independent below the transition describes the data well with $\beta = 0.354 \pm 0.008$.

We performed a temperature sweep in an applied field of 2 T to decouple a fraction of

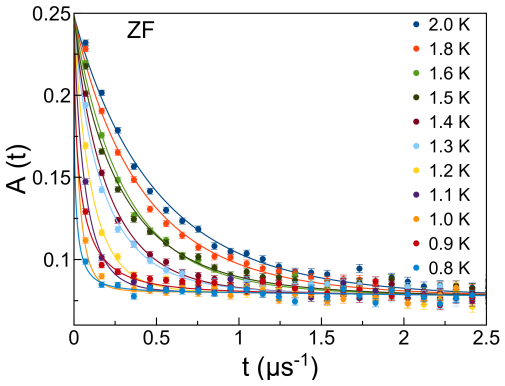

(A) μSR Zero Field data above the transition temperature fit to Eq. 3.2

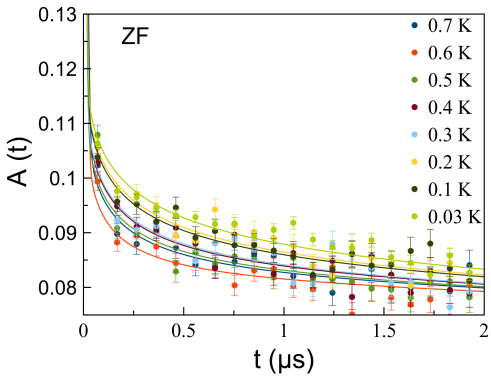

(B) Zero Field data below the transition temperature fit to Eq.3.1

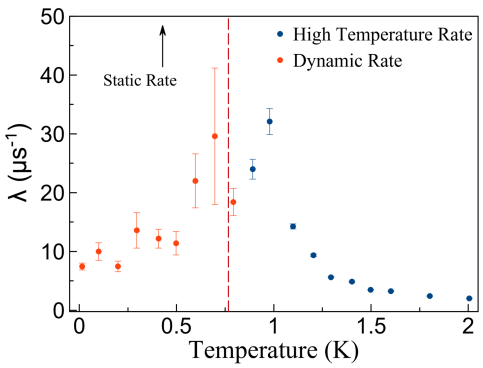

(C) Zero field relaxation rate. Note the static rate is far above the scale

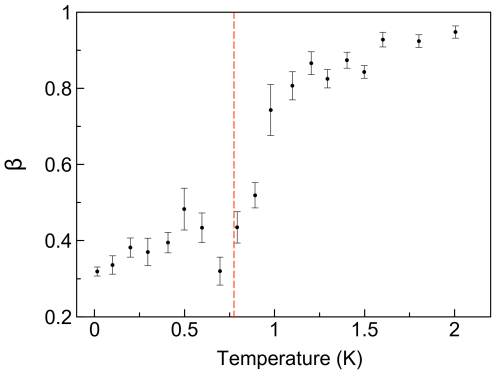

(D) Exponent of the exponential decay in zero field as a function of temperature

FIGURE 3.4: Gd_2ScNbO_7 Zero Field μSR

the static magnetism and better probe the dynamics of the system. As discussed in subsection 2.5.3, static magnetism is much more susceptible to decoupling by a longitudinal field than dynamic magnetism is. The results are shown in Fig. 3.5, displaying a small amount of decoupling. In a longitudinal field, the dynamic and static components of the asymmetry signal no longer need to compose one-third and two-thirds of the signal, respectively, as a decoupling of the static field should occur. Without knowing what the relative components should be and because it describes the data quite well, we used Eq. 3.2 as the fitting function. This function captures a peak in the relaxation at 0.9 K (Fig. 3.5(b)). This peak is also found when other, similar fitting functions are used (not shown). It appears the signal is mostly dominated by dynamic relaxation above 0.2 K in this field, meaning the peak in the relaxation, or alternatively, $1/T_1$, could correspond to critical fluctuations and suggest a transition occurs at 0.9 K in an applied field of 2 T. The asymmetry fits shown in Fig. 3.5(a) also displays a small decoupling below 0.2 K (0.1 K and 0.03 K shown), indicating that a larger fraction of moments are becoming static in the μSR time window.

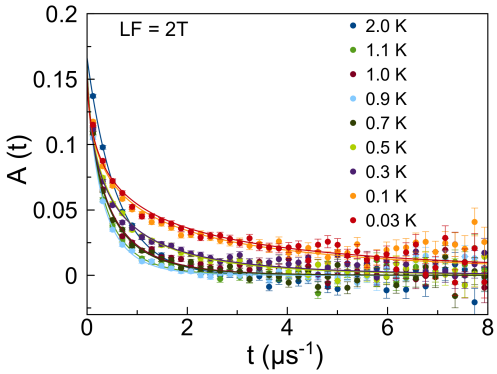

(A) μSR asymmetry measured in a 2 T longitudinal field

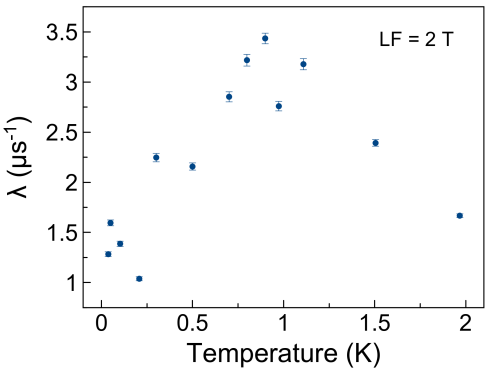

(B) Relaxation rate as a function of temperature in a 2 T longitudinal field.

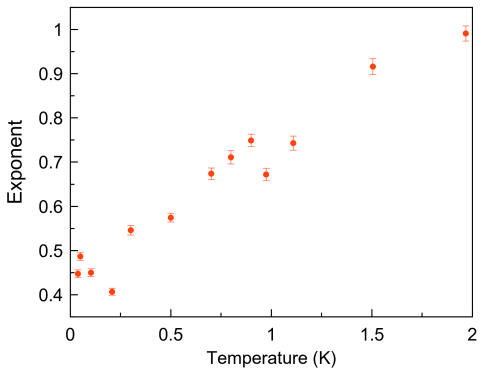

(C) Stretching exponent β as a function of temperature in a 2 T longitudinal field.

FIGURE 3.5: Gd_2ScNbO_7 2 T Temperature Sweep

We performed a zero-field cooled, longitudinal field sweep at 0.1 K and fit the data to a single stretched exponential. The fits demonstrate that the signal has a small amount of decoupling even in a field of 4 T. The relaxation and stretching exponent are shown in Fig. 3.6(a) and Fig. 3.6(b), respectively. A strong reduction in relaxation is observed between the ZF and 1 T data. The change in β as the field increases indicates that the shape of the field distribution the muon detects is changing over this field range.

Our results point to the existence of both static (on the μSR time-scale) and dynamic moments below the transition seen in AC susceptibility. The very fast initial relaxation indicates the development of static moments while the slower relaxation of the 1/3 component points to the existence of dynamic moments. Our 2 T measurements show some decoupling below 0.2 K, indicating an increase in the fraction of moments that are static on the μSR time scale as compared to higher temperatures. Above the transition, the data are well described by a stretched exponential with an exponent that varies from about 1 at high temperature to 0.43 ± 0.04 at 0.8 K.

We have combined these results with neutron scattering and heat capacity results

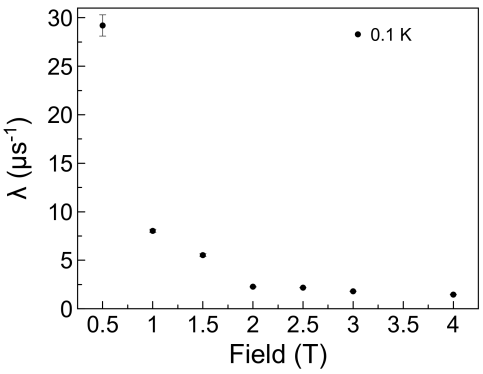

(A) Relaxation rate as a function of longitudinal field at 0.1 K

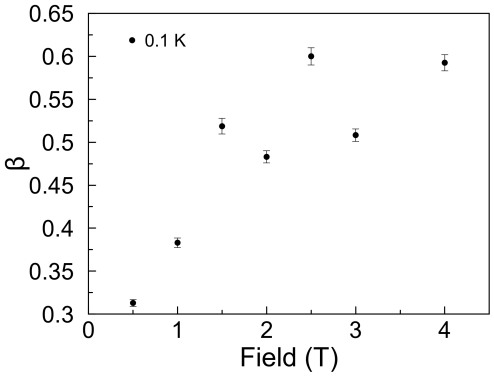

(B) Exponent as a function of longitudinal field at 0.1 K

FIGURE 3.6: Gd_2ScNbO_7 Longitudinal Field Sweep at 0.1 K

from Chris Wiebe's group (University of Winnipeg) into a manuscript to be published [85]. Neutron scattering measurements show nearest neighbour antiferromagnetic, next nearest neighbour ferromagnetic, and third nearest neighbour antiferromagnetic correlations. The magnetic correlation length is 2.1 Å, approximately the nearest neighbour distance. Reverse Monte Carlo simulations of polarized magnetic neutron scattering data using the Γ_7 and Γ_5 magnetic structures suggest the system is XY like, however, Heisenberg interactions fit the data nearly as well [85]. Heat capacity measurements show a broad peak at 1.2 K and integrating over this peak gives an entropy of $\approx 90\% \, R \ln(8)$. The heat capacity at low temperatures is linear.

3.4 Discussion

Our results demonstrate that Gd_2ScNbO_7 is a spin glass system with a transition temperature of T_g= 0.75 K. This is most strongly evidenced by a transition temperature that changes as a function of AC field frequency. The Mydosh parameter of 0.020 ± 0.001 places this system in the spin glass, rather than the super-paramagnetic regime [92]. The ZFC/FC splitting is consistent with this picture while the frustration parameter of $\approx$ 10 shows that frustration plays an important role in this system.

The approximate linear behaviour at low temperature in the heat capacity (measured by Mauws *et. al*) is also consistent with an insulating spin glass. The expected total entropy for this J = 7/2 system is $R \ln(8)$ for which our measured value of $90\% \, R \ln(8)$ is in good agreement. It is possible including contributions below our lowest measured value of 0.4 K could improve the agreement.

The neutron scattering measurements performed by Mauws *et. al* show no long-range order. The elastic magnetic scattering appears similar to the pyrochlore spin-glass $Y_2Mo_2O_7$ except with a magnetic correlation length of 2.1 Å compared to $\approx$ 5 Å for $Y_2Mo_2O_7$ [51]. The alternating antiferromagnetic, ferromagnetic, and antiferromagnetic

correlations between the first, second, and third nearest neighbours, respectively, might be expected to produce spin-glass behaviour in disordered systems like Gd_2ScNbO_7. Here the mixed 3+/5+ cations of the B-site would be expected to distort the local environments compared to a fully 4+ B-site cation. Measurements on Nd_2ScNbO_7 [86] indicate that there are likely a small number of B-site tetrahedra which do not have two Sc^{3+} and two Nb^{5+} (the so called charge-ice state [86]), which introduces additional disorder. The structural disorder in the system produces bond disorder as the distance between first, second, and third nearest neighbours is somewhat variable, producing a range of dipole-dipole interaction strengths. This range in distance, as well as variations in the Gd-O-Gd bond angle, is expected to give a range of superexchange interactions as well, another source of disorder.

Our μSR results are broadly consistent with the expectations of a spin-glass material where static (on the μSR timescale), as well as dynamic magnetism, exist simultaneously. The behavior of our μSR data is qualitatively similar to the dense spin-glass pyrochlore $Y_2Mo_2O_7$ [40, 41] where a very fast relaxing static component is observed, followed by a slower relaxation of the 1/3 tail. Our data indicate that below the transition the system is in the slow fluctuation regime where the relaxation rate, λ_D, is proportional to the fluctuation rate, ν, of the magnetic moments. The exact proportionality depends upon the exponent, β, [32] but given that β is roughly constant below the transition (and the data is well described by Eq. 3.1 when a common exponent is used), we can infer that the dynamics are slowing down, but not completely static, at the lowest temperatures.

Several μSR experiments on spin glasses [21, 74, 41, 33, 123, 129] have empirically found that a stretched exponential describes the asymmetry in the temperature range near, but above the transition. It is found that the stretching exponent is temperature dependent with a value that changes from one at high temperature and approaches 1/3 near the transition temperature, T_g. This represents a change in the fluctuation dynamics where at high temperature, all moments fluctuate at the same rate, while, as the transition is approached, a broad range of fluctuation rates contribute to the relaxation. A Monte Carlo study for 3-dimensional Ising spin glasses [93] found that above the transition, the auto-correlation function, which measures how correlated a spin is with itself at a later time, can be empirically fit by a stretched exponential at long time scales. The stretching exponent in this study varies from 1 at high temperatures and approaches 1/3 at the transition. Our μSR measurements are consistent with this behaviour and suggest Gd_2ScNbO_7 is a spin glass.

Considering this system contains three of the most important ingredients for spin glass systems; disorder, competing interactions, and frustration, it might be expected that Gd_2ScNbO_7 is a spin glass system. It is only after measuring that we can confirm all of our measurement techniques are consistent with spin-glass behaviour providing conclusive evidence that Gd_2ScNbO_7 is a spin glass system. This system is an example of a dense, insulating spin glass which is less well studied than its dilute, metallic counterparts.

3.5 Conclusions

We have synthesized the pyrochlore system Gd_2ScNbO_7 and confirmed phase purity by powder X-ray diffraction. The system contains three key ingredients of spin glass systems; disorder, competing interactions, and frustration. We characterized the magnetic properties of the system using AC and DC magnetisation, heat capacity, neutron scattering, and μSR measurements. All of our measurements are consistent with spin glass behaviour, conclusively demonstrating Gd_2ScNbO_7 is a spin glass system. Gd_2ScNbO_7 offers a pathway for probing the less well studied insulting, dense spin glass systems.

Chapter 4

Nd_2ScNbO_7

4.1 Introduction

Neodymium-based pyrochlores have gained much experimental interest due to exotic physics found in $Nd_2Zr_2O_7$. In general, the Neodymium pyrochlores $Nd_2X_2O_7$ (X = Hf [3, 2, 112], Ir [130], Pb [57], Sn [13]) order partially or fully into an all-in all-out structure around 0.4 K (except for X = Ir which orders at 32 K), however, spin-ice correlations measured above T_N in $Nd_2Zr_2O_7$ may renew interest in studying these systems just above T_N. $Nd_2Zr_2O_7$ displays spin-ice like correlations in combination with all-in all-out order below $T_N \approx 0.4$ K [100], a possible quantum spin-ice phase just above T_N [140], dynamic Kagome-ice correlations in (111) fields [78], and quantum spin-$\frac{1}{2}$ chains in (110) fields [141]. Later measurements on $Nd_2Hf_2O_7$ show similar results [3, 2, 112]. An explanation for these results proposed by Benton [10] is that the magnetic moment fragments in a specific way due to the dipolar-octopolar nature of the CEF ground state. Theoretically, dipolar-octupolar ground states on the pyrochlore lattice garnished interest due to an absence of the debilitating "sign problem" plagued by many condensed matter systems [24]. Huang *et al.* [67] were able to show that the dipolar-octupolar doublet hosts two distinct quantum spin liquid phases; the dipolar and octupolar quantum spin ice phases, increasing interest in these materials. Around the same time, Brooks-Bartlett *et al.* [18] proposed the idea of moment fragmentation where the magnetic moment field fractionalizes into a divergence full part, representing magnetic monopoles, and a divergence-free part, representing a Coulomb phase. With the discovery of simultaneous all-in all-out order and a Coulomb phase in $Nd_2Zr_2O_7$, Benton [10] was able to numerically show how the dipolar-octupolar nature of the CEF ground state leads to moment fragmentation of the transverse moments. For more information on this see sections 1.3.2 and 1.3.3.

The exotic physics discovered in these systems motivates the study of similar Neodymium pyrochlores such as Nd_2ScNbO_7 which has the added complexity of B-site disorder. There are 2^6 possible ways to place Sc^{3+} and Nb^{5+} ions on a pair of tetrahedra, such that the average charge of each ion is 4+. In analogy with the spin-ice state, this particular way of decorating the B-sites is called "charge-ice" ordering. It is an open question as to whether the Sc-Nb systems have (nearly) perfect charge-ice ordering but, naively, charge repulsion should be minimized in this state. Assuming perfect charge-ice ordering, only 0.4% of the Nd^{3+} ions should retain the D3d symmetry of the usual pyrochlore

structure while 17.6% should have D3 symmetry, where there are alternating Sc and Nb ions in a hexagon around the Nd [86, 114] (see Fig. 4.2a). It is only for these particular symmetries that the dipolar-octupolar description of the pseudo-spins is possible and therefore only Nd ions with these symmetries should be able to exhibit moment fragmentation. The likelihood of an Nd ion having these symmetries depends on the distribution of Sc-Nb ions on the B-site, making it important to test the charge-ice hypothesis.

Mauws *et al.* [86] measured the magnetic properties of $Nd_2ScNb_2O_7$ using AC and DC susceptibility, high energy inelastic neutron scattering, polarized neutron diffraction, and low energy time of flight measurements. The pair distribution function of the Sc and Nb ions was probed using both X-rays and neutrons, however, the error bars on both measurements are too large to make any definitive conclusions on the level of charge-ice order. Nonetheless, there is a preference for charge-ice order correlations over a purely random distribution of Sc-Nb ions. AC susceptibility measurements as a function of temperature show no frequency dependence of the transition temperature $T_N = 0.37$ K, precluding any glassy behaviour. DC measurements on a powder sample give a maximum saturated magnetic moment of $2.5 \pm 0.1\ \mu_B$, assuming Ising anisotropy. The theoretical inverse susceptibility, including contributions from the CEF interpretation used in this work, shows deviations from the data in the mid-to-high temperature range where CEF contributions are expected to play a role. In this work, the CEF measurements display four broad peaks on top of a very broad hump (see Fig. 4.1). Mauws *et. al.* interprets three of the peaks as corresponding to CEF levels from Nd ions with D3 symmetry with the broad hump being due to overlap of these crystal field levels as well as contributions from Nd ions which have a different local symmetry. They suggest that the fourth peak is from an imperfectly subtracted phonon. The three peaks, they argue, should come from the most probable CEF environment which they assume is D3. Using the spectral weight of the peaks as compared with the broad hump, they estimate that 14% of the Nd ions have D3 symmetry. When calculating the CEF ground state the broad hump is ignored. Polarized neutron diffraction measurements on a single crystal show the majority of the moment orders into an all-in all-out state as expected for antiferromagnetic interactions on a pyrochlore lattice. An ordered moment of 2.2 ± 0.4 μ_B is measured along with diffuse scattering along the [HHH] and [00L] directions as would be expected from a Coulomb phase. The $(\frac{3}{2},\frac{3}{2},\frac{3}{2})$ peak appears above T_N and reduces in intensity as the temperature is lowered below T_N, as in the parent compound $Nd_2Zr_2O_7$ [140]. A higher resolution measurement was performed which shows a flat, nearly dispersionless, gapped band at 0.07 meV, similar to $Nd_2Zr_2O_7$, however, while the structure factor shows anisotropic scattering between the [HHH], [HH0], and [00L] directions, consistent with a Coulomb phase, the statistics were too poor to confirm the gap structure. Measuring the temperature dependence of this gap would help to determine if it has a similar origin as in $Nd_2Zr_2O_7$. In $Nd_2Zr_2O_7$ and materials with this particular type of moment fragmentation, this gap is expected to decrease and then disappear as the temperature is increased from low temperature to above T_N, where a quantum spin ice phase is entered. Finally, an inelastic moment of $0.26 \pm 0.02\ \mu_B$ was estimated from these measurements. The $2.2 \pm 0.4\ \mu_B$ ordered moment out of a possible

2.5 μ_B is much larger than the 0.8 μ_B out of 2.3 μ_B for $Nd_2Zr_2O_7$ [77] and 0.6 μ_B out of 2.5 μ_B for $Nd_2Hf_2O_7$ [3],

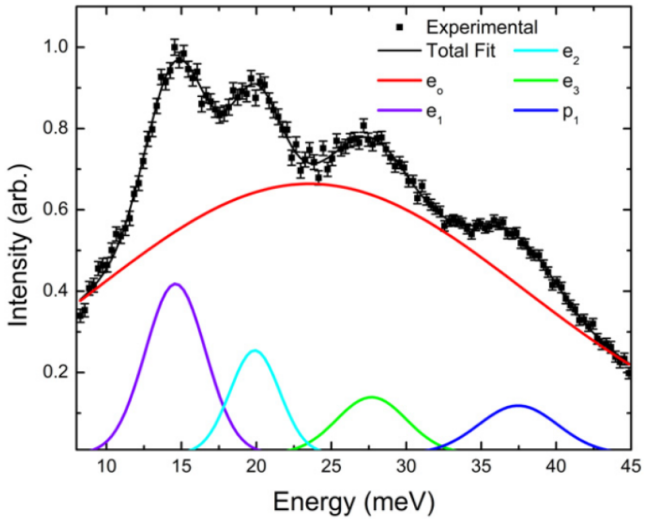

FIGURE 4.1: Inelastic neutron scattering measurement performed by Mauws *et al.* The work interprets the e_i to correspond to crystal electric field levels while p_1 is an improperly subtracted phonon. Reproduced with permissions from [86].

An alternative CEF interpretation is given by Scheie *et al.* [114] where the CEF levels from the 13 possible arrangements of the Sc/Nb ions are simulated and weighted by their relative likelihood assuming that D3 symmetry has a 14% likelihood as assumed in [86]. The point-charge model used does not perfectly reflect the data from [86], however, using a more complex theory may fit the data better. Fig. 4.2a shows that D3 symmetry is not the most likely symmetry while Fig. 4.2b and Fig. 4.2c show the individual CEF levels of the inequivalent symmetries and total CEF scheme, respectively. This simulation suggests that the other allowed symmetries can, and likely do, contribute to the discrete peaks seen by [86].

Scheie *et al.* performed heat capacity, neutron diffraction, and neutron back-scattering experiments on powder samples to probe the electronic moment in different ways, giving complementary information. The heat capacity shows a transition at 370 mK with a nuclear Schottky anomaly developing below 100 mK. Hyper-fine couplings between the Nd nuclei and electrons polarize the nuclear magnetic moments along the direction of the static electronic moments, giving rise to the anomaly. The size of the Schottky anomaly therefore depends on the local static electronic moment. The peak of the Schottky anomaly is not observed, however, the high-temperature tail of the Schottky anomaly gives a measure of the root-mean-square (RMS) electronic local static moment [114]. The electronic heat capacity can not be accounted for with a simple T^3 relationship expected for linearly dispersing spin-waves. The best agreements come from three different models which gives an average RMS electronic magnetic moment of 1.17(3) μ_B

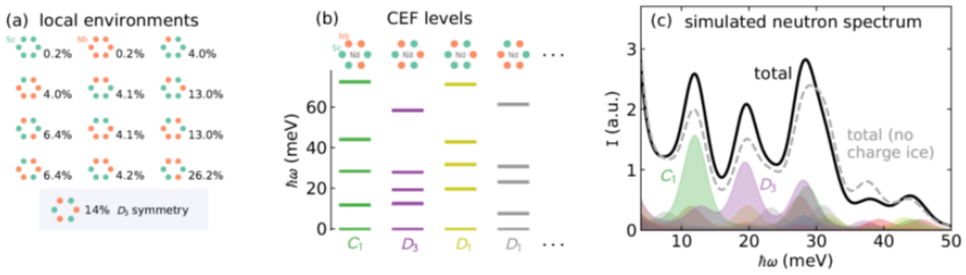

FIGURE 4.2: (a) The 13 symmetry inequivalent arrangements of the Sc/Nb ions surrounding an Nd ion. (b) The crystal electric field levels of the arrangements and (c) the weighted sum. Reproduced with permissions from [114].

(for more information on the models see Ref. [114]). A neutron diffraction measurement on a triple-axis spectrometer measures the mean magnetic moment participating in long-range order to be 1.121 (9) μ_B. Finally, the neutron back-scattering experiment probes the magnetic field probability distribution through the hyper-fine splitting of the degenerate nuclear spin levels. The degree of splitting depends upon the size of the local moment, allowing the local field probability distribution to be probed. The intensity is well described by a model which includes a Gaussian and Lorentzian function (representing static and dynamic moments, respectively) convoluted with the Boltzmann factor as well as the resolution function (c.f. appendix A2 of Ref. [114]). The shape of the field distribution changes from Lorentzian to Gaussian as the temperature is lowered through the transition, accompanied by an increase in the static moment size. The mean local moment from this measurement is estimated to be 1.47 (6) μ_B, 1.32 (5) times larger than the ordered moment. This rules out classical moment fragmentation (the monopole crystal model) discussed in Ref. [18], Ref. [99], and section 1.3.3, because for this state the local moment should be twice the ordered moment. Interestingly, inelastic neutron scattering indicates a flat, dispersionless band around 0.1 meV (energy resolution of 0.08 meV) very similar to Ref. [86] which could correspond to the Coulomb phase proposed by Benton [10].

To reconcile the differences between the magnetic moment measured by the three different methods, [114] proposes a phenomenological model where $\frac{1}{4}$ of the moments remain dynamic, or, are static with very small moments, to very low temperatures. They show that this model can reproduce their heat capacity and neutron back-scattering measurements quite accurately, however, the theoretical models they propose to produce this may not be appropriate to the material. The proposed theories include a model describing spin-$\frac{1}{2}$ spin-liquids on a triangular lattice [144], gapless Z_2 quantum spin-liquids in combination with all-in all-out order on the pyrochlore lattice [79], a moment modulated spin fragmented state which applies to non-Kramers ions on the Kagome lattice [37], disorder-induced states in non-Kramers ions on the pyrochlore lattice [113], singlet formation through bond disorder in Heisenberg antiferromagnets on

the pyrochlore lattice [132], and a partial spin-glass state due to bond-disorder. While the resulting effects of many of these theories could describe Nd_2ScNbO_7, it is unclear how these effects would come about with an easy-axis, Kramers ion on the pyrochlore lattice that appears to have a 0.1 meV gap and no indication of glassiness in AC susceptibility. On the other hand, the model proposed by Benton [10] naturally includes both static and fluctuating moments through the particular moment fragmentation possible in Dipole-Octupole magnets on the pyrochlore lattice, which is not considered in Ref. [114].

In this study, we use μSR to examine the moment fragmentation candidate $Nd_2ScNb_2O_7$. We grow a single crystal of the material and characterize it using powder X-ray diffraction and magnetic susceptibility measurements. We perform ZF and LF μSR measurements to unambiguously confirm or exclude coexisting static and dynamic magnetism.

4.2 Methods

We have grown large single crystals of Nd_2ScNbO_7 using the optical floating zone technique. We prepared polycrystalline rods of Nd_2ScNbO_7 using stoichiometric ratios of Sc_2O_3 (99.999%), and Nb_2O_5 (99.99%). We annealed the polycrystalline rods in argon at 1200°C for 48 hours. We grew a large single crystal from these rods with a growth speed of 15 mm/hr in 4 atm of O_2. The phase purity of (crushed) crystal was confirmed with powder X-ray diffraction.

We performed DC susceptibility measurements using a Quantum Design MPMS 5 Superconducting Quantum Interference Device (SQUID), providing a base temperature of 1.8 K. A He3 insert was placed inside the system to allow for measurements down to 0.5 K. Our DC measurements were performed on a single crystal cut into a disc with a mass of 57.82 mg. DC susceptibility was measured in a field of 100 Oe.

We performed Zero field (ZF) and longitudinal field (LF) μSR measurements on the M15 and M20 beamlines at the TRIUMF Laboratory in Vancouver, Canada. On the M15 beam line, we used a spectrometer incorporating a dilution refrigerator which allowed for measurements in the temperature range of 0.025-10K. The experimental set-up makes use of a superconducting magnet to allow for fields up to 5 T. We mounted the samples on a silver cold finger using copper grease mixed with N grease to ensure adequate heat transfer between the sample and cold finger. Silver gives a well-defined μSR background signal with very little relaxation. The instrument has a time resolution of 0.4 ns. On the M20 beamline, we used the low background apparatus LAMPF with temperature capabilities from 1.9-300 K and fields up to 4 kG. This instrument also has a resolution of 0.4 ns. We explored the effect of applied fields anti-parallel to the direction of the initial muon spin polarization (LF). We cut several 2 mm thick plates of Nd_2ScNbO_7 from a single crystal such that the normal of the face of each plate lies along the (111) direction. This geometry means the initial muon polarization and any applied fields were along the (111) direction. We used the muSRfit software platform [125] to analyse the collected μSR spectra.

4.3 Results

4.3.1 Characterization

We grew an approximately 10 cm long crystal of Nd_2ScNbO_7 (Fig. 4.3(a)) using the optical floating zone technique. A large facet can be seen running along the side of approximately 7 cm of the crystal in Fig. 4.3(b).

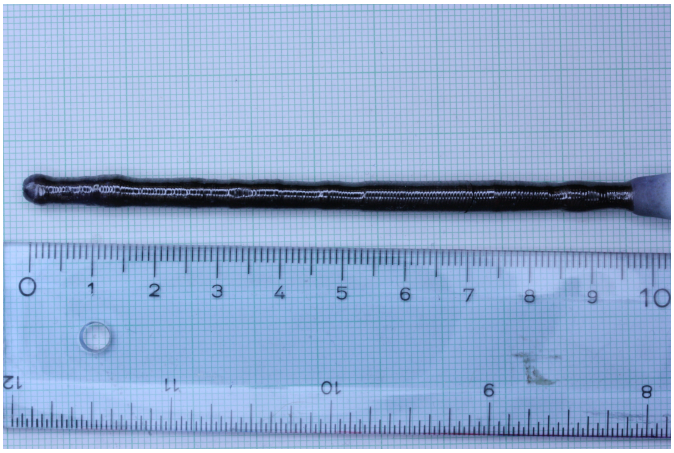

(A) As grown Nd_2ScNbO_7 crystal produced using the optical floating zone method.

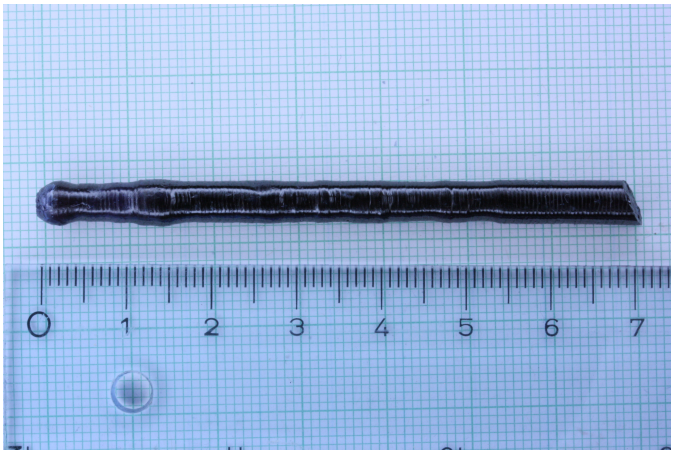

(B) A flat facet runs across approximately 7 cm of the Nd_2ScNbO_7 crystal.

FIGURE 4.3: Nd_2ScNbO_7 crystal produced using the optical floating zone method.

We performed powder X-ray diffraction (PXRD) on a fragment of our crystal after grinding the fragment into a fine powder. PXRD results are shown in Fig. 4.4(a) with a Reitveld refinement to a pyrochlore phase. There is no evidence of phase impurity. Fig 4.4(b) shows the Laue diffraction pattern along the (111) direction of a section of our

as grown crystal. The crystal was translated along its length and width with no change to the Laue diffraction pattern, indicating that the sample is single crystal on a surface level. The crystal was then rotated 180 degrees and the same procedure was performed, with no change in the Laue diffraction pattern. The crystal was aligned and cuts were made perpendicular to the (111) direction. After cutting, we checked 3 pieces with Laue diffraction, one from the middle of the crystal and two from either end of the crystal, to confirm both the single crystal nature of the sample, and that alignment was maintained during cutting. Overall these results indicate a phase pure single crystal sample aligned along the (111) direction.

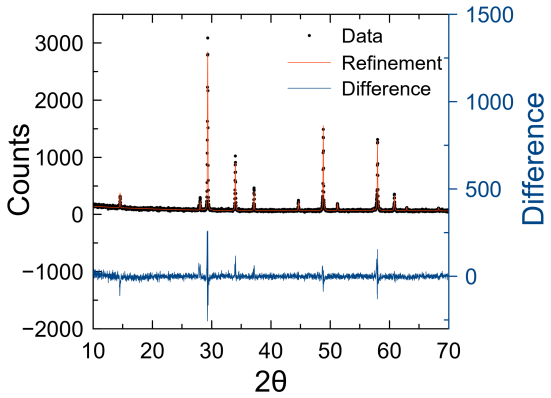

(A) Nd_2ScNbO_7 room temperature powder X-ray diffraction with Reitveld refinement to a pyrochlore phase.

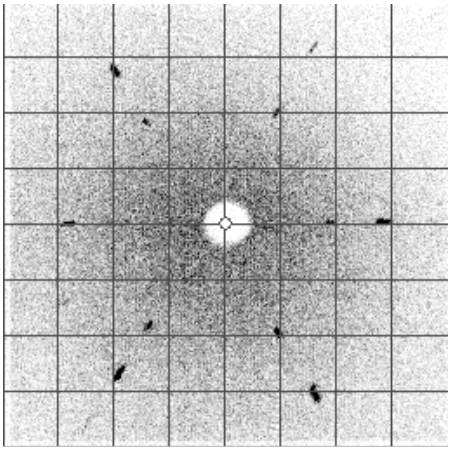

(B) Nd_2ScNbO_7 crystal (111) Laue diffraction pattern.

FIGURE 4.4: Nd_2ScNbO_7 structural characterization

We performed X-ray Laue diffraction on our 7 cm long crystal, scanning along the length of both sides of the crystal, and found no indication of multiple grains. To confirm this we performed a neutron pole figure measurement at the McMaster Nuclear Reactor, indicating approximately 90% is a single grain by comparing the heights of peaks from the primary and secondary grains. Using the Laue diffraction method, the crystal was aligned along the (111) axis of the dominant grain (there was no evidence of a second grain in Laue measurements) and the crystal was cut into plates with faces perpendicular to a global (111) axis.

4.3.2 SQUID Magnetometry

We performed SQUID magnetometry measurements on a 57.82 mg disc of single-crystal Nd_2ScNbO_7. Low-temperature results are displayed in Fig 4.5(a) which show no magnetic transition or zero field cooled/field cooled splitting above 0.5 K; consistent with previous heat capacity and neutron scattering results which show a transition at ≈0.375 K [86, 114]. The high-temperature molar susceptibility (Fig. 4.5(b)) is fit to a modified Curie-Weiss law at high temperature (50-300 K) where a temperature independent term is included. This temperature-independent term partially accounts for the Van-Vleck

susceptibility due to the crystal electric field levels which are not precisely known in this compound [86, 114]. This fit results in an effective magnetic moment of 3.45 μ_B; in good agreement with the expected value of 3.5-3.6 μ_B. Low-temperature fits (10-30 K) result in an effective moment of 2.64 $\pm$ 0.05 μ_B, in relative agreement with the expectations of [86] and [114], with a Curie-Weiss temperature of -0.4 $\pm$ 0.3 K indicating antiferromagnetic interactions.

4.3.3 μSR

We performed zero-field and longitudinal field μSR measurements on 2 mm thick plates of single-crystal Nd_2ScNbO_7 with the initial muon polarization along the (111) direction. Fig. 4.6(a) shows the Asymmetry data fit to a Dynamic Gaussian Broadened Gaussian Kubo-Toyabe (GBG). Fig. 4.6(b) shows the early time behaviour of the Asymmetry which displays a Gaussian relaxation. This early time behaviour is seen at and below the transition temperature of $\approx$0.4 K measured by other techniques [86, 114], indicating the presence of static or slow dynamic magnetism. Higher temperature measurements have an exponential early time behavior consistent with the faster dynamics of a paramagnetic phase.

The GBG provides a smooth distribution of Δ (Fig. 4.7(a)), the full-width half-maximum of the field distribution, that increases as the transition seen in other measurements is approached from above and roughly flattens out below this transition. This function assumes that the full-width half-maximum has a value that is randomly selected from a Gaussian probability distribution, with width, Δ_{GBG}, and mean value Δ. A parameter used in this function is the ratio, R, of the full-width half-maximum of the Gaussian distribution, Δ_{GBG}, to the mean Δ, which fits a global value of 0.31 $\pm$ 0.02. For comparison, the Dynamic Gaussian Kubo-Toyabe has R = 0. The fluctuation rate when fitting to the GBG is shown in Fig. 4.7(b) displaying a minimum slightly above the transition temperature. Δ is shown in Fig. 4.7(a) where it can be seen that Δ increases as the temperature decreases until 0.25 K, where there is a maximum, followed by a decrease.

The low temperature, low field LF data (measured in 2018) is shown in Fig. 4.8(a) with the higher field data displayed in 4.8(b). For the low temperature fits the initial asymmetry and α calibration are fixed to the ZF values as these should be valid up to 5 kG, and a decoupling fraction parameter is included. The fraction of the signal decoupled is about 10% for all fields from 50 G to 5 kG. In high field data (measured in 2019) it can be seen that the relaxation is increasing from 0.5 T to 2.5 T. The data are fit with a Dynamic Gaussian Kubo-Toyabe with the field fixed to be the applied field. There is additional relaxation observed at long times in the high field data which the fit does not capture. The results of the fits are shown in Fig. 4.9 with the relaxation rate in Fig. 4.9(a) and the fluctuation rate in Fig. 4.9(b). The fits show a peak in both the relaxation and fluctuation rate at 2.5 T, likely indicating a field-induced transition, discussed below. We also performed LF measurements in the paramagnetic state with low field measurements performed on the M20 beamline and high field measurements on

the M15 beamline. Data are fit to a simple exponential function and the relaxation rate is shown in Fig. 4.9(c) where a maximum in the relaxation rate can be seen around 2 T. While the data from M20 and M15 may not be directly comparable, they show the trend of the relaxation rate in their respective field ranges.

4.4 Discussion

Our ZF μSR measurements of Nd_2ScNbO_7 are qualitatively similar to the ZF μSR measurements of $Nd_2Zr_2O_7$ [138]; both are well described by the Gaussian Broadened Gaussian Kubo-Toyabe function with a similar magnitude and temperature dependency of the parameters. There are small differences in Δ in that our measurements show a slight decrease below about 0.25 K where the measurements of $Nd_2Zr_2O_7$ are flat, however, our error bars are non-negligible and the behaviour could be random scatter around a constant Δ below 0.4 K. Similarly, our measured fluctuation rate below 0.4 K may be constant, with fluctuations around a mean value. The disordered B-site in Nd_2ScNbO_7 does not appear to drastically alter μSR measurements as compared to $Nd_2Zr_2O_7$, which is surprising given the effect the B-site disorder has on neutron scattering measurements.

Both our μSR measurements and the measurements on $Nd_2Zr_2O_7$ show persistent spin dynamics, however, differences are seen between our LF measurements. Both sets of data are fit with the Dynamic Gaussian Kybo-Toyabe function. In the LF measurements along the (111) axis of $Nd_2Zr_2O_7$ at 20 mK, a peak in the fluctuation rate is seen near 0.1 T in the fluctuation rate, which we do not see in our data. A peak is observed in both the imaginary component of the AC susceptibility [77] as well as in the derivative of the DC magnetisation [78] at this field in this material. Neutron scattering measurements also show a change in the inelastic scattering pattern to a possible dynamic Kagome ice state [78] or reorientation of all-in all-out domains to all-out all-in domains [139]. In the dynamic Kagome spin ice, the pyrochlore lattice is described as alternating layers of triangular and Kagome lattices where all of the moments on the triangular lattice point in the field direction while moments in the Kagome lattice follow a two-in one-out/one-in two-out pattern. In the reorientation case (Fig. 4.10), considering two tetrahedra together, an all-in all-out state could have 6 moments in the Kagome layers with a component opposite to the applied field while the moment in the triangular layer points in the direction of the (111) field. The energy may be lowered by flipping the 6 spins to have a component along the applied field while the moment in the triangular layer is flipped to point opposite to the field. Eventually, as the field gets large enough it polarizes all of the moments into a three-out one-in/one-in three-out state as shown in Fig. 4.10. Our measurements could have a similar explanation for our observed peak in the relaxation rate, albeit at much higher fields due to the larger static ordered moment while the very large width of the transition could be from the disordered B-site affecting both the moment size, as well as the muon stopping sites. If we use the ordered moment of 1.3 μ_B a field of 0.5 T causes a Zeeman splitting comparable in size to the interaction strength (based on the transition temperature of the material). As this is the field where

the relaxation rate starts to increase in our material, moment reorientation followed by polarization may be a more favourable explanation for Nd_2ScNbO_7 than the Kagome ice state. It may also be likely that the Kagome ice state is sensitive to disorder, again making spin reorientation a more favourable explanation for our data.

In all, our μSR results on Nd_2ScNbO_7 are quite similar to the moment fragmentation candidate $Nd_2Zr_2O_7$. The μSR technique can observe both static and dynamic magnetism in combination, which our measurements are consistent with and is the expected signal of moment fragmentation. The neutron scattering measurements of [84] and [114] also contain many of the same features as those seen in $Nd_2Zr_2O_7$. For these reasons, we consider Nd_2ScNbO_7 a plausible candidate for moment fragmentation physics. Possible future measurements could include additional neutron scattering measurements on a large single crystal to confirm the Coulomb phase correlations expected in the 0.1 meV band as discussed in sections 1.3.2 and 1.3.3.

4.5 Conclusions

We have performed the crystal growth and characterization of the pyrochlore material Nd_2ScNbO_7. Our measurements show our samples are phase pure with similar susceptibility to samples grown by other groups. Our μSR measurements show a striking similarity to the measurements performed on the moment fragmentation candidate $Nd_2Zr_2O_7$ [138]. This, in combination with neutron scattering measurements performed by other groups ([84, 114]) provide evidence for a moment fragmentation state in this mixed B-site pyrochlore where disorder is expected to affect the crystal electric field levels.

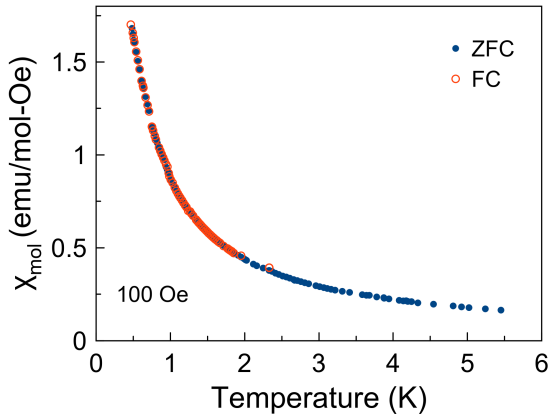

(A) Low-temperature magnetic susceptibility of Nd_2ScNbO_7 measured in a 100 Oe field when zero-field cooled (blue) and field cooled (red)

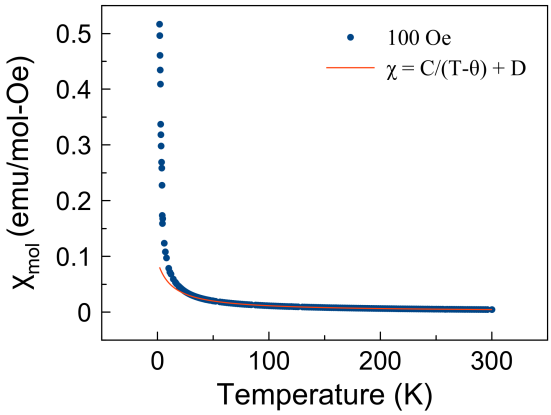

(B) High-temperature magnetic susceptibility of Nd_2ScNbO_7 measured in a 100 Oe field

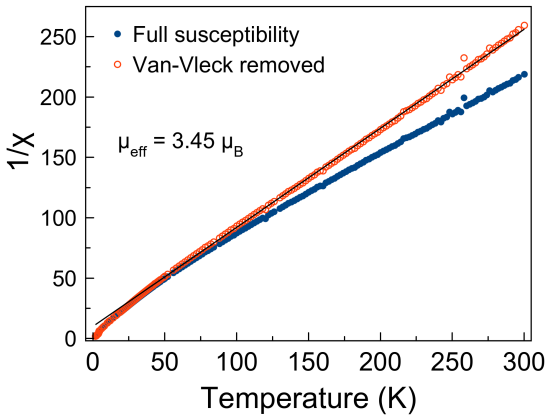

(C) Inverse magnetic susceptibility of Nd_2ScNbO_7 measured in a 100 Oe field

FIGURE 4.5: Magnetic Susceptibility of Nd_2ScNbO_7.

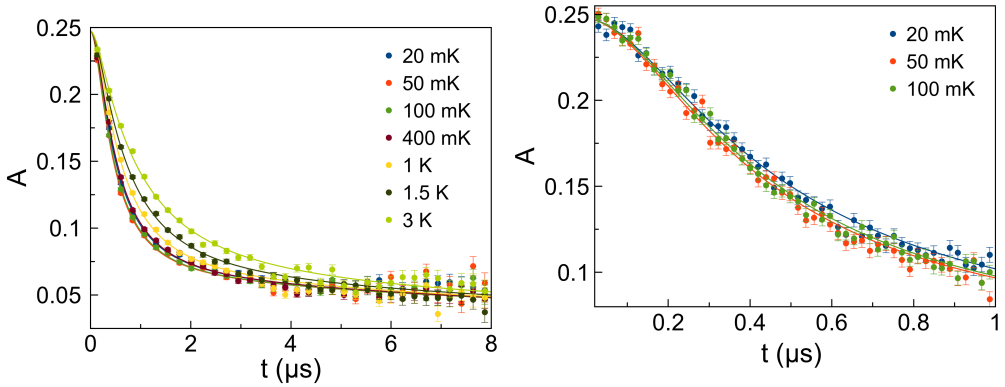

(A) Zero-field Asymmetry of Nd_2ScNbO_7 fit to the Dynamic Gaussian Broadened Gaussian function.

(B) Early time Zero-field Asymmetry of Nd_2ScNbO_7 fit to the Dynamic Gaussian Broadened Gaussian function. The early time behaviour appears Gaussian.

FIGURE 4.6: Zero-field Asymmetry of Nd_2ScNbO_7.

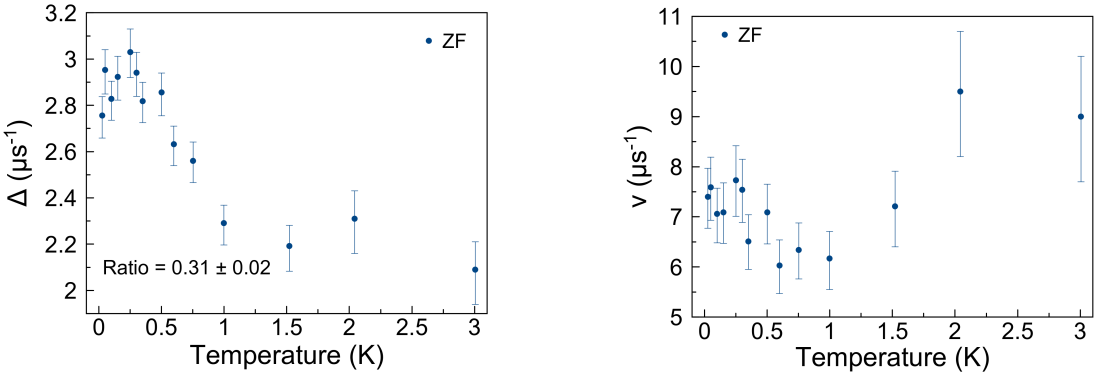

(A) Zero-field Δ of Nd_2ScNbO_7 when fit to the Dynamic Gaussian Broadened Gaussian function.

(B) Zero-field fluctuation rate of Nd_2ScNbO_7 when fit to Dynamic Gaussian Broadened Gaussian function.

FIGURE 4.7: Results of fitting the zero-field Nd_2ScNbO_7 Asymmetry to the Dynamic Gaussian Broadened Gaussian function.

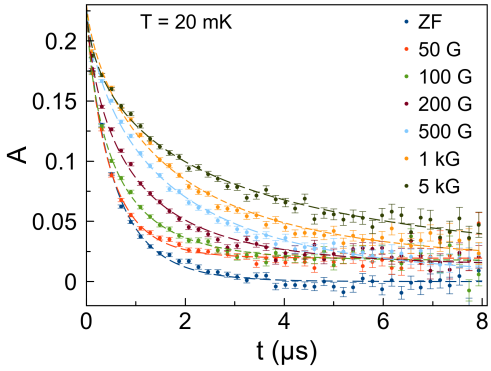

(A) Low-temperature, low field LF Asymmetry distribution of Nd_2ScNbO_7 fit to the Dynamic Gaussian Kubo-Toyabe function.

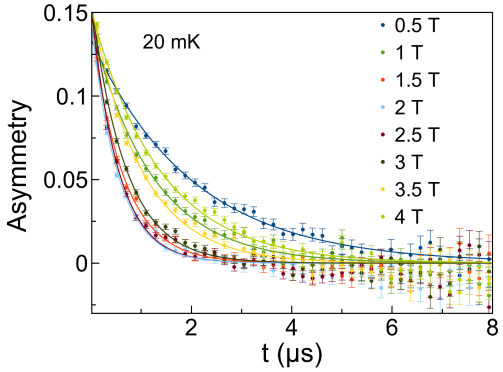

(B) Low-temperature, high field LF relaxation rate of Nd_2ScNbO_7 fit to the Dynamic Gaussian Kubo-Toyabe function.

Figure 4.8: Longitudinal field Nd_2ScNbO_7 Asymmetry Results fit to a Dynamic Gaussian Kubo-Toyabe.

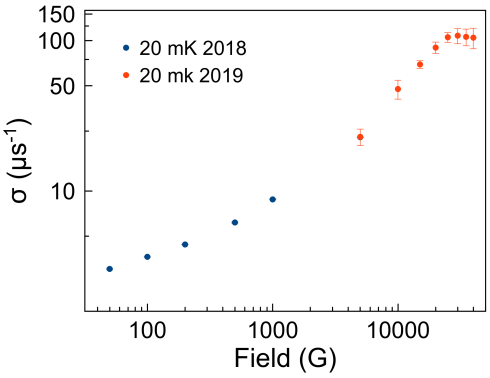

(A) Low-temperature longitudinal field relaxation rate of Nd_2ScNbO_7 when fit to the Dynamic Gaussian Kubo-Toyabe function.

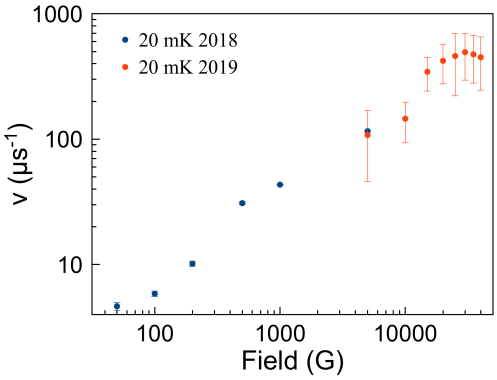

(B) Low-temperature longitudinal fluctuation rate of Nd_2ScNbO_7 when fit to the Dynamic Gaussian Kubo-Toyabe function.

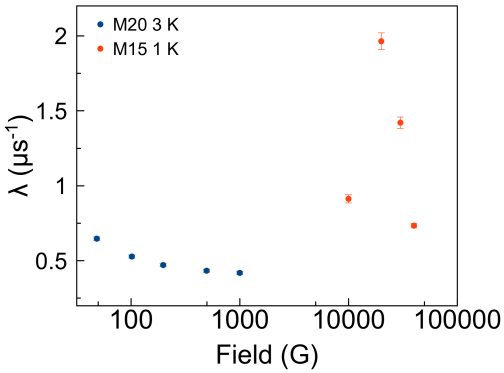

(C) High-temperature longitudinal field relaxation rate of Nd_2ScNbO_7 when fit to a simple exponential.

FIGURE 4.9: Longitudinal field Nd_2ScNbO_7 Asymmetry Results.

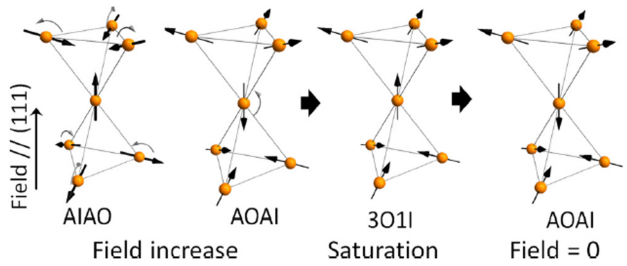

FIGURE 4.10: All-in All-out spin reorientation as the applied field is increased and then decreased in the last panel. Reused from [139] with permissions.

Chapter 5

$Sm_2Ti_2O_7$

5.1 Introduction

Perhaps the earliest interest in Samarium based pyrochlores was $Sm_2Sn_2O_7$ as a thermometer in NMR measurements using the paramagnetic chemical shift of Sn^{119} [55], while more recent studies have focused on $Sm_2Zr_2O_7$ and $Sm_2Hf_2O_7$ as a high-temperature thermal barrier coating due to these material's low thermal conductivity [90, 143, 124]. In this thesis, we examine the low-temperature magnetic properties of $Sm_2Ti_2O_7$ which gained interest after the discovery of a classical spin-ice phase in $Dy_2Ti_2O_7$ [103] and $Ho_2Ti_2O_7$ [61]. A significant difference between these materials and $Sm_2Ti_2O_7$ is the moment size of $\approx$10 μ_B for Dy/Ho while Sm in this material has a moment less than 0.5 μ_B. This means that the dipolar interactions, which are so important for $Dy_2Ti_2O_7$ and $Ho_2Ti_2O_7$, are over 100 times weaker in $Sm_2Ti_2O_7$.

It may come as no surprise then that neutron scattering measurements show $Sm_2Ti_2O_7$ [84] and $Sm_2Sn_2O_7$ [98] order antiferromagnetically into an all-in all-out ground state, as one would expect by considering the nearest neighbour Dipolar Spin-ice model discussed in section 1.3.1. The transitions seen in neutron scattering are accompanied by sharp λ anomalies in specific heat measurements at T_N = 0.35 K and 0.44 K for $Sm_2Ti_2O_7$ [84, 98] and $Sm_2Sn_2O_7$ [98], respectively, supporting a transition to long-range order. In contrast to this, $Sm_2Zr_2O_7$ displays a broad peak in heat capacity around 0.6 K [142] that is as of yet unexplained. We could find no reports of neutron scattering measurements on this material, possibly due to the need for isotopically enriched Sm^{154} samples for this measurement. Natural Sm contains around 14% Sm^{149} which is a very strong neutron absorber (σ = 42000 b) that will dominate the signal even in small amounts [84, 98]. All three materials have a crystal electric field (CEF) ground state doublet formed from states with $m_j = \frac{3}{2}$ or $\frac{9}{2}$, giving them dipolar-octupolar character [84, 81, 98]. Benton [11] showed that the phase diagram for materials with Dipolar-Octupolar doublets contains the all-in all-out ordered state, Octupolar ordered state, and four Quantum Spin Liquid states which are determined by how the emergent electric field transforms (Dipolar or Octupolar) as well as if there are 0 or π units of flux penetrating plaquettes in the ground state, as discussed in sections 1.3.2 and 1.3.3. By examining excitations around the all-in all-out ordered state it can be determined if the material is a candidate for moment fragmentation as in $Nd_2Zr_2O_7$ [100] and $Nd_2Hf_2O_7$ [2].

There is no consensus on the form of the ground state doublet of $Sm_2Ti_2O_7$, other than it only contains states with $m_j = \frac{3}{2}$ or $\frac{9}{2}$. Malkin *et. al.* [81] estimated the g-tensor of this material using susceptibility data, where a very broad hump is seen in the susceptibility centered around approximately 140 K. In this material the parallel component of the g-tensor, $g_{||}$ of the ground state (which has purely Ising character) is much smaller than either component of the g-tensor for the two excited states, meaning exciting these states have a large effect on the susceptibility.

Inelastic neutron scattering measurements by Mauws *et. al.* [84] on an approximately 3 gram, 99.8% Sm^{154} isotopically enriched single crystal show CEF excitations at 16.5 meV and 70 meV along with two phonon mode excitations also measured in Raman scattering [117]. Particular care was taken to correct for the absorption cross-section of Sm^{149} as this cross-section has a maximum in the 50-100 meV range. After this correction, the two CEF levels are shown to follow the magnetic form factor of the lowest Sm^{3+} J-multiplet, J = 5/2. This analysis uniquely points to a pure $m_j = \pm 3/2$ ground state with a calculated ordered moment of 0.43 μ_B.

Inelastic neutron scattering measurements in several energies up to 300 meV were performed by Pecanha-Antonio *et. al.* [98] on 0.7 grams of 98.5% Sm^{154} isotopically enriched powder. They observe excitations at 16 meV and 70 meV, however, they show that the 70 meV excitation does not follow the magnetic form factor for the J = 5/2 ground state multiplet. This is possibly due to the increased Sm^{149} content in their sample as compared to Mauws *et. al.* which they do not appear to correct for. They do not use the 70 meV excitation in their analysis but include several higher measured excitation levels along with transitions to the excited J = 7/2 and J = 9/2 states. From this analysis, they find all states included in the CEF ground state have $m_j = \pm 3/2$ or $\pm$ 9/2, however, there are contributions from the J = 7/2 and 9/2 multiplets. They estimate an ordered moment of 0.16 μ_B for this ground state. In their work, they also measure magnetic susceptibility on a powder sample which fitting to a Curie-Weiss model from 5-30 K produces a magnetic moment of 0.22(3) μ_B. For an Ising material the powder susceptibility is expected to produce a moment of half the ordered moment and therefore this measurement is in agreement with the 0.43 μ_B calculated by Mauws.

Polarized neutron scattering measurements by Mauws *et. al.* [84] show no indication of magnetic diffuse scattering and uniquely points to an all-in all-out ground state while a triple-axis spectrometer measures an ordered moment of 0.44(7) μ_B, in agreement with their calculations as well as the susceptibility data of [98]. [98] are unable to measure any magnetic peaks, possibly because the sample did not cool enough.

Finally, we turn to the zero-field (ZF) μSR data of Mauws *et. al.* [84]. Their ZF data are well described by a Gaussian relaxation below 1 K which shows an increase in the relaxation rate at the transition temperature. A temperature-independent background component is subtracted off of the displayed data, resulting in a relaxation rate of zero above 1 K for the material. This situation is unusual and may represent an over-subtraction of the data. It is argued the system shows persistent spin dynamics as the asymmetry does not show any oscillations; a clear sign of static magnetic order. This

however does not guarantee there is no static magnetic order as a spread in the field probability distribution would cause the asymmetry to have Kubo-Toyabe behaviour and given the small moment of the system, this may be difficult to differentiate from a simple Gaussian or exponential relaxation. Further, they do not present longitudinal field (LF) measurements which would indisputably differentiate between static and dynamic magnetism.

We seek to unambiguously determine if there is static or dynamic magnetism through LF μSR measurements of this system. We will perform zero-field measurements on a new sample of $Sm_2Ti_2O_7$ while also exploring signatures of magnetic ordering in transverse field measurements, similar to what was seen in $Yb_2Ti_2O_7$ [34].

5.2 Methods

We have grown large single crystals of $Sm_2Ti_2O_7$ using the optical floating zone technique. We prepared polycrystalline rods of $Sm_2Ti_2O_7$ using stoichiometric ratios of Sm_2O_3 (99.99%), and TiO_2 (99.99%), mixing the powders thoroughly using an agate mortar and pestle. We annealed the polycrystalline rods in Oxygen at 1350°C for 48 hours. We grew a large single crystal from these rods with a growth speed of 4 mm/hr in 5 atm of O_2. The phase purity of (crushed) crystal was confirmed with powder X-ray diffraction.

We performed zero-field (ZF), high transverse field (TF), and longitudinal field (LF) μSR measurements on the M15 beamline at the TRIUMF Laboratory in Vancouver, Canada. We used a spectrometer incorporating a dilution refrigerator which allowed for measurements in the temperature range of 0.025-10K. The experimental set-up makes use of a superconducting magnet to allow for fields up to 5 T. We cut several 2 mm thick disks of $Sm_2Ti_2O_7$ from a single crystal such that the normal to the face of each disk lies along the (110) direction. This geometry means the initial muon polarization and any applied fields were along the (110) direction. We mounted the disks on a silver cold finger using copper grease mixed with N grease to ensure adequate heat transfer between the sample and cold finger. Silver gives a well-defined μSR background signal with very little relaxation. The instrument has a time resolution of 0.4 ns. We used the muSRfit software platform [125] to analyse the collected μSR spectra.

5.3 Results

5.3.1 Structural Characterization

We performed a powder X-ray diffraction measurement on finely ground crystal from a section of our growth. Fig. 5.1(a) shows the results of our measurement with Reitveld refinement to a pyrochlore phase. There are no indications of any phase impurities. Fig 5.1(b) shows the Laue diffraction pattern along the (001) direction of a section of our as grown crystal. The crystal was translated along its length and width with no change to the Laue diffraction pattern, indicating that the sample is single crystal on a surface

level. The crystal was then rotated 180 degrees and the same procedure was performed, with no change in the Laue diffraction pattern. The crystal was aligned and cuts were made perpendicular to the (110) direction. After cutting, we checked 3 pieces with Laue diffraction, one from the middle of the crystal and two from either end of the crystal, to confirm both the single crystal nature of the sample, and that alignment was maintained during cutting. Overall these results indicate a phase pure single crystal sample aligned along the (110) direction.

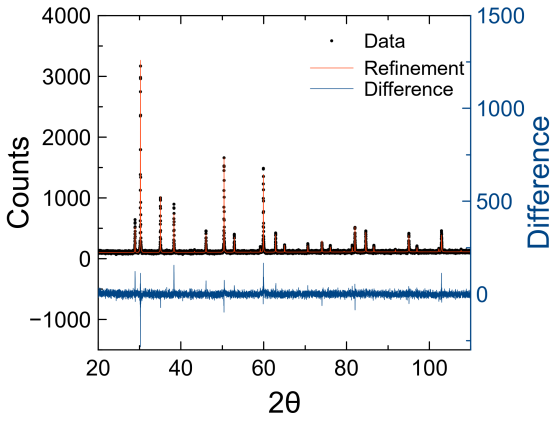

(A) $Sm_2Ti_2O_7$ room temperature powder X-ray diffraction with Reitveld refinement to a pyrochlore phase.

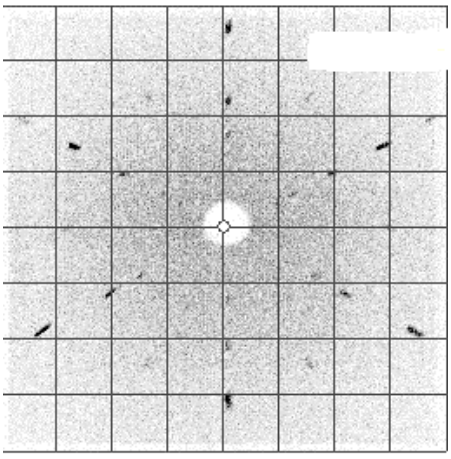

(B) $Sm_2Ti_2O_7$ crystal (001) Laue diffraction pattern.

FIGURE 5.1: $Sm_2Ti_2O_7$ structural characterization.

5.3.2 μSR

Fig. 5.2 shows our $Sm_2Ti_2O_7$ zero-field (ZF) μSR measurement results fit to a phenomenological model,

$$A(t) = A_0 \left[F_S \, \mathrm{GKT}(\sigma t) \exp(-\lambda t) + (1 - F_S) \exp(-\lambda_{Bkg} t) \right], \tag{5.1}$$

where F_S is the fraction of the signal coming from the sample, $\mathrm{GKT}(\sigma t)$ is the static Gaussian Kubo-Toyabe given by Eq. 2.21 with relaxation rate σ, λ is the Lorentzian relaxation rate of the sample and λ_{Bkg} is the relaxation rate of the background. In this equation, σ is roughly the relaxation rate due to static moments while λ is roughly the relaxation rate due to dynamic moments. It should be noted that even the low-temperature data required the inclusion of the Lorentzian relaxation to produce a high-quality fit. Fig. 5.2(a) shows the ZF Asymmetry data is very well described by Eq. 5.1. The static relaxation rate in Fig. 5.2(b) begins to increase at 0.8 K, where magnetic correlations might be expected to develop. An increase in relaxation occurs at 0.4 K, approximately the transition temperature seen in [84] and [98], with an overall trend of increasing as the temperature is lowered. The Lorentzian relaxation in Fig. 5.2(c)

displays a peak at 0.7 K and decreases below this temperature. We interpret this as the dynamic fluctuation rate is decreasing with more explanation given in the discussion.

Fig. 5.3(a) shows our low-temperature $Sm_2Ti_2O_7$ high transverse field (TF) Asymmetry data in a rotating reference frame of 1.006 T while 5.3(b) shows the Fourier transform of this data. Displaying the data in a rotating reference frame shows the difference between the data and a signal precessing at the rotating reference frame frequency, allowing for a better visualization of the data. The high-temperature data is shown in Fig. 5.4. The data is fit to two oscillating components with an exponential decay for the sample, along with another oscillating and much more slowly decaying exponential. The fits to the data are quite good and we can measure the field drift in the magnet over time quite accurately.

The results of our fits are shown in Fig. 5.5, where it is seen that the frequency shift of one component of the signal is about 10 times the frequency shift of another, but has approximately the same magnitude of relaxation. The large frequency shift component has a frequency shift (Fig. 5.5(a)) which increases in magnitude as the temperature decreases until 0.5 K where the frequency shift levels off. The frequency shift of the smaller frequency shift component (Fig. 5.5(b) has a large amount of scatter above 0.6 K but below this temperature, the magnitude of the shift decreases with decreasing temperature. The relaxation rate of the large frequency shift component (Fig. 5.5(c) increases until approximately 0.3 K and roughly plateaus, while the small frequency shift component (Fig. 5.5(d)) has a relaxation rate that subtly increases as the temperature decreases to 0.4 K, where there is a maximum.

We performed longitudinal field (LF) measurements at a temperature of 0.1 K to test for dynamic magnetism with the results shown in Fig. 5.6. A 50 G applied field decouples a fair amount of the signal, while also changing the shape of the relaxation significantly. Increasing the field to 100 G decouples a significant amount of the signal but increasing the field beyond this does not change the decoupling much, indicating there is some dynamic magnetism.

5.4 Discussion

Our μSR data shows no obvious signs of magnetic order, such as oscillations or a clear Kubo-Toyabe dip and recovery to 1/3 of the initial Asymmetry in ZF (Fig. 5.2). Instead, the raw data shows a gradual increase in the relaxation rate accompanied by a change of shape in the Asymmetry from a Lorentzian relaxation at high-temperature to a Gaussian relaxation at low-temperatures. The Asymmetry may recover to 1/3 of the initial Asymmetry beyond 10 μs but this is very hard to measure at a continuous muon source where beam borne background becomes a non-negligible portion of the signal beyond 10 μs. Our phenomenological model given by Eq. 5.1 describes the data quite well but is unable to provide a smoking gun signature of magnetic ordering.

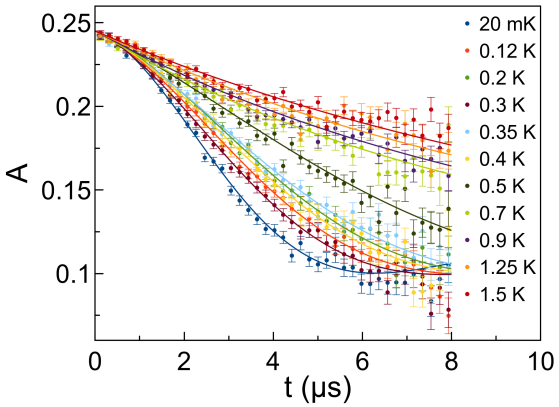

(A) Zero-field Asymmetry of $Sm_2Ti_2O_7$ fit to Eq. 5.1.

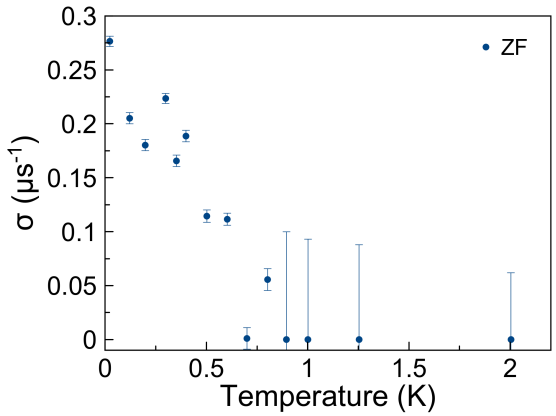

(B) Zero-field Gaussian relaxation rate of $Sm_2Ti_2O_7$ fit to Eq. 5.1.

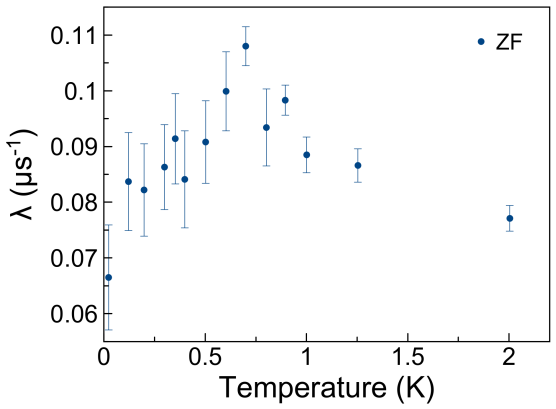

(C) Zero-field Lorentzian relaxation rate of $Sm_2Ti_2O_7$ fit to Eq. 5.1.

Figure 5.2: Zero-field Asymmetry of $Sm_2Ti_2O_7$.

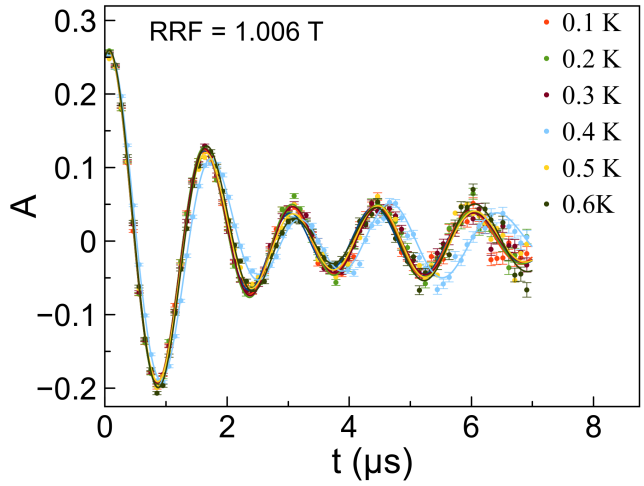

(A) low-temperature high transverse field Asymmetry of $Sm_2Ti_2O_7$
in a rotating reference frame.

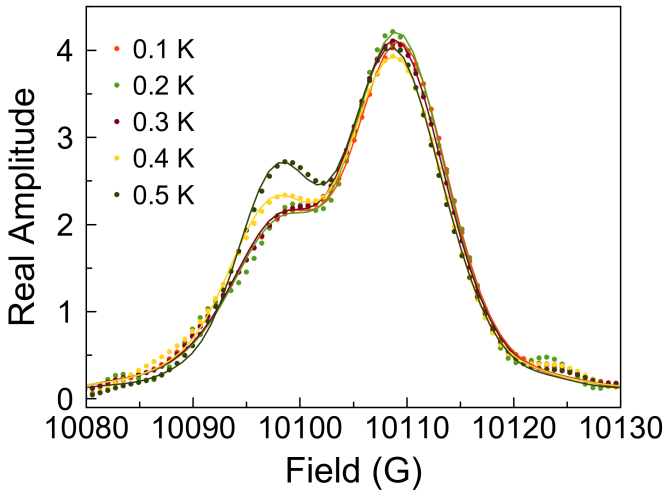

(B) Fourier transform of the low-temperature high transverse field Asymmetry of $Sm_2Ti_2O_7$.

FIGURE 5.3: low-temperature high transverse field Asymmetry of $Sm_2Ti_2O_7$.

As discussed in Sec. 2.5.3, a quickly fluctuating magnetic field produces an exponential relaxation, even if the field probability distribution is Gaussian. At high temperatures, we believe the fluctuation rate of the internal fields is high enough to produce a Lorentzian relaxation while as the temperature is lowered, the fluctuation rate decreases producing a Gaussian relaxation. We have fit the Gaussian component of our signal with a Gaussian Kubo-Toyabe that for small σt closely resembles a Gaussian exponential (as can be seen from Eq. 2.21). Using a Gaussian exponential also fits the

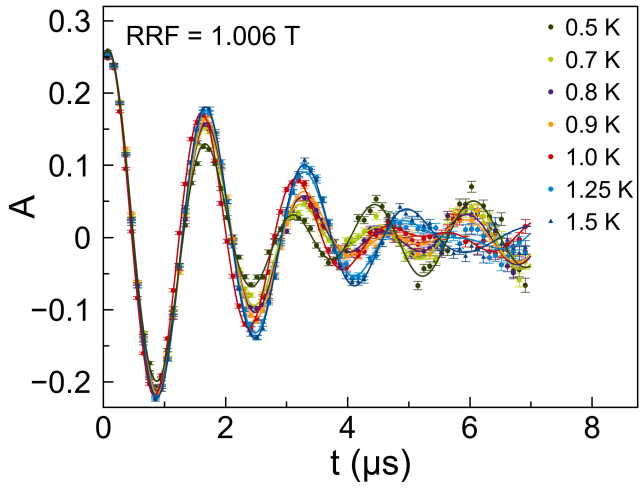

(A) high-temperature high transverse field Asymmetry of $Sm_2Ti_2O_7$ in a rotating reference frame.

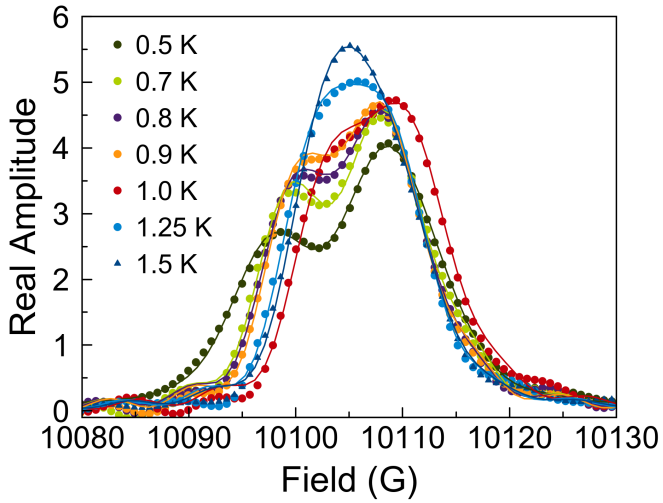

(B) Fourier transform of the high-temperature high transverse field Asymmetry of $Sm_2Ti_2O_7$.

FIGURE 5.4: high-temperature high transverse field Asymmetry of $Sm_2Ti_2O_7$.

data well, however, the large decoupling observed in our LF data (Fig. 5.6) tells us the muon is experiencing a nearly static field, where a Gaussian Kubo-Toyabe is more appropriate. There does still exist magnetic fluctuations at the lowest temperatures as can be seen by a small component that is relaxing in our higher LF measurements and by the fact that our ZF data does not produce high-quality fits without an exponential relaxation multiplying the Gaussian component (not shown). Normally when there are coexisting static and dynamic magnetism the ZF μSR would be fit to the Dynamic

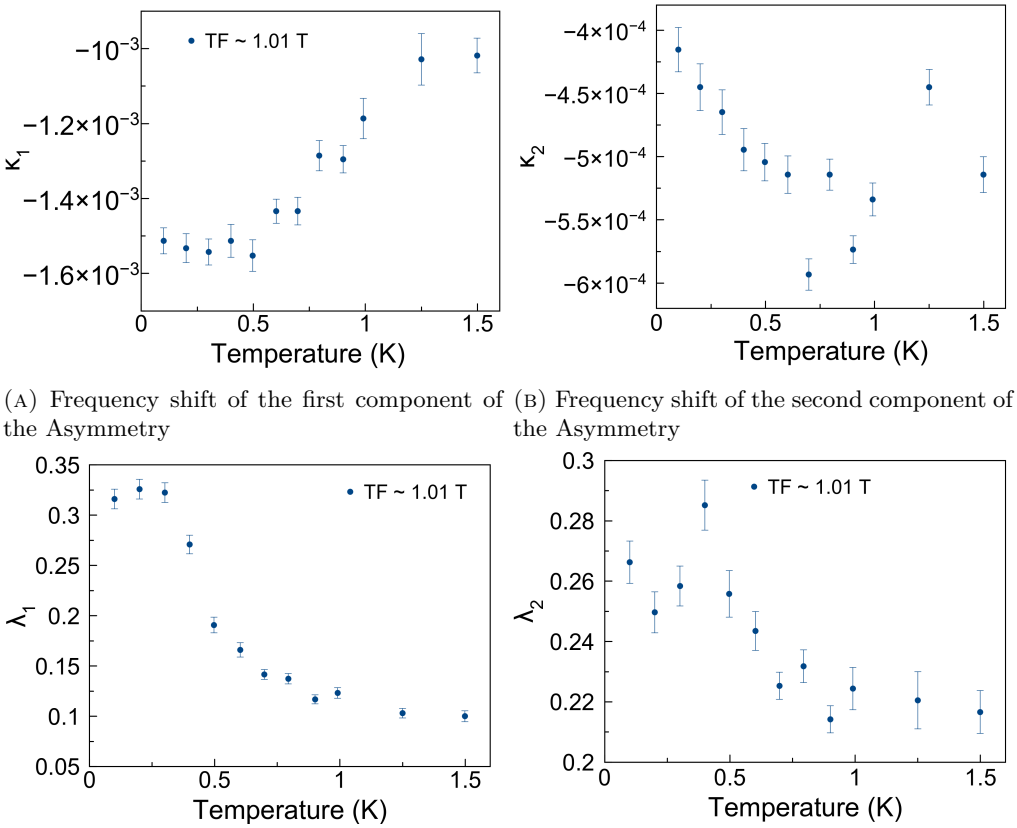

(A) Frequency shift of the first component of the Asymmetry

(B) Frequency shift of the second component of the Asymmetry

(C) Relaxation rate of the first component of the Asymmetry

(D) Relaxation rate of the second component of the Asymmetry

FIGURE 5.5: Fitting results of the high transverse field data to Eq.

Gaussian Kubo-Toyabe, however, this function produces very large error bars at high temperatures. Examining Fig. 2.11 shows that the function depends on the ratio of the fluctuation rate, ν, to the static field distribution width, Δ. Without a clearly observed Kubo-Toyabe dip and recovery to set the scale of Δ, or imposing that Δ has a specific value at some temperature, there is a large range of $\frac{\nu}{\Delta}$ which accurately fits the data, creating a large uncertainty in these parameters. Nevertheless, our ZF and LF data suggest a transition to long-range order with slow persistent spin dynamics.

The persistent spin dynamics may be an indication of the dynamic magnetism expected from moment fragmentation, however, neutron scattering measurements show no evidence of moment fragmentation. The static ordered moment of 0.44(7) μ_B out of a possible 0.43 μ_B measured by [84] leaves the possibility of only a small dynamic moment, however, it may be that the fluctuation rate is so slow as to appear static to neutrons. If the moment did appear static and there was moment fragmentation, there should still be diffuse scattering along the [HHH] and [00L] directions, indicating Coulomb phase

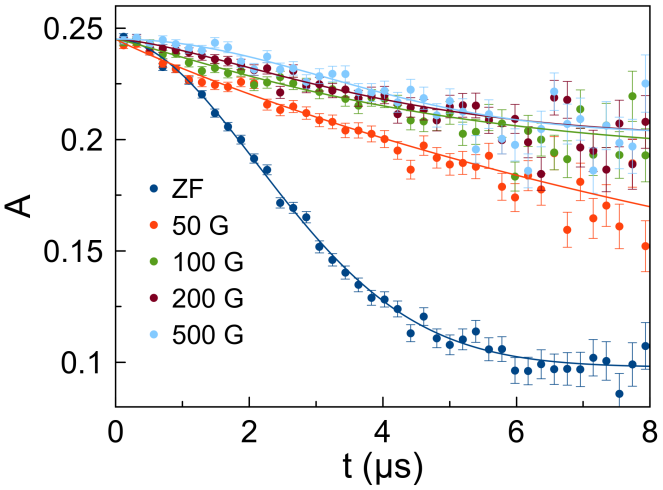

(A) Asymmetry fits in a longitudinal field at base temperature

FIGURE 5.6: $Sm_2Ti_2O_7$ Asymmetry in different applied longitudinal fields at 0.1 K.

correlations, which are not resolved in the measurements of [84]. This rules out the possibility of a large dynamic component of the moment with Coulomb phase correlations, leaving only the possibility of a very small component of the moment being dynamic with Coulomb correlations. Neutron scattering measurements therefore severely limit moment fragmentation as a possible explanation for the dynamic magnetism observed in our μSR measurements.

Measuring persistent spin dynamics within a magnetically ordered state of a geometrically frustrated material is not a new phenomenon; it has been described as "ubiquitous" [107] in a relatively recent review. These materials can be roughly divided into materials that show oscillations in the ZF spectrum of their magnetically ordered state (e.g. $Nd_2Sn_2O_7$ [13] $Gd_2Ti_2O_7$ [39, 146], and $Gd_2Sn_2O_7$ [16]) and those that do not (e.g. $NaCaNi_2F_7$ [19], $Tb_2Ti_2O_7$ [51], $Tb_2Sn_2O_7$ [35], $Er_2Ti_2O_7$ [76], $Yb_2Ti_2O_7$ [34, 9]). A possible explanation for the ubiquitous nature of these spin fluctuations proposed, but not widely endorsed, is that there exist scattering processes involving two magnetic excitations, with a density of states that has an upturn at low energy and a small gap that depends linearly on the temperature [146]. It was later suggested [145] that these excitations are one-dimensional (d=1) spin structures related to the spin loop structures on the pyrochlore lattice considered theoretically by [88] and [64]. A widely endorsed explanation for the spin-dynamics observed in geometrically frustrated materials is lacking, however, there may exist a common explanation for this observation that applies to many of these materials, including $Sm_2Ti_2O_7$.

Our TF measurements (fitting results shown in Fig. 5.5) require two oscillating, exponentially decaying signals to adequately describe the sample signal. The frequency shift of the first component has a magnitude that is approximately ten times the frequency

shift of the second component. Each component comprises about 50% of the signal (53.5± 2% for the small frequency shift component). We use the silver background signal in the data to estimate the background field as the frequency shift of silver is small and temperature-independent in this regime, allowing us to estimate the frequency shift of $Sm_2Ti_2O_7$. The silver signal also allowed us to accurately measure the field drift of the magnet over time.

The frequency shift as a function of temperature is proportional to the susceptibility of the material, which figure 5.5(a) shows increases in magnitude until it plateaus below 0.5 K, for the large frequency shift component. Accompanying this, the relaxation rate (Fig. 5.5(c)) of this component follows a similar behaviour but increases until 0.3 K, then plateaus. This is broadly consistent with a magnetic transition around the expected transition temperature. The frequency shift of the small shift component (Fig. 5.5(b)) has a large spread above 0.5 K with a definite trend of decreasing in magnitude below 0.5 K, while the relaxation rate (Fig. 5.5(d)) increases as the temperature is decreased, possibly peaks at 0.4 K, then is roughly constant below 0.3 K.

A possible explanation of our TF data is that the material breaks up into so-called α and β chains in an applied (110). In an applied (110) field the pyrochlore lattice can be decomposed into two sets of 1-dimensional chains, labelled α and β [141], where the α chains are parallel to the (110) direction while the β chains lie perpendicular to this, along the (1-10) direction. Each set of chains contains 50% of the spins. The spins themselves lie along the local (111) direction due to the CEF anisotropy, however, the description of the spins as quasi-one-dimensional α and β chains is well established in the classical spin-ice materials [48, 111, 30]. More recently it was shown that $Nd_2Zr_2O_7$, with an all-in all-out ground state rather than a spin-ice ground state, also displays this behaviour in a (110) field [141]. In this work, [141] considers the usual XYZ Hamiltonian applicable to dipolar-octupolar doublets in an applied (110) field. In the α chains along (110), the moments alternate between pointing inwards and outwards of each tetrahedron while maintaining a component of their moment along the (110) direction. The behaviour within the β chain can have either ferromagnetic or antiferromagnetic intra-chain character, however, dipolar interactions promote inter-chain antiferromagnetic order in the dipolar spin-ices. This inter-chain interaction is much less important for $Nd_2Zr_2O_7$ due to the reduced moment size, meaning that interactions between β chains are negligible. Ref. [141] shows that the spins on the β chains experience effectively zero molecular field from the α chains and do not couple to the (110) field (at the mean field and nearest neighbour level). Returning to our current investigation of $Sm_2Ti_2O_7$, it may be that the component of the signal with a small frequency shift corresponds to β chains, which should have a small susceptibility since they do not couple to an applied field; at least at the nearest neighbour and mean-field level. The component of the signal with a large frequency shift would then correspond to the α chains, with the approximate 50% weight of each component in the data agreeing with expectations of this model. In this model the magnetic moments on the α and β chains are the same size, explaining why two signals with such different frequency shifts have approximately the same relaxation rate.

5.5 Conclusions

We have performed zero-field (ZF), longitudinal field (LF), and transverse field (TF) μSR measurements on the pyrochlore system $Sm_2Ti_2O_7$. Our ZF measurements show subtle evidence of magnetic ordering through a change of shape in the relaxation as a function of temperature combined with an increased Gaussian relaxation rate at low-temperatures. Our ZF and LF data show evidence of persistent spin dynamics as our ZF data requires a component corresponding to dynamic magnetism at all temperatures and a slowly relaxing component is observed in our high LF data where any static magnetism should be decoupled. We consider the possibility of moment fragmentation as the source of this dynamic magnetism while recognizing the strong limitations neutron scattering results place on this explanation. Our TF measurements with the field applied along the (110) direction contain two components, each comprising $\approx$50% of the signal, that have a large difference in the magnitude of their frequency shifts. Both signals have a change in their features around 0.5 K, which may indicate a magnetic transition into quasi-one-dimensional α and β chains.

Chapter 6

$Dy_2Ti_2O_7$

6.1 Introduction

$Dy_2Ti_2O_7$ is one of the most well-studied pyrochlore systems. It originally generated interest due to its close relation to $Ho_2Ti_2O_7$ which was the first material to show evidence of magnetic frustration in a ferromagnetically interacting system [61]. The (non-zero) zero-point entropy of $Dy_2Ti_2O_7$ was first measured in 1999 [103] where an analogy to the entropy of water-ice was made and the term "spin-ice" was coined. In this state magnetic moments are constrained to lie along the local (111) directions of each tetrahedron due to crystal electric field effects and ferromagnetic interactions cause two of the moments to point into/out of the tetrahedra. Further interest was garnished when Castelnovo *et. al.* [27] showed how the dipole degrees of freedom in the spin-ice state could fractionalize into magnetic monopoles. For a mathematical description of the spin-ice state see Sec. 1.3.1.

Spin-ice correlations measured in early neutron scattering [47] only showed moderate agreement between the Dipolar Spin Ice model (DSIM) for $Dy_2Ti_2O_7$. Later it was shown that a more general dipolar spin-ice model (gDSIM), including interactions up to third nearest-neighbour, could explain the extra scattering at the Brillouin-zone boundary [148]. With the spin-ice state well established in $Dy_2Ti_2O_7$, tremendous effort was taken to measure the magnetic monopoles predicted by Castelnovo *et. al.* [27]. A promising avenue to measure magnetic monopoles is through their signature in the spin dynamics of this material. A μSR study [17] claimed to observe magnetic monopoles through the magnetic Wien effect in transverse field measurements but the observed signal was later shown to be consistent with the Ag sample holder used in the measurement [38]. AC susceptibility has been used extensively to probe spin dynamics in $Dy_2Ti_2O_7$ [118, 115, 83, 108, 147, 126, 73, 45, 56] and has roughly been broken into three temperature regimes; below $\approx$3 K, 3-12 K, and 12-20 K [69]. Here we focus on the low-temperature regime where spin-ice physics becomes relevant.

An early description of the spin dynamics in terms of magnetic monopoles is based upon the the work of Jaubert *et. al.* [69] for the low-temperature regime where the monopoles are dilute and only one monopole or anti-monopole exist on a tetrahedra (corresponding to 3-in/1-out or 1-in/3-out configuration) with no double excitations

(all-in or all-out configurations). The dipole interaction in the spin-ice state becomes a Coulomb interaction in the monopole picture where the interaction is between free particle/anti-particle pairs. This description was improved upon by Castelnovo *et. al.* [27] who used Debye-Huckel theory to predict the monopole density at a given temperature. Debye-Huckel theory is used to treat the monopoles as a magnetic version of an electrolyte; a so-called "magnetolyte". Screening due to the density of magnetic monopoles is expected to produce a dressed charge for an individual monopole and including this in the monopole picture provided good agreement between prediction and measurement of magnetic relaxation times in $Dy_2Ti_2O_7$ down to approximately 1 K [26]. Below this temperature, the magnetic relaxation time increases faster than predicted by Debye-Huckel theory. Returning to the full DSIM offers a better description of the dynamics of the system, however, the low temperature characteristic relaxation time is still underestimated [69]. Both the monopole and DSIM account for the heat capacity and pinch points in the neutron scattering of $Dy_2Ti_2O_7$ very well.

The measured relaxation time from AC susceptibiltiy measurements has been interpreted as having two relevant relaxation processes [83, 108], multiple relaxation processes due to multiple energy scales [69], or more recently due to the system acting as the magnetic analogue of a supercooled liquid [73, 45]. It has become clear that demagnetization [126], boundary [108], impurity [108], and thermal quenching [101, 147] play an important role in the measured relaxation times, making the intrinsic magnetic relaxation properties of the material difficult to measure.

In this work, we probe the equilibrium magnetic relaxation properties of $Dy_2Ti_2O_7$ through AC susceptibility measurements. We account for demagnetisation effects by shaping our samples into ellipsoids and applying appropriate demagnetization factors to measure the intrinsic susceptibility of the material. We grew four single-crystal samples; two in different atmospheric conditions (air and O_2) with stoichiometric ratios of the starting materials and two samples grown in O_2 with a 1% excess/deficiency of Dy_2O_3. We only performed measurements above ≈ 0.65 K with a specific heating protocol for our low-temperature data to ensure the sample was in thermal equilibrium. In this way, we believe we have measured the intrinsic magnetic relaxation properties of $Dy_2Ti_2O_7$.

The model we investigate for the complex AC susceptibility is the Havriliak-Negami (HN) form [62],

$$\chi = \frac{\chi_0}{(1 + (i\omega\tau_{HN})^{\alpha})^{\gamma}}, \tag{6.1}$$

where χ_0 is the DC susceptibility, ω is the angular frequency, τ_{HN} is the characteristic relaxation time, α is a stretching parameter, and γ is an asymmetry parameter. We have neglected the high-frequency contribution χ_∞ as it is constant and contributes less than 1% to the signal at our measured frequencies and temperatures [73]. The model is an extension of the Debye model where $\alpha = \gamma = 1$, which describes a process with a single relaxation time. For $0 \leq \alpha \leq 1$ and/or $0 \leq \gamma \leq 1$ there is a distribution of relaxation times characterized by the width and skew of the distribution. The model is known to describe the dielectric function of polymers and supercooled liquids [62, 44, 128, 28]. To

our knowledge, no other model simultaneously accounts for both the real and imaginary susceptibilities of $Dy_2Ti_2O_7$, over a wide range of frequencies and temperatures, as well as this model does [73, 45]. Simulations of the DSIM by [126] produces qualitatively similar behaviour for the real and imaginary susceptibility, however, the exact shape of the distributions are not captured. It is possible that some of the disagreement between simulation and data in [126] is due to demagnetization effects, that, while small in their samples, could partially produce the observed difference.

To more easily assess if our data follows an HN form for all temperatures, we calculate scaling relations [73] in Appendix B,

$$\mathrm{Re}\left[G\left(\gamma,\chi_0,\chi\right)\right]=\left(\chi_0\right)^{\frac{-1}{\gamma}}\left(\chi'^2+\chi''^2\right)^{\frac{1}{2\gamma}}\cos\left(\frac{1}{\gamma}\arctan\left(\frac{\chi'}{\chi''}\right)\right) \tag{6.2}$$

and

$$\mathrm{Im}\left[G\left(\gamma,\chi_0,\chi\right)\right]=\left(\chi_0\right)^{\frac{-1}{\gamma}}\left(\chi'^2+\chi''^2\right)^{\frac{1}{2\gamma}}\sin\left(\frac{1}{\gamma}\arctan\left(\frac{\chi'}{\chi''}\right)\right). \tag{6.3}$$

These relations are produced by rearranging Eq. 6.1 to have χ_0, χ', χ'', and γ on one side and α, ω, and τ_{HN} on the other. Using some standard complex identities to break the expressions into real and imaginary parts we arrive at Eq. 6.2 and Eq. 6.3. In Appendix B we show that the real and imaginary parts of the function $G\left(\gamma,\chi_0,\chi\right)$ will follow a universal behaviour if the data has an HN form when plotted against $(\omega\tau)^\alpha$, which we plot for different α values in Fig. 6.1. Provided α is temperature-independent, applying the scaling relations Eq. 6.2 and Eq. 6.3 to our measured susceptibilities should cause all of the data to collapse onto a single line given by Eq. B.4 and Eq. B.5 of Appendix B. We shall see that α is weakly temperature dependent for our samples, with $0.9\leq\alpha\leq1$, similar to other measurements performed on tori of $Dy_2Ti_2O_7$ [73, 45].

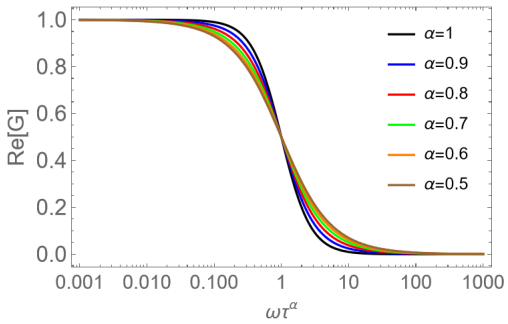

(A) Real part of the scaling relation $G(\chi_0,\chi',\chi'',\gamma)$

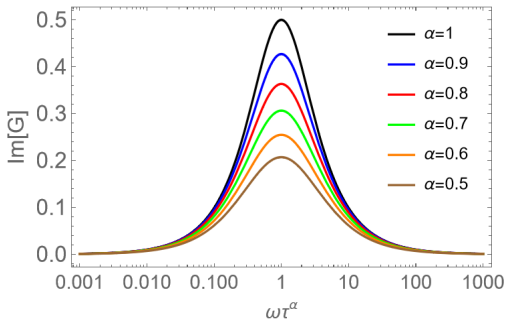

(B) Imaginary part of the scaling relation $G(\chi_0,\chi',\chi'',\gamma)$

FIGURE 6.1: Visualization of the scaling relations.

After establishing that the AC susceptibilities follow an HN form, we check if the characteristic relaxation follows a Vogel–Tammann–Fulcher (VTF) form, an example of

Super-Arrhenius behaviour, given by, [28, 14, 5],

$$\tau = \tau_0 \exp\left(\frac{DT_0}{T - T_0}\right), \tag{6.4}$$

where D is the "fragility" of the material and T_0 is the temperature at which the relaxation time diverges. The characteristic relaxation times of supercooled liquids are known to follow this form. The fragility characterizes how similar or different the relaxation is from Arrhenius law, with large fragility ($D \approx 100$) being similar to Arrhenius relaxation and small fragility ($D \approx 10$) showing large deviations from Arrhenius behaviour. For supercooled liquids, the temperature T_0 represents a temperature where, no matter the cooling procedure used, the system either freezes dynamically into a glassy state or enters an ordered state. For some supercooled liquids, the ordered state can only be entered by waiting an exceedingly long time, far longer than experimental timescales [28].

Early single spin-flip Monte Carlo simulations on the DSIM performed by [88] found that the system falls out of equilibrium and undergoes dynamical freezing with a VTF trajectory. The explanation given for this behaviour is that there exists large energy barriers between distinct, energetically degenerate spin-ice configurations, that stop the system from exploring its full phase-space and finding its true ground state. The goal of [88] is to find the long-range ordered ground state of the DSIM so the above result is somewhat glossed over, and they move to include contributions from loops of spins. While a VTF trajectory describes the simulated dynamics, it is not derived from the microscopic theory and the authors of [88] describe it as an *ad hoc* model. It is interesting to note that in supercooled liquids, large energy barriers separate many degenerate states in a similar manner. These energy barriers physically manifest as domain walls between regions in different degenerate states. The domain walls cost energy to create and equilibrium is reached in the system when the energy cost to create more barriers balances the entropy gain of further dividing a region into different states [28]. Before commenting further on this, let us check if our measurements agree with an HN form for the AC susceptibility and a super-Arrhenius VTF form for the characteristic relaxation time.

6.2 Methods

Four single-crystal samples were grown using the Optical Floating zone technique. Stoichiometric amounts of the starting materials, Dy_2O_3 (99.99%) and TiO_2 (99.99%) were used for two of the growths while two growths had a 1% excess/deficiency of the rare-earth oxide. Crystals of rare-earth oxide titanate pyrochlores are susceptible to "stuffing" [127, 110, 105] where the rare-earth ion takes the place of a titanium ion on the B-site, relieving frustration by allowing additional superexchange pathways that can cause an imbalance in the forces felt by each spin. The non-magnetic B-site Ti^{4+} may be reduced to a magnetic Ti^{3+} ion, again relieving frustration. Additionally, oxygen vacancies randomly distributed throughout the sample can change the local CEF levels in a disordered

way. The magnetic properties of $Yb_2Ti_2O_7$ and $Tb_2Ti_2O_7$ can be significantly altered by as little as a 0.25% excess of rare-earth ion [105] and Monte-Carlo studies on $Dy_2Ti_2O_7$ suggest that stuffing on the 0.3% level can lead to extremely long relaxation times [108]. We test the effect of stuffing on the relaxation times of $Dy_2Ti_2O_7$ by performing three growths at 5 mm/hr in 2 atm O_2 with 1) stoichiometric, 2) 1% excess of the rare-earth ion, and 3) a 1% deficiency of the rare-earth ion. All of the growths came from 20 g batches of the starting materials measured with an accuracy of 0.0005 g, representing an error of 0.0025 %. The starting materials were preannealed at 1000°C for 12 hours with 10 hours to heat up and cooled over a few hours. The materials were weighed immediately after cooling to room temperature and mixed thoroughly using an agate pestle and mortar. The three growths used to test the effect of off-stoichiometry were annealed in O_2 for 24 hours at 1200°C, reground, formed into rods, and annealed again under the same conditions. After growth, the crystals were post-annealed in O_2 at 1200°C for 24 hours to ensure the correct oxidation state of titanium was achieved and to minimize oxygen vacancies. The growth using air was annealed in air for 24 hours at 1200°C, reground, formed into rods, and annealed again under the same conditions. The crystal from this growth was not post-annealed in O_2. Powder XRD measurements show the samples have a pyrochlore phase with no impurities, however, the precise stoichiometry of the samples cannot be determined from these measurements. Samples appear single-crystal by X-ray Laue diffraction.

Samples were ground into ellipsoids using a spherically concave diamond-encrusted Dremel head. Cylindrical-shaped samples were cut from the single-crystals and epoxied to a holding rod. Applying the Dremel head to the sample and rotating the sample in different directions resulted in a semi-ellipsoid which can then be unstuck using acetone or ethanol. The ellipsoidal side of the sample was then reattached to the holding rod and the opposite side was ground in the same manner to form an ellipsoid. The ellipsoids were placed into an irregularly shaped cavity that was sealed on the top and bottom with sand-paper. An air compressor forced the samples to roll inside the cavity until the desired smoothness was reached, usually 12-24 hours. To fit inside of the sample holder of the ^{3}He cryostat, samples were required to have two semi-minor axes diameters less than 4 mm. Samples were measured 3-5 times on each axis using calipers accurate to 0.005 mm, from which we estimate a maximum error of 0.05 mm.

Table 6.1 shows the measured properties of each ellipsoid, the measurement axis and the demagnetization factor, N from tables in [95]. Uncertainties for N are estimated from the tables where it should be noted that ellipsoids with a higher eccentricity have a larger error. The intrinsic real, χ', and imaginary, χ'', susceptibilities can be calculated from the measured susceptibilities, χ_M, using the formula's [82],

$$\chi' = \frac{\chi'_M - 4\pi N\left(\chi'^2_M + \chi''^2_M\right)}{\left(1 - 4\pi N\chi'_M\right)^2 + \left(4\pi N\chi''_M\right)^2}, \tag{6.5}$$

Sample Uncertainty	mass (g) 0.000005	a-axis (mm) 0.05	b-axis (mm) 0.05	c-axis (mm) 0.05	axis	N [95]
$Dy_2Ti_2O_7$ O_2	0.09825	2.93	2.97	3.20	c	0.315±5%
$Dy_{2.02}Ti_2O_{7.03}$	0.135460	3.35	3.38	3.42	a	0.335±4%
$Dy_{1.98}Ti_2O_{6.97}$	0.065860	2.43	2.48	2.83	a	0.355±9%
$Dy_2Ti_2O_7$ Air	0.245160	3.88	3.92	4.20	c	0.317±4%

TABLE 6.1: Ellipsoid Properties.

and

$$\chi'' = \frac{\chi''_M}{(1 - 4\pi N\chi'_M)^2 + (4\pi N\chi''_M)^2}, \tag{6.6}$$

where the measured susceptibilities are the volume susceptibilities in CGS units.

Reaching thermal equilibrium with a heat bath can take exceedingly long for this material below about 0.6 K [101, 147]; on the order of days or weeks. Above 0.65 K thermal relaxation times are on the order of thousands of seconds. For this reason, and the fact that our SQUID is only calibrated for AC measurements down to 0.1 Hz, we restrict ourselves to temperatures above 0.65 K. Below 0.65 K the peak in the imaginary susceptibility lies below 0.1 Hz, making a measurement of the relaxation time difficult. We stress again that great care is required to ensure the sample is in thermal equilibrium with the bath. Our ^{3}He system at McMaster goes through a condensation procedure to reach temperatures below 2 K. During this process ^{3}He is added into the sealed sample chamber in short bursts until both the temperature and pressure reach the desired values. At a temperature of 1.65 K, a valve opens allowing ^{3}He to return to the storage chamber from the sample chamber, resulting in a rapid drop in temperature to 0.9 K over about a minute. Turning off all heaters in the sample chamber and pumping on the chamber with a turbopump allows the sample chamber to reach a temperature of 0.49 K in around 30 minutes. The temperature is held here for 5 minutes, then increased at a rate of 0.01 K/min until the measurement temperature is reached. The sample is then held at this temperature for 10 minutes before measurement starts. For an AC measurement, a signal nulling process is done before the start of each measurement that takes approximately 30 minutes for measurements in the 0.1-1.0 Hz range and 5-10 minutes for measurements above 1.0 Hz. Measurements are taken sequentially in increasing frequency at a constant temperature. As time goes on and pumping continues on the sample chamber, the amount of ^{3}He in the chamber decreases. Eventually, temperature stability is lost due to a lack of ^{3}He in the chamber and the ^{3}He needs to be recondensed. Each temperature required recondensing at least 4 times to measure the entire frequency range if everything went smoothly during measurement. During condense mode the temperature initially spikes to 3-5 K then slowly settles to about 1.7 K. Once this temperature is reached the system adds in more ^{3}He in bursts causing the sample chamber temperature to jump to 2 K and then oscillate between 1.7 K and 2 K until the chamber is full. The whole process takes 3-4 hours, following which the above cooling treatment is again followed

for measurement temperatures below 1.0 K. For temperatures at and above 1.0 K the system was not taken to 0.48 K and instead sat at 0.85 K for 20 minutes before heating to the required temperature at 0.01 K/min.

For each frequency point, three measurements were performed each of which includes a measurement with the sample in the center of the second-order gradiometer and with the sample 3 cm away, above the second-order gradiometer, to be used as background subtraction. The measurement with the sample removed from the gradiometer will detect any signals produced by the electronics that are not being completely removed by the system, allowing them to be subtracted off from the measurement of the sample. Unfortunately, there is a temperature gradient within the sample chamber of a few tens of mK due to the heaters being located above the sample. Moving the sample upwards increases the sample temperature, which the system tries to compensate for while returning the sample to the initial position decreases the sample temperature. Tremendous effort was undertaken to find heater and turbopump settings, at each temperature, which allowed for adequate temperature stability during measurement. Often the first measurement taken in a sequence of measurements needed to be redone due to the large temperature change during the cooling procedure. If there was any evidence that the sample was not in thermal equilibrium during measurement, such as a spike in temperature during measurement or a spurious result, the measurement was retaken. Measurements were rejected if the maximum/minimum temperature during measurement was more than 25 mK from the setpoint or if the average temperature was more than 13 mK away from the setpoint. Each measurement takes between 0.05 and 10 seconds to perform, making it unlikely that the sample temperature changed by this much during measurement.

We developed python code to fit the complex AC susceptibility data to Eq. 6.1. The python uncertainties package was used to calculate and propagate the uncertainty values from the measured quantities while the curvefit function from the scipy optimize package was modified to simultaneously fit the real and imaginary parts of the data. The python code also applied the scaling relations, Eq. 6.2 and Eq. 6.3 to the measured quantities and calculated $(\omega\tau)^{\alpha}$ to make the scaled AC susceptibility plots.

6.3 Results

Fig. 6.2 displays the effect of the demagnetisation corrections for the O_2 grown sample. A Cole-Cole plot for the demagnetisation corrected (Fig.6.2(a)) and uncorrected (Fig.6.2(b)) susceptibilities clearly shows the importance of this correction in a large moment sample such as $Dy_2Ti_2O_7$. Fig. 6.2(c) and Fig. 6.2(d) show the intrinsic susceptibilities as a function of the raw susceptibilities, highlighting the non-linearity of these corrections. It is apparent that demagnetisation effects must be accounted for by either shaping the samples into a geometry which does not depend on demagnetisation (Tori) or one for which the effect has been measured (ellipsoids).

The demagnetisation corrected real and imaginary susceptibilities along with the scaled susceptibilities are shown for O_2 grown $Dy_2Ti_2O_7$ (Fig. 6.3), Dysprosium deficient

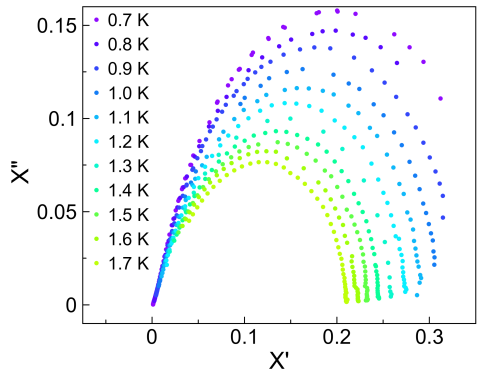

(A) Demagnetisation corrected Cole-Cole plot.

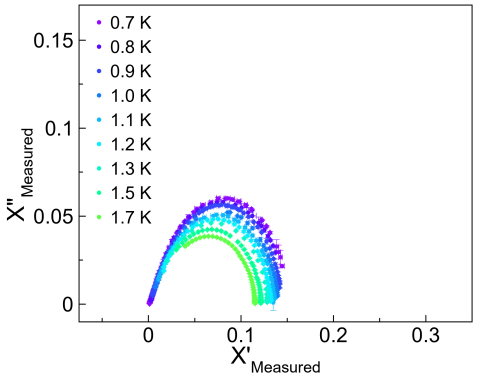

(B) Uncorrected Cole-Cole plot

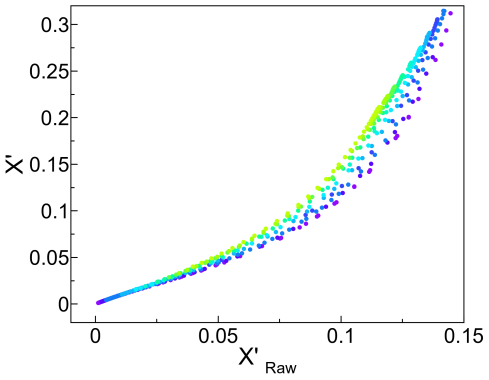

(C) Demagnetisation corrected real susceptibility as a function of the raw, measured susceptibility

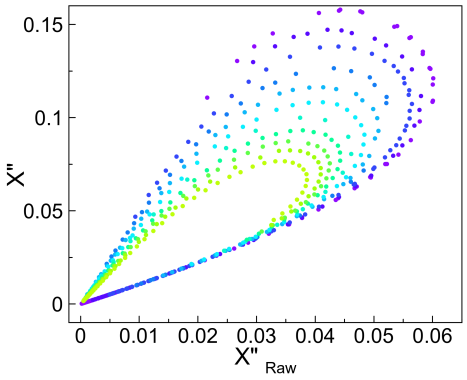

(D) Demagnetisation corrected imaginary susceptibility as a function of the raw, measured susceptibility

FIGURE 6.2: Effect of the demagnetisation corrections

$Dy_{1.98}Ti_2O_{6.97}$ (Fig. 6.4), Dysprosium over-abundant $Dy_{2.02}Ti_2O_{7.03}$ (Fig. 6.5), and air-grown $Dy_2Ti_2O_7$ (Fig. 6.6). All of the samples grown in O_2 show remarkably similar susceptibility behaviour and are well described by the HN form of Eq. 6.1. The air-grown sample is well described by this form as well but it has a peak in the imaginary susceptibility which shifts to a higher frequency at a lower temperature than the other samples. Above 1.5 K the center of the peak is above our maximum frequency, causing large errors in the fitting parameters for the air-grown sample. As all samples follow an HN form, this suggests that all samples are acting as supercooled liquids in this temperature regime.

The HN fitting parameters are shown as a function of temperature in Fig. 6.7. These parameters show the same qualitative behaviour as the measurements done on tori of $Dy_2Ti_2O_7$ [72, 45]. All of the samples we grew have similar properties with some exceptions. The stretching parameter, γ, of the Dysprosium deficient sample is lower than for the other samples, indicating that the distribution of relaxation times is more asymmetric for $Dy_{1.98}Ti_2O_{6.97}$. The characteristic relaxation time of the air-grown

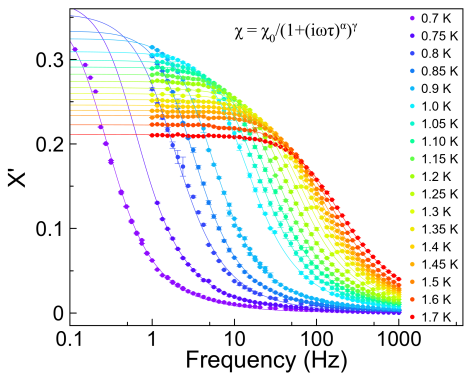

(A) Real susceptibility of O2 grown $Dy_2Ti_2O_7$.

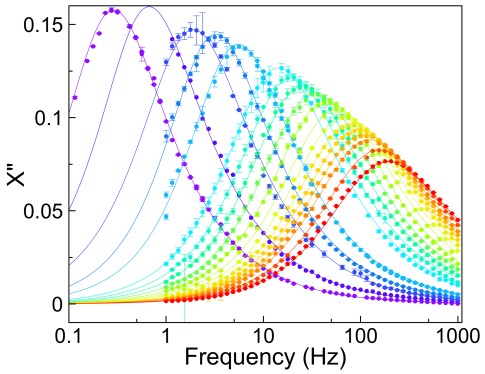

(B) Imaginary susceptibility of O2 grown $Dy_2Ti_2O_7$.

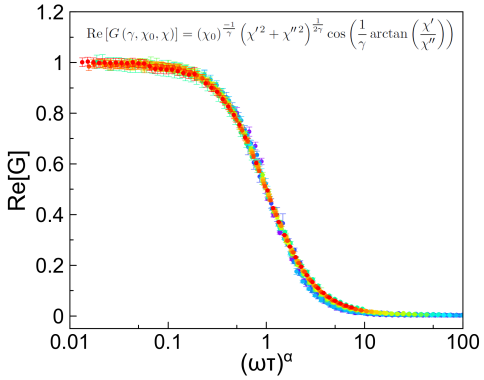

(C) Scaled real susceptibility (Eq. 6.2) of O2 grown $Dy_2Ti_2O_7$.

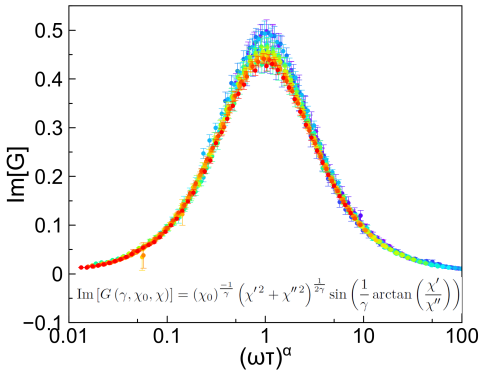

(D) Scaled imaginary susceptibility (Eq. 6.3) of O2 grown $Dy_2Ti_2O_7$.

FIGURE 6.3: Demagnetization corrected real and imaginary susceptibility along with the scaled real and imaginary susceptibility for O_2 grown $Dy_2Ti_2O_7$

sample is about a factor of 10 shorter, has a higher high-temperature α, and a lower high-temperature γ value than for the O_2 grown samples. Finally, the DC susceptibility per cm^3, χ_0, is about 10% higher in the 1% excess and about 5% lower in the 1% deficient samples than for the stoichiometric air and O_2 samples, larger than what would be expected from a 1% increase/decrease in the density of $Dy3^+$ ions.

We check the behaviour of the relaxation time as a function of temperature in Fig. 6.8, comparing the relaxation time to the Super-Arrhenius VTF model in Fig. 6.8(a) and to an Arrhenius form in Fig. 6.8(b). The VTF form provides a better description of the characteristic relaxation time than the Arrhenius model for all samples. The final results of the fits are displayed in Table 6.2 along with the fitting results of four other works. Good agreement is seen between the characteristic relaxation time of our stoichiometric O_2 grown sample and the other references for the Super-Arrhenius model. The divergence temperature, T_0, and fragility, D, also show good agreement. Comparing our Arrhenius fitting results to those of [147] shows moderate agreement, however, [147]

fit an Arrhenius model at lower temperatures than we did. Considering that we have demonstrated the system follows a VTF form, it should be expected to get different fitting results when using an Arrhenius model with a different fitting range.

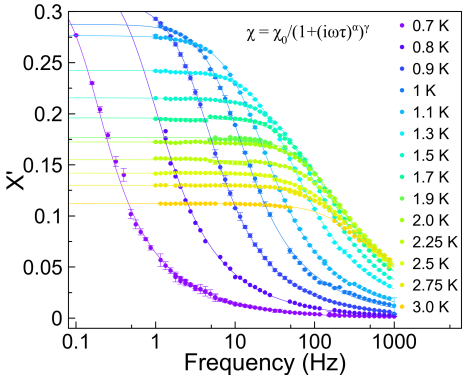

(A) Real susceptibility of $Dy_{1.98}Ti_2O_{6.97}$.

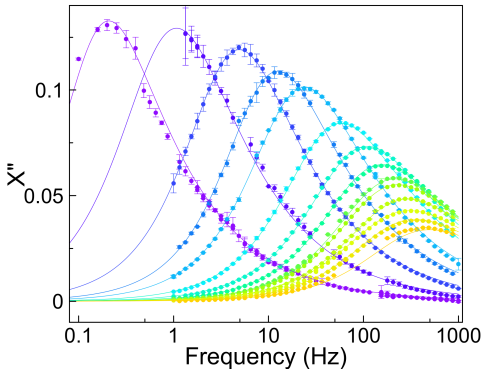

(B) Imaginary susceptibility of $Dy_{1.98}Ti_2O_{6.97}$.

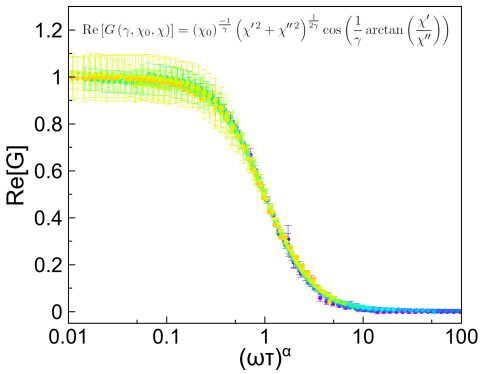

(C) Scaled real susceptibility (Eq. 6.2) of $Dy_{1.98}Ti_2O_{6.97}$.

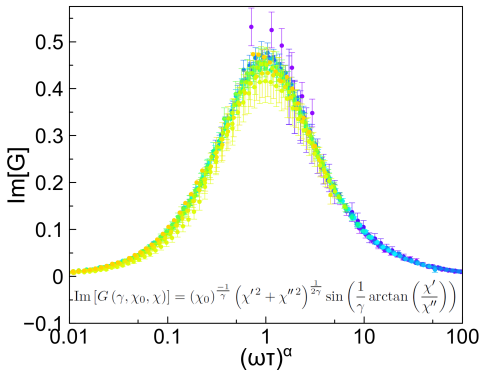

(D) Scaled imaginary susceptibility (Eq. 6.3) of $Dy_{1.98}Ti_2O_{6.97}$.

Figure 6.4: Demagnetization corrected real and imaginary susceptibility along with the scaled real and imaginary susceptibility for of $Dy_{1.98}Ti_2O_{6.97}$

6.4 Discussion

In Fig. 6.8(a) we show that the characteristic relaxation time of $Dy_2Ti_2O_7$ is well described by the Vogel–Tammann–Fulcher (VTF) trajectory (Eq. 6.4), while Fig. 6.8(b) shows that an Arrhenius form provides a poor fit of the relaxation times. The AC susceptibility is well described by a Havriliak-Negami (HN) form, Eq.6.1, which can be seen in figures 6.3-6.6. These results in combination indicate that the system is acting as a magnetic supercooled liquid analogous to dielectric glass-forming liquids. This model provides a better description of the dynamics of the system than both Debye-Huckel theory for magnetic monopoles and the DSIM. The Debye-Huckel and DSIM models predict a faster than Arrhenius increase in the characteristic relaxation times, however,

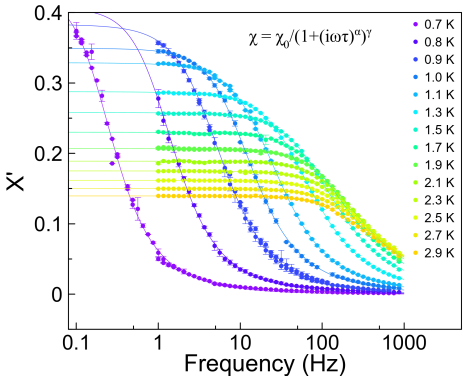

(A) Real susceptibility of $Dy_{2.02}Ti_2O_{7.03}$.

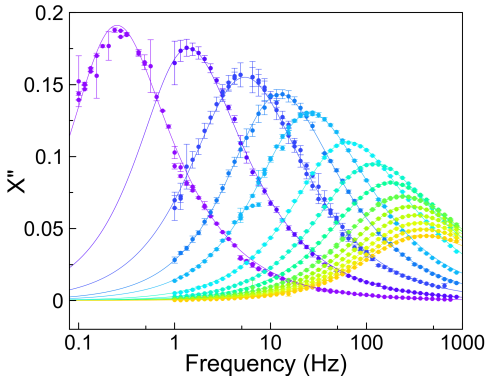

(B) Imaginary susceptibility of $Dy_{2.02}Ti_2O_{7.03}$.

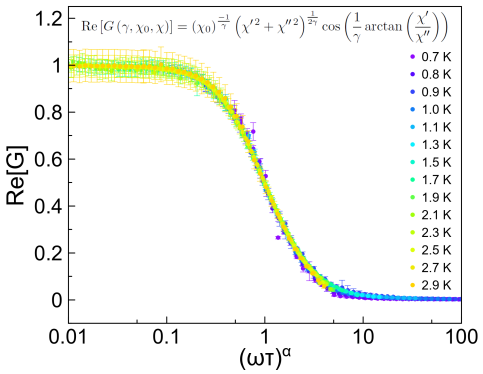

(C) Scaled real susceptibility (Eq. 6.2) of $Dy_{2.02}Ti_2O_{7.03}$.

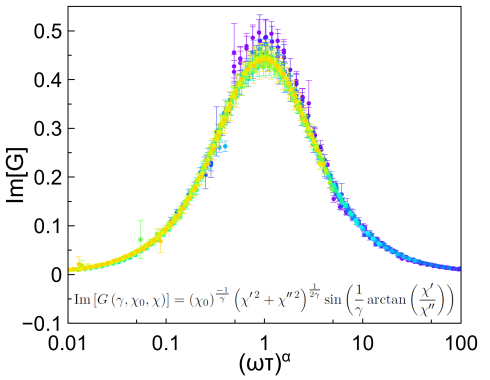

(D) Scaled imaginary susceptibility (Eq. 6.3) of $Dy_{2.02}Ti_2O_{7.03}$.

FIGURE 6.5: Demagnetization corrected real and imaginary susceptibility along with the scaled real and imaginary susceptibility for of $Dy_{2.02}Ti_2O_{7.03}$

the increase in relaxation times is still slower than what is observed in the real material [27]. Provided that the Monte Carlo simulations performed can capture all behaviour of the Debye-Huckel and the DSIM, we must conclude they do not offer a complete description of the physics $Dy_2Ti_2O_7$. One possibility is that clusters of spins, such as a zero magnetisation hexagonal ring, act as either a perturbation or replacement for the DSIM [149]. These clusters would be another example of emergent composite spin clusters in frustrated systems.

Surprisingly, the VTF and HN behaviour are robust against disorder as all four of our samples follow these forms. This is quite different from the extreme sensitivity seen in $Tb_2Ti_2O_7$ and $Yb_2Ti_2O_7$ [105]. The four samples grown are expected to have different types of defects which may affect their properties. We assume the defects in each sample are randomly distributed throughout the crystal and have no reason to believe their locations should be correlated. The Dysprosium overabundant sample is more susceptible to stuffing, the dysprosium deficient sample is more susceptible to anti-stuffing

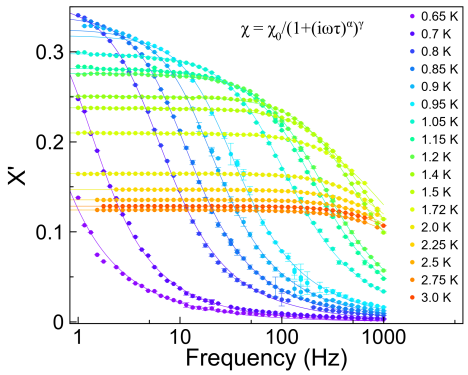

(A) Real susceptibility of air-grown $Dy_2Ti_2O_7$.

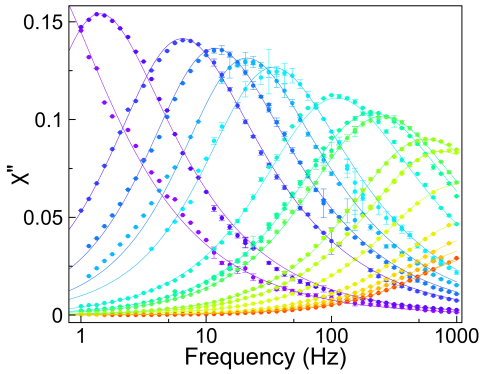

(B) Imaginary susceptibility of air-grown $Dy_2Ti_2O_7$.

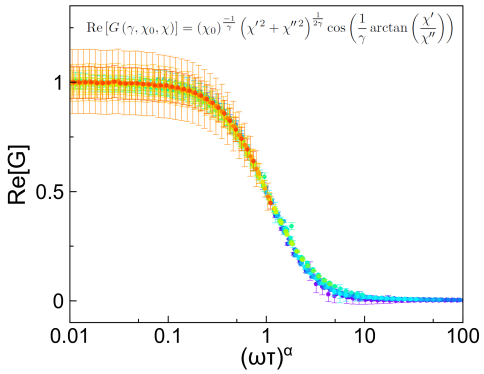

(C) Scaled real susceptibility (Eq. 6.2) of air-grown $Dy_2Ti_2O_7$.

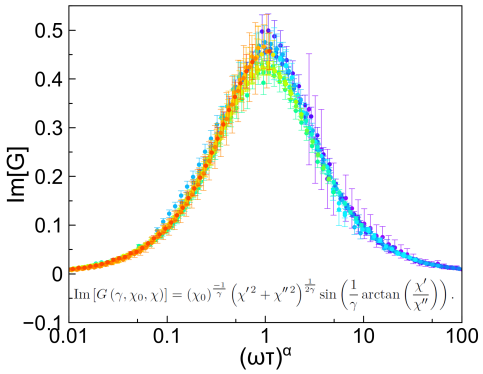

(D) Scaled imaginary susceptibility (Eq. 6.3) of air-grown $Dy_2Ti_2O_7$.

Figure 6.6: Demagnetization corrected real and imaginary susceptibility along with the scaled real and imaginary susceptibility for air-grown $Dy_2Ti_2O_7$

and Dysprosium/Oxygen vacancies, while the air-grown sample is more susceptible to Oxygen vacancies. Revell *et. al.* [108] used simulations to show that stuffing can act to trap monopoles near stuffed sites. According to [108] trapping monopoles around defects results in very long relaxation times. We believe excitations are being more effectively trapped around defects in our Dysprosium deficient and overabundant samples as τ_0 is a factor of 2 larger in these samples. The β value of the Dysprosium deficient sample indicates a more asymmetric distribution of relaxation times than for the stoichiometric or Dysprosium overabundant sample. Dysprosium vacancies or titanium anti-stuffing would reduce the number of pathways a spin-ice violating spin has to propagate through the sample. If recombination of a 3-in 1-out tetrahedra and 1-in 3-out tetrahedra is the main source of relaxation then these defects would increase relaxation times. It is interesting that these types of defects produce a more asymmetric relaxation time than stuffing does in the Dysprosium overabundant sample. Monte-Carlo studies on Dysprosium deficient $Dy_2Ti_2O_7$ could help to elucidate this behaviour. For the air-grown

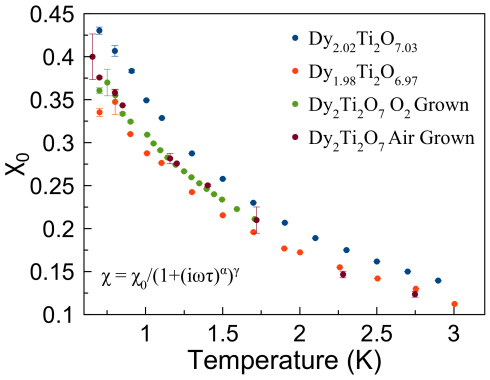

(A) DC susceptibiltiy parameter, χ_0.

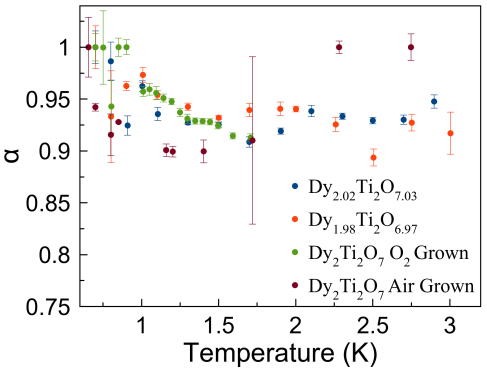

(B) α stretching parameter

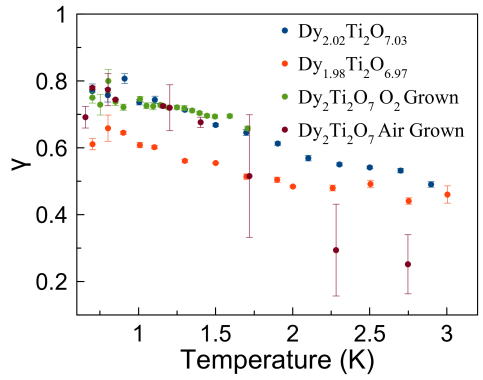

(C) γ asymmetry parameter

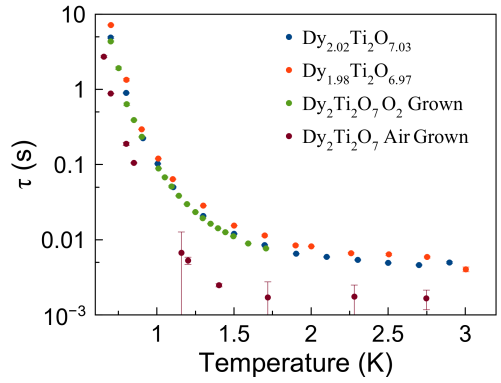

(D) Havriliak-Negami characteristic relaxation time

FIGURE 6.7: Havriliak-Negami fitting parameters for $Dy_2Ti_2O_7$ with different growth conditions

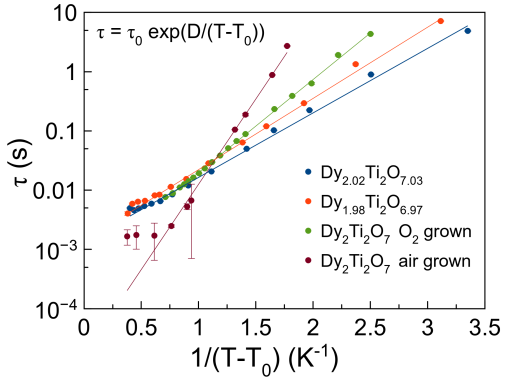

(A) Relaxation times fit to the Super-Arrhenius model.

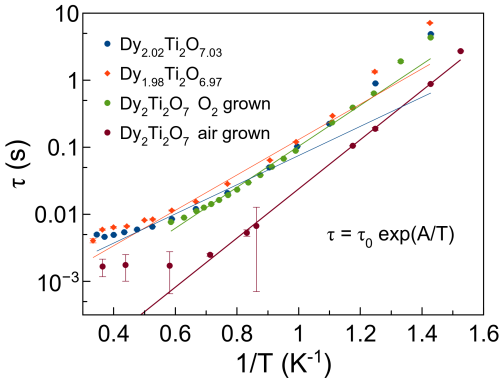

(B) Relaxation times fit to an Arrhenius model

FIGURE 6.8: Comparing the characteristic relaxation time to a Super-Arrhenius and Arrhenius form.

Sample	Model				
	Arrhenius		Super-Arrhenius		
	τ_0 (s)	E_a (K)	τ_0 (s)	T_0 (K)	D
$Dy_2Ti_2O_7$ O_2	9.1(2)E-5	7.0(2)	5.3(5)E-4	0.301(3)	12(1)
$Dy_{2.02}Ti_2O_{7.03}$	5(2)E-4	5.0(5)	1.3(4)E-3	0.40(2)	6.2(9)
$Dy_{1.98}Ti_2O_{6.97}$	3.0(8)E-4	6.1(3)	1.4(1)E-3	0.38(1)	7.3(6)
$Dy_2Ti_2O_7$ Air	5(1)E-6	8.4(2)	2(1)E-5	0.09(6)	72(5)
$Dy_2Ti_2O_7$ [72, 73]			1.9(3)E-4	0.24(2)	14(1)
$Dy_2Ti_2O_7$ [45]			1.4E-4	0.26	14
$Dy_2Ti_2O_7$ [43, 42]			1.0(2)E-4	0.25(10)	11(7)
$Dy_2Ti_2O_7$ [147]	1.6E-5	9.8			

TABLE 6.2: Relaxation parameters of the samples when fit to an Arrhenius and Super-Arrhenius model. Errors indicate the error on the last digit displayed or are left blank where errors were not given

sample, there may be a higher proportion of Dysprosium ions with a different CEF scheme and g-tensor than usual due to oxygen vacancies. We hypothesize that these Dysprosium ions offer another mode of relaxation for spin-ice violating defects, thereby reducing the relaxation times in this sample.

The temperature at which relaxation times diverge, T_0 is larger for the O_2 grown samples whereas the air-grown sample has a lower T_0. The fragility parameter, D, is also much lower in O_2 grown samples than in the air-grown sample. This combination indicates that the O_2 grown samples are more *fragile* liquids than the air-grown sample. The most straightforward implication of this is that the O_2 grown samples are better described by a Super-Arrhenius form and therefore relaxation is not (solely) due to thermally activated processes. For glass-forming liquids, fragility measures how quickly relaxation times increase at the glass transition, with low fragility indicating a strong increase in relaxation times at the glass transition. The fragility and divergence temperature of our stoichiometric O_2 grown sample are close to the values from the studies on tori [73, 45] and the noise spectrum [42] even though these measurements probed higher temperatures and frequencies than we were able to access.

Regardless of the exact fitting parameters, we have demonstrated that the supercooled liquid behaviour identified in AC susceptibility measurements is robust against many types of disorder applicable to $Dy_2Ti_2O_7$. As a further test of this, measurements on recent ultra-pure samples [9] could be performed in the future. To further demonstrate the supercooled liquid behaviour of this system, time-domain measurements, examining how the system relaxes after turning a field on or off, could be performed. The expected behaviour for this measurement is a stretched exponential Kohlrausch-Williams-Watts form and has been measured in Tori [73, 45].

6.5 Conclusions

We have grown four different samples of $Dy_2Ti_2O_7$ and measured their demagnetisation corrected AC susceptibility. The samples were a stoichiometric O_2 grown sample, a 1% Dysprosium overabundant sample, a 1% Dysprosium deficient sample, and a stoichiometric air-grown sample. We find the AC susceptibilities are well described by a Havriliak-Negami form while the characteristic relaxations are described by a Vogel–Tammann–Fulcher form indicating the samples are acting as a magnetic supercooled liquid analogous to dielectric glass-forming liquids. This demonstrates that this behaviour is robust against the types of disorder most applicable to $Dy_2Ti_2O_7$, such as stuffing. The observation of a Vogel-Tamman-Fulcher form for the characteristic relaxation time is an improvement upon the Dipolar Spin Ice model and we must conclude that this model is an incomplete description of $Dy_2Ti_2O_7$.

Chapter 7

Type-I Superconductivity in BeAu

7.1 Summary of Publication

In this chapter we present the published manuscript "μSR and Magnetometry study of the Type-I Superconductor BeAu". Originally it was thought that BeAu was a type-II superconductor based on magnetisation measurements of this material. When we performed μSR measurements in the superconducting state of this material we found that the internal field was larger than the applied field and that there was a large, unexplained, missing asymmetry. This is at odds with the expectation that the majority of the field distribution lies below the applied field and the full asymmetry should be observed for a type-II superconductor. It was quickly realized that these results could be explained by type-I superconductivity.

Including demagnetisation effects, the full volume of a type-I superconductor does not have to be in the Meissner state below T_c and H_c. The demagnetising field can cause the total magnetic field at the surface of the sample to exceed H_c in certain regions, forcing the material to enter the normal state in these regions. This is known as the intermediate state of a type-I superconductor. It turns out that the free energy is minimized within the sample if these normal regions have a field (roughly) equal to the critical field. Thus, you end up in a situation with regions of the sample in the Meissner state, with zero field, and regions of the sample in the normal state, with an internal field of H_c higher than the applied field, precisely what we observed in our transverse field μSR measurements. By performing temperature sweeps at constant field, we were able to measure H_c as a function of temperature using μSR.

With this result in hand we set out to correct the previous magnetisation measurements by shaping our sample into an ellipsoid, allowing us to account for demagnetisation effects. Combining our μSR and magnetisation results we find a value of $H_c = 258$ Oe. We then perform susceptibility measurements under pressure and find that under 450 MPa, T_c decreases by 35 mK, similar to what is seen in other type-I superconductors. Our results demonstrate the utility of μSR measurements to type-I superconductors, which is much well less established than for type-II supeconductors.

μSR and magnetometry study of the type-I superconductor BeAu

J. Beare,[1] M. Nugent,[1] M. N. Wilson,[1] Y. Cai,[1] T. J. S. Munsie,[1] A. Amon,[2] A. Leithe-Jasper,[2] Z. Gong,[3] S. L. Guo,[4] Z. Guguchia,[3] Y. Grin,[2] Y. J. Uemura,[3] E. Svanidze,[2] and G. M. Luke[1,5,6]

[1]*Department of Physics and Astronomy, McMaster University, Hamilton, Ontario, Canada L8S 4M1*
[2]*Max-Planck-Institut für Chemische Physik fester Stoffe, Nöthnitzer Straße 40, 01187 Dresden, Germany*
[3]*Department of Physics, Columbia University, New York, New York 10027, USA*
[4]*Department of Physics, Zhejiang University, Hangzhou 310027, China*
[5]*Canadian Institute for Advanced Research, Toronto, Ontario, Canada M5G 1Z7*
[6]*TRIUMF, Vancouver, British Columbia, Canada V6T 2A3*

(Received 31 January 2019; published 11 April 2019)

We present muon spin rotation and relaxation (μSR) measurements as well as demagnetizing-field-corrected magnetization measurements on polycrystalline samples of the noncentrosymmetric superconductor BeAu. From μSR measurements in a transverse field, we determine that BeAu is a type-I superconductor with $H_c = 258$ Oe, amending the previous understanding of the compound as a type-II superconductor. To account for demagnetizing effects in magnetization measurements, we produce an ellipsoidal sample, for which a demagnetization factor can be calculated. After correcting for demagnetizing effects, our magnetization results are in agreement with our μSR measurements. Using both types of measurements, we construct a phase diagram from $T = 30$ mK to $T_c \approx 3.25$ K. We then study the effect of hydrostatic pressure and find that 450 MPa decreases T_c by 35 mK, comparable to the change seen in the type-I elemental superconductors Sn, In, and Ta. This suggests BeAu is far from a quantum critical point accessible by the application of pressure.

DOI: 10.1103/PhysRevB.99.134510

I. INTRODUCTION

The absence of inversion symmetry in noncentrosymmetric superconductors results in an antisymmetric spin-orbit coupling, which splits otherwise degenerate electronic bands [1]. Parity of the superconducting parameter is no longer conserved, allowing spin-singlet and spin-triplet states to mix. These mixed-parity states are generally expected to give rise to point or line nodes in the superconducting gap [2–4].

Evidence for line nodes has been found in $CePt_3Si$ [5], $CeIrSi_3$ [6], $Mg_{10}Ir_{19}B_{16}$ [7], Mo_3Al_2C [8], and Li_2Pt_3B [9], while many other noncentrosymmetric superconductors possess fully gapped states [10–15]. Other noncentrosymmetric superconductors such as La_2C_3 [16] and $TaRh_2B_2$ exhibit multigap behavior. A detailed analysis of the possible pairing mechanisms [17] shows that either isotropic or nodal gaps are possible, depending on the anisotropy of the pairing mechanism. The anisotropy may depend upon the strength of spin-orbit coupling in the material [10].

In addition to breaking parity symmetry, noncentrosymmetric superconductors can also exhibit time-reversal symmetry breaking. Muon spin rotation and relaxation (μSR) has been used to detect time-reversal symmetry breaking in the noncentrosymmetric superconductors Re_6D (D = Zr, Hf, Ti) [18–20], La_7Ir_3 [13], $LaNiC_2$ [14], and SrPtAs [21] as well as several centrosymmetric superconductors [22–29]. Further study of noncentrosymmetric superconductors, such as BeAu, is required to probe the unconventional pairing mechanisms and explore the diverse gap properties that have been exhibited.

BeAu exhibits cubic space-group symmetry of $P2_13$ (FeSi) with lattice parameter $a = 4.6699(4)$ Å. From previous work [30], BeAu exhibits conventional Bardeen-Cooper-Schrieffer-type superconductivity below $T_c \approx 3.3$ K with a full Meissner flux expulsion. The specific heat jump at the superconducting transition is equal to the normal state-specific heat, indicating bulk superconductivity. BeAu can be classified as a weakly coupled superconductor with $\Delta C/\gamma_n T_c \approx 1.26$, $\lambda_{e-p} = 0.5$, and $2\Delta(0)/k_B T_c = 3.72$. Previously [30], BeAu was thought to be a type-II superconductor with lower critical field $H_{c1} = 32$ Oe and upper-critical field $H_{c2} = 335$ Oe based upon magnetization measurements which used a spherical demagnetization factor $N = \frac{1}{3}$ when measuring an irregularly shaped sample. This is a common first assumption when correcting for demagnetizing effects that we would like to improve upon in this paper. Zero-field μSR measurements presented in Ref. [30] show no time-reversal symmetry breaking.

μSR is a powerful technique which can be used to measure internal fields due to time-reversal symmetry breaking as well as give an accurate measurement of the penetration depth and coherence length of type-II superconductors. As muons are a local probe of magnetism, μSR is insensitive to the large demagnetizing fields produced outside of superconductors. In this paper, transverse field (TF) μSR measurements are used to demonstrate that BeAu is a type-I superconductor with $H_c = 258$ Oe. Demagnetizing effects in superconductors can cause parts of a sample to experience a magnetic field that is larger than the applied field. If the local field due to demagnetizing effects at the surface of a type-I superconductor is above H_c, then at least part of the sample will enter the normal state. In this situation, the free energy is minimized by a complicated structure of alternating normal and superconducting regions which depends upon the geometry

of the sample, as well as the coherence length and penetration depth [31–33]. This is known as the intermediate state of a type-I superconductor and occurs for applied fields, H_a, between $(1 - N)\, H_c$ and H_c, where N is the demagnetization factor of the sample. At low applied fields, close to $(1 - N)\, H_c$, the free energy of the intermediate state is minimized when the normal regions of the sample have an internal field of H_c. At high magnetic fields, close to H_c, interface effects between normal and superconducting regions, as well as surface effects, modify the thermodynamic critical field to a slightly reduced value H_{cI} [31–33]. The magnetic moment of a muon landing within a type-I superconductor will therefore either be stationary in the superconducting regions (where the field is zero) or will precess in a field very close to H_c in the normal regions. The probability that a muon experiences either field is equal to the volume fraction of the sample in the respective states and, therefore, a μSR measurement directly measures the superconducting volume fraction of the sample.

μSR has been used to study elemental type-I superconductors such as Sn (IV) [34] and we find qualitatively similar results in BeAu. The most striking indication of type-I behavior in BeAu is that, below T_c, the normal regions of the sample have a relatively constant value of the internal field of $H_c = 258$ Oe, for all applied fields between 50 Oe and 250 Oe. This can be contrasted with the expected internal field behavior of the vortex state of a type-II superconductor, where the internal field distribution in the normal cores falls mostly below the applied field and, in general, changes as a function of the applied field. BeAu joins a relatively small list of nonelemental compounds which show type-I behavior [12,35–42].

Our μSR results call for a more accurate accounting of demagnetizing effects in magnetization measurements to reconcile previous magnetization measurements [30] with the identification of BeAu as a type-I superconductor. To this end, a sample of BeAu is shaped into an ellipsoid so demagnetizing effects can be accounted for more accurately than is typically done in magnetization studies of superconductors. Using this geometry, a demagnetizing factor for the sample can be calculated which allows us to determine the internal field of the normal regions and demonstrate the type-I nature of this compound with magnetization measurements.

Pressure can often have a dramatic effect on superconductivity, especially when the system is near a quantum critical point. Cerium-based noncentrosymmetric superconductors have shown unusual behavior under the application of pressure with a pressure-induced superconducting transition discovered in $CeIrGe_3$, $CeCoGe_3$, and $CeRhSi_3$ [43–45], while $CePt_3Si$ shows a strongly decreasing critical temperature as a function of applied pressure with a complete loss of superconductivity at 1.5 GPa [46]. Iron pnictide superconductors have also shown exotic behavior under the application of pressure [47]. This can be compared to elemental type-I superconductors which typically have a small decrease in T_c with the application of pressure but no exotic behavior is observed [48]. To compare BeAu to these cases, we study the effect of hydrostatic pressure and find that at 450 MPa BeAu still exhibits type-I behavior with a decrease in T_c of 35 mK. This decrease in T_c is similar to the change seen in type-I elemental superconductors such as Sn, In, and Ta under the same conditions [48] and suggests that BeAu is far from a quantum critical point that can be accessed by applying pressure.

II. EXPERIMENTAL METHODS

Polycrystalline samples were synthesized by arc melting from elemental Be (Heraeus, $\geqslant$99.9 wt.%) and Au (Alfa Aesar, $\geqslant$99.95 wt.%) in a 51:49 ratio, with mass loss of less than 0.3%. A small excess of beryllium was added to compensate for the Be loss due to evaporation. After melting, the boule was annealed in an argon atmosphere for 48 hours at 400 °C. A representative sample was measured to have a residual resistivity ratio of 38, which demonstrates the high purity of our samples. Further details can be found in Ref. [30].

Transverse field (TF) muon spin rotation and relaxation (μSR) measurements were performed on the M15 and M20 beamlines at the TRIUMF Laboratory in Vancouver, Canada. A spectrometer incorporating a dilution refrigerator was used on the M15 beamline, which allows for measurements in the temperature range of 0.025–10 K. The experimental setup makes use of a superconducting magnet to allow for fields up to 5 T. Samples were mounted on a silver cold finger to ensure good thermal conductivity and to give a well-defined μSR background signal with minimal relaxation. The instrument has a time resolution of 0.4 ns. The field was applied parallel to the direction of the muon beam and measurements were taken with the initial muon spin direction perpendicular to the field (TF). Several approximately elliptical discs of BeAu, each 0.5 mm thick and roughly 2.75 mm x 3.75 mm, were mounted on the cold finger such that a large fraction of the muon beam spot was covered. The direction of the applied field was perpendicular to the flat faces of the samples. Copper coil electromagnets were used to compensate for any stray fields. The LAMPF spectrometer was used on the M20 beamline, which allows measurements in the temperature range from 2–300 K in an applied field up to 0.4 T. A silver cold finger is not required on LAMPF and the background signal is greatly reduced. Thin, aluminum-backed mylar was used to mount a mosaic of BeAu discs to a copper square cutout. The experiment on M20 was performed using a similar TF setup as on M15. The μSRfit software package was used to analyze the μSR data [49].

Magnetometry measurements were taken at McMaster University using a Quantum Design XL-5 MPMS, which allows for measurements from 1.8 K to 300 K. We used a GC10/3 helium gas pressure cell from the Institute of High Pressure Physics, Polish Academy of Sciences, inserted into the MPMS to allow for magnetometry measurements under pressure up to 700 MPa, above 2 K. A 102.5 mg, nearly ellipsoidal sample with $a = b = 2.75$ mm and $c = 1.90$ mm was produced through grinding with a spherically concave, diamond Dremel head in a fume hood while submerged in mineral oil. A small section on either side of the c axis is flat due to the constraint of grinding while submerged in mineral oil to avoid the dispersal of toxic Be/BeO dust. The sample was measured in the MPMS at ambient pressure after which it needed to be ground down (under the same conditions) to

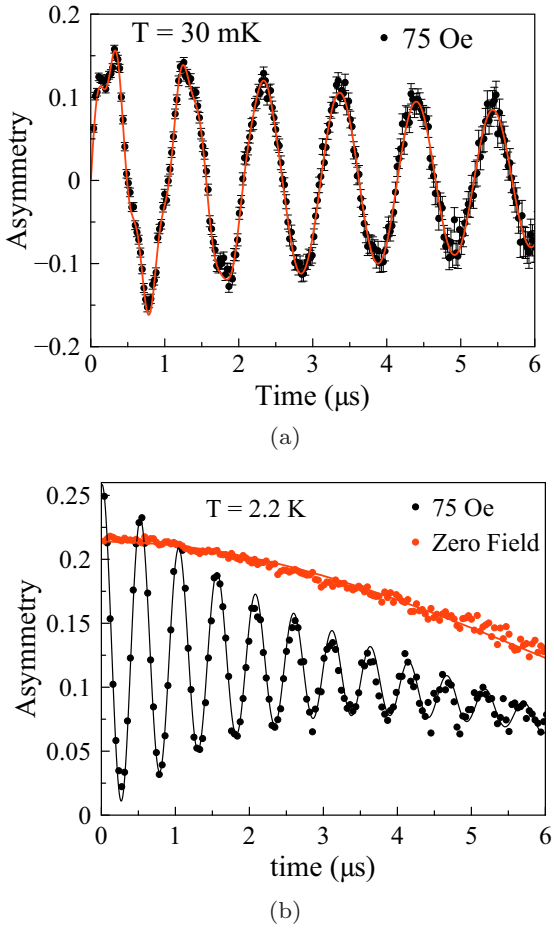

FIG. 1. (a) BeAu μ SR Asymmetry at 30 mK on the M15 beamline in an applied transverse field of 75 G showing two oscillating components, one from the sample and one from the sample holder. (b) μSR Asymmetry at 2.2 K on the M20 beamline in an applied transverse field of 75 G (black) and zero field (red). The nonoscillating component of the 75 G data relaxes with the same rate as the zero field data, showing that there are regions in the sample which are superconducting.

$a = b = 2.69$ mm and $c = 1.86$ mm to fit inside the 3-mm-diameter pressure cell.

III. RESULTS AND DISCUSSION

Figure 1(a) shows the TF μSR asymmetry spectrum at 30 mK on the M15 beamline while Fig. 1(b) shows the asymmetry spectrum on M20 at 2.2 K (black circles), both after field cooling in an applied field of 75 G. All μSR data presented is field cooled (FC). The M15 data show large oscillations as expected for muons precessing in the applied TF with additional contributions coming from a fraction of muons precessing in a different field. This is due to a significant fraction of muons stopping in the silver cold finger and precessing in the applied magnetic field while another fraction of muons stop in the sample and precess in the local field of the sample. The M15 data show a reduced initial asymmetry, A_0, while in a superconducting state due to there being no detectors in the direction of the initial muon polarization when using the TF geometry on M15. Muons landing in the superconducting regions of the sample will not precess and their decay products, which tend to travel in the direction of the muon spin polarization, will be less likely to be detected. This reduces A_0 in the intermediate state of a type-I superconductor compared to the normal state. By comparing the initial asymmetry in the intermediate state and in the normal state, the superconducting volume fraction can be determined. In the intermediate state of a type-I superconductor, the μSR asymmetry measures the total fraction of the signal coming from the sample, F, as well as from superconducting regions in the sample, F_S, and the asymmetry spectrum on the M15 beamline may be fit to

$$A(t) = A_0\{F(1-F_S)\cos(\gamma_\mu H_N + \phi)\exp\left(-\tfrac{1}{2}(\sigma_N t)^2\right) + (1-F)\cos(\gamma_\mu H_{\rm bkg} + \phi)\exp(-\lambda_{\rm bkg} t)\}, \quad (1)$$

where A_0 is the initial asymmetry, H_N the internal field in the normal regions of the sample, $H_{\rm bkg}$ the background field seen by muons stopping outside of the sample, ϕ the phase shift in the μSR asymmetry, σ_N the relaxation rate of the normal regions of the sample, and $\sigma_{\rm bkg}$ the relaxation rate of muons stopping outside of the sample. As μSR samples the entire volume of the material, the fraction of the signal coming from normal/superconducting regions is equivalent to the volume fraction of the sample in the normal/superconducting state. To determine A_0 and to account for extrinsic effects, high temperature (above T_c) data was taken for each applied field and fits to Eq. (1) were performed after fixing $F_S = 0$. The missing asymmetry when comparing low temperature and high temperature measurements allows F_S to be determined on the M15 beamline. A fit to Eq. (1) at 30 mK and 75 G is given by the solid line in Fig. 1(a).

LAMPF on M20 has detectors in the direction of the initial muon polarization and the 75 Oe data [Fig. 1(b)] shows a large fraction of the signal is very slowly relaxing, which is expected if a large fraction of the signal is coming from superconducting regions with zero field. The relaxation rate of this nonoscillating component is equal to the relaxation rate of measurements performed in zero applied field and so this component may be identified with regions of the sample that are superconducting. The visual difference in relaxation rate between the 75 G and zero field measurements in Fig. 1(b) is due to the different initial asymmetries of the two types of measurements. The oscillating component of the signal comes from normal regions of the superconductor that are experiencing a nonzero field. There is very little background signal on M20 and the M20 asymmetry may be fit to

$$A(t) = A_0\{(1-F_S)\cos(\gamma_\mu H_N + \phi)\exp(-\lambda_N t) + F_S\left(\tfrac{1}{3} + \tfrac{2}{3}(1-(\sigma_S t)^2)\exp\left(-\tfrac{1}{2}(\sigma_S t)^2\right)\right)\}, \quad (2)$$

where A_0 is the initial asymmetry, F_S is the superconducting volume fraction, H_N and λ_N are the internal field and relaxation in the normal regions of the sample, ϕ the phase shift of the normal regions, and σ_S the relaxation rate of the superconducting regions of the sample. A fit to Eq. (2) at 2.2 K and 75 G is given by the solid line in Fig. 1. The relaxation rate, σ_S, is consistent with the zero applied field relaxation rate of 0.115 ± 0.002 μs^{-1} for all applied fields, demonstrating that these regions have zero internal field and

are truly superconducting. To determine the expected behavior of the internal field and superconducting volume fraction, a discussion of type-I superconductors is required.

For applied fields, H_a above $(1-N)\,H_c$, where N is the demagnetization factor of the sample, demagnetizing fields cause regions of the surface of a type-I superconductor to experience a field that is larger than the critical field H_c, inevitably causing parts of the sample to enter the normal state. For applied fields $H_c(1-N) \leqslant H_a \leqslant H_c$ a type-I superconductor will have a complicated structure of coexisting superconducting and normal regions known as the intermediate state. Just above approximately $(1-N)H_c$, it can be shown that equilibrium between the superconducting and normal phases can only be achieved if the normal regions have an internal magnetic field of H_c [31,32,50,51]. The field changes from 0 in the superconducting state to H_c over a distance $\delta \approx \xi - \lambda_L$, where ξ is the coherence length and λ_L the London penetration depth, which requires energy. There is also a surface energy associated with maintaining the normal regions at H_c in an applied field of H_a. As the applied field increases, more normal regions are generated, increasing the energy requirements of both affects that slightly reduces the thermodynamic critical field from H_c to the intermediate critical field H_{cI}. In the case of a thin plate oriented perpendicular to H_a, under the assumption of a laminar domain structure of normal and superconducting regions, H_{cI} is approximated by

$$H_{cI} \approx H_c\left[1 - 2\theta\left(\frac{\delta}{d}\right)^{1/2}\right], \quad \theta = \sqrt{\frac{\ln 2}{\pi}}, \tag{3}$$

where d is the plate thickness, δ the thickness of the interface between superconducting and normal regions, and θ is a numerical constant which depends on the assumed domain structure of the superconducting-normal regions as well as the geometry of the sample [31–33]. Similar effects will also slightly raise the Meissner to intermediate state transition field from $(1-N)H_c$ [33].

To complicate matters more, the structure of superconducting-normal domains which minimizes the free energy changes as a function of H_a. At applied fields just above $\approx H_{cI}(1-N)$ the free energy is minimized by having tubular-threadlike normal regions pierce the superconductor, while at intermediate fields the free energy is minimized by having corrugated laminae of superconducting and normal layers. Finally, at fields close to H_{cI}, tubular-threadlike superconducting regions pierce normal metal [31–33,50,52]. This behavior has been observed before [53–55], but the exact behavior of a material in the intermediate state is hard to predict *a priori* as it has been shown that the free-energy differences of various spatial configurations of the intermediate state are quite small. Observationally, the spatial configuration selection depends upon the exact experimental conditions, as well as sample quality [32,50,55].

The internal field in the normal regions of a type-I superconductor remain relatively constant at H_c until an applied field comparable with H_c is reached. A TF μSR experiment on a type-I superconductor, in an applied field above $H_c(1-N)$ and sufficiently far below H_c, will therefore show muons in the normal regions of the sample precessing with a frequency distribution centered around $\omega = \gamma_\mu H_c$ where $\frac{\gamma_\mu}{2\pi} =$ 135 MHz/T is the gyromagnetic ratio of the muon [56]. This can be contrasted with the expected results of a TF μSR experiment on a type-II superconductor in the vortex state where muons will precess at a frequency $\omega = \gamma_\mu H_{\rm int}$ where $H_{\rm int}$ is an asymmetric distribution, the peak of which falls below H_a [56]. It should also be noted that while a type-I superconductor in the intermediate state will have an approximately constant internal field with $H_{\rm int} \approx H_c$ or $H_{\rm int} = 0$ (normal versus superconducting regions) for all applied fields in the range $H_c(1-N) \leqslant H_a \leqslant H_c$, the peak position and shape of the $H_{\rm int}$ distribution for a type-II superconductor in the vortex state will generally depend upon H_a.

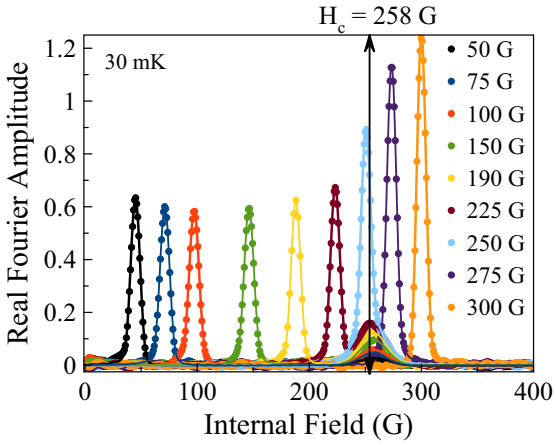

FIG. 2. The Fourier transform of the M15 μSR Asymmetry for a variety of fields at 30 mK. The sharp peaks in the data as well as color indicate the applied field experienced by muons stopping in the silver cold finger. The broad peak centered around 258 Oe for all applied fields below $H_a = 260$ Oe unambiguously shows BeAu to be a type-I superconductor.

The Fourier transform of the μSR spectra gives the probability distribution of $H_{\rm int}$ in both the intermediate state of a type-I superconductor and the vortex state of a type-II superconductor. The probability distribution for both types of superconductors will show a sharp background peak at H_a on the M15 beamline from muons stopping in the silver cold finger but the internal field in a type-I superconductor will not change as a function of applied field. A type-II superconductor, however, will have a varying internal field. The short, broad peak centered at 258 Oe for all applied fields $H_a \leqslant 260$ G in Fig. 2 unambiguously demonstrates that BeAu is a type-I superconductor with $H_c \approx 258$ Oe.

The results from fitting the 30 mK data at various applied magnetic fields in the time domain are shown in Fig. 3. The superconducting volume fraction of the sample in the intermediate state of a type-I superconductor should decrease from 100% near $(1-N)H_c$ approximately linearly, for low applied fields [32]. As the applied field increases and approaches H_{cI}, the superconducting volume fraction picks up a small correction given by Eq. (2.28) of Ref. [32]. The superconducting volume fraction for BeAu given in Fig. 3(a) shows qualitatively similar behavior to Ref. [34] and follows the expected linear behavior for fields not too close to H_c [31,32]. Figure 3(b) shows that the internal field in the normal regions of the sample is nearly constant as a function of

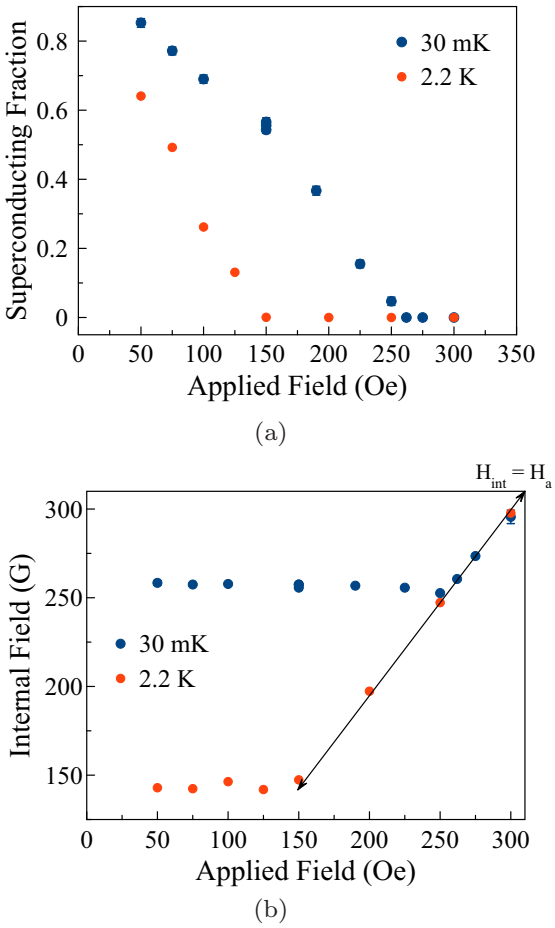

FIG. 3. (a) The superconducting volume fraction of the sample as a function of applied field at 30 mK after field cooling on M15 (blue) and 2.2 K on M20 (red). The superconducting volume fraction increases as the field decreases, as is expected for a type-I superconductor in the intermediate state. Where not shown, uncertainties are smaller than marker size. (b) The internal field in the normal regions of the sample as a function of applied field at 30 mK after field cooling on M15 (blue) and 2.2 K on M20 (red). The data shows the normal regions have an approximately constant internal field while in the intermediate state. For applied fields above H_{cI}, $H_{\rm int} = H_a$, indicating the sample is in the normal state.

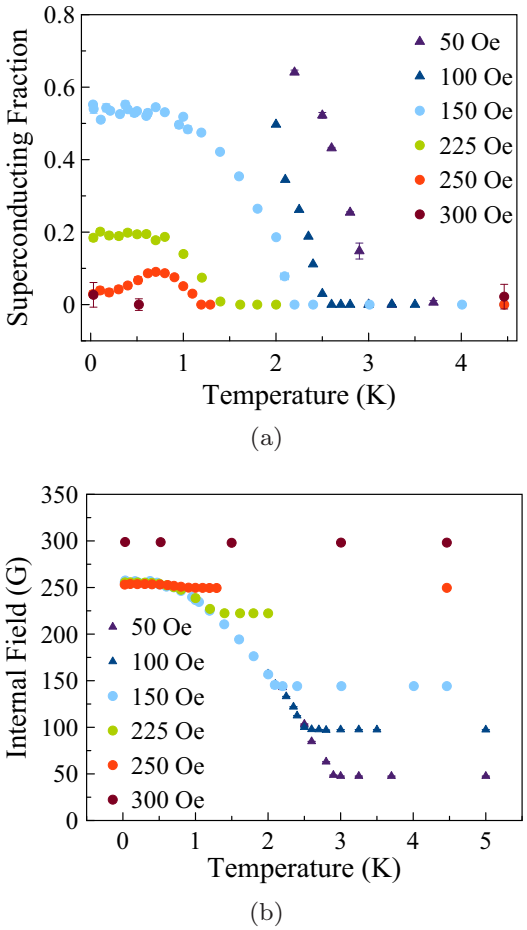

FIG. 4. (a) Superconducting volume fraction as a function of temperature. Data was taken after field cooling to base and measured upon heating to the specified temperature. Triangles indicate data was taken on M20 while circles indicate data was taken on M15. The superconducting volume fraction increases as the temperature decreases for fields below H_{cI}, as is expected for a type-I superconductor in the intermediate state. Uncertainties are smaller than marker size where not shown. (b) The internal field in the normal regions of the sample as a function of temperature. For an applied field below $H_{cI}(T)$, the internal field is equal to approximately $H_c(T)$ and μSR is able to measure $H_c(T)$ while in the intermediate state. For applied fields above $H_c(T)$, the sample is in the normal state and the internal field is equal to the applied field.

H_a until $H_a \approx H_{cI}$ is reached. Figure 3(b) also demonstrates that the thermodynamic critical field at 30 mK is slightly decreased from $H_c \approx 258 \pm 1$ Oe in an applied field of 50 Oe to $H_{cI} \approx 252.6 \pm 0.4$ Oe in an applied field of 250 Oe, in qualitative agreement with Eq. (3) and the expected behavior from Ref. [32]. The variation in internal field is due to the contribution of the interface energy between normal and superconducting regions as well as the interface energy between normal regions and regions outside the sample as a significant fraction of the sample enters the normal state [31–33,50,52].

Our 30 mK data show that BeAu is in the intermediate state from 50–250 Oe with some variability in internal field due to interface energy between normal and superconducting regions. The transition to the normal state above ≈250 Oe is indicated in Fig. 3(a) and indirectly shown in Fig. 3(b) where $H_{\rm int} = H_a$ above 250 Oe. An approximate demagnetization factor of the measured discs is taken from a table [57] and gives $N = 0.82$. Using $H_{M-I} \approx H_{cI}(1 - N)$ shows the Meissner state is expected for H_a less than ≈46 Oe. As we did not measure below 50 Oe, a pure Meissner state is not seen in our M15 data.

The μSR asymmetry of BeAu was also studied as a function of temperature for the applied fields 50 G, 100 G, 150 G, 225 G, 250 G, 300 G, and results are shown in Fig. 4. The fraction of the sample in the Meissner state generally increases as temperature decreases [Fig. 4(a)], as is expected in a type-I superconductor. The exception to this is the 250 G data set which peaks near 0.7 K, however, the applied field is close enough to $H_c(T = 0)$ that the superconducting-normal domain structure may change as a function of temperature, altering the relative size of the normal and superconducting volumes. The internal field in the normal regions as a function

of temperature is shown in Fig. 4(b) and demonstrates that the μSR technique can be used to trace out a partial H versus T phase diagram for type-I superconductors while in the intermediate state, i.e., when $H_{cI}(1-N) \leqslant H_a \leqslant H_{cI}$.

Our μSR results unambiguously show that BeAu is a type-I superconductor, motivating a new careful study of the magnetization properties of BeAu using a well-defined sample geometry so that demagnetizing effects can be accounted for more accurately than is typically done in studies of superconductors. For a type-I superconductor of an ellipsoidal shape, the field at the surface of the equator of the sample, $H_{\rm eq}$, when measuring in an applied field perpendicular to this equator, is given by

$$H_{\rm eq} = H_a - 4\pi NM, \tag{4}$$

where N is the demagnetizing factor and M the magnetization of the sample [31,32,50]. An ellipsoid of revolution is one of the few shapes for which the demagnetization factor can be calculated analytically, which is why we produced a sample with this geometry [57,58]. The surface field at the equator of a superconducting ellipsoid is the maximum field that the sample experiences and is given by

$$H_{\rm eq} = \frac{H_a}{1-N} [31, 32]. \tag{5}$$

$H_{\rm eq}$ is an important quantity because, while in the intermediate state, the internal field is equal to the surface field on the equator of the superconductor. As this is the region with the highest local field, when the sample enters the normal state the equator should be the first region to do so. By using the fact that $H_{\rm eq} = H_c$ while in the intermediate state, we should be able to reconstruct the discontinuous magnetization behavior expected at H_c for a type-I superconductor. An ellipsoidal type-I superconductor will be in the Meissner state below $H_a \approx (1-N)H_{cI}$, above which it will enter the intermediate state [31,32]. Figure 5(a) shows the magnetization as a function of applied field for temperatures from 0.5 K to 3.2 K. Measurements were taken from 0 G to a maximum field, followed by measurements from the maximum field to 0 G. Fields are accurate to 0.1 G. Figure 5(a) shows linear behavior at low fields while in the Meissner state, with a departure from linearity as the minima is approached. The behavior is well described by a type-I superconductor entering the intermediate state near the magnetization minima followed by a transition to the normal state at high fields. The departure from linearity as the minima is approached is due to the generation of normal regions and the restructuring of normal-superconducting domains as the sample enters the intermediate state [33,52].

$H_{\rm eq}$ has very different behaviors for type-I superconductors in the intermediate state and type-II superconductors in the vortex state. In the intermediate state, the superconducting volume fraction of the sample decreases approximately linearly for a wide range of applied fields while the microscopic magnetization does not change. The linear decrease in the superconducting volume makes the overall magnitude of the magnetization of the entire sample decrease linearly. H_{eq} therefore remains constant, equal to internal field while in the intermediate state of a type-I superconductor.

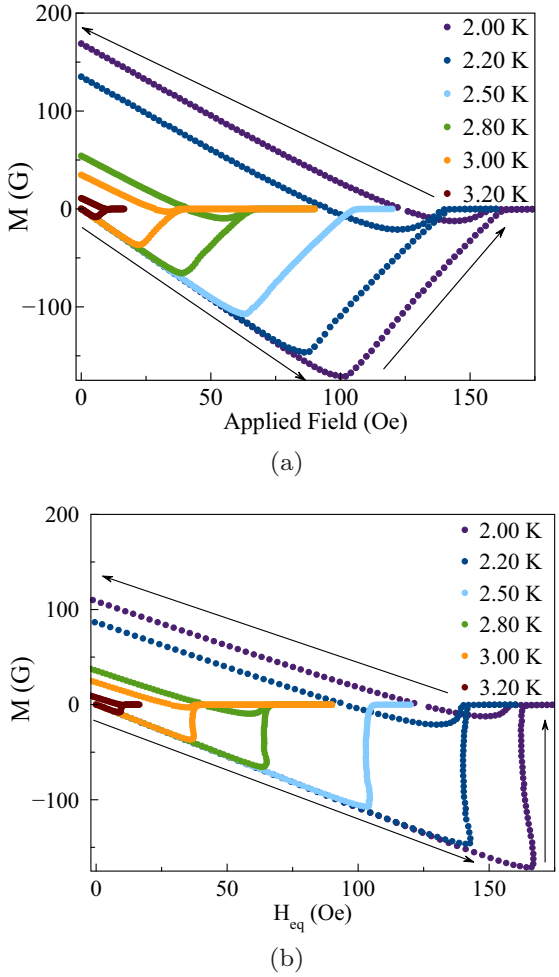

FIG. 5. (a) Magnetization as a function of applied field from 2.0 K to 3.2 K. Measurements were taken in increasing field followed by measurements in decreasing field once $H_{\rm eq} > H_{cI}$ was reached. (b) Magnetisation as a function of the field at the equator $H_{\rm eq} = H_a - 4\pi NM$. This plot shows the expected discontinuous transition in magnetization for a type-I superconductor.

A demagnetizing factor of $N_{\rm ellipsoid} = 0.4355$ was calculated using Eq. (34) of Ref. [58], assuming the sample was a perfect ellipsoid with major-axis $a = b = 2.75$ mm and minor-axis $c = 1.90$ mm. The sample is not a perfect ellipsoid and a demagnetizing factor of $N_{\rm sample} = 0.3755$ was found by optimizing the discontinuous transition of the magnetization in Fig. 5(b), such that the transition occurred over the smallest $H_{\rm eq}$ range. A high-quality sample of a type-I superconducting material should exhibit a crisp transition at H_{cI}. The high-quality nature of our sample [30], along with our μSR measurements showing type-I behavior, justify this optimization procedure for the demagnetization factor. Figure 5(b) shows the magnetization decreases linearly with a slope corresponding to $\chi = -1$ while in the Meissner state. Upon entering the intermediate state the magnetization as a function of $H_{\rm eq}$ is nearly vertical as is expected in a type-I superconductor [31,32]. The change in $H_{\rm eq}$ as the magnitude of the magnetization decreases is due to the thermodynamic critical field being modified from H_c at low field to H_{cI} at fields just below H_{cI}.

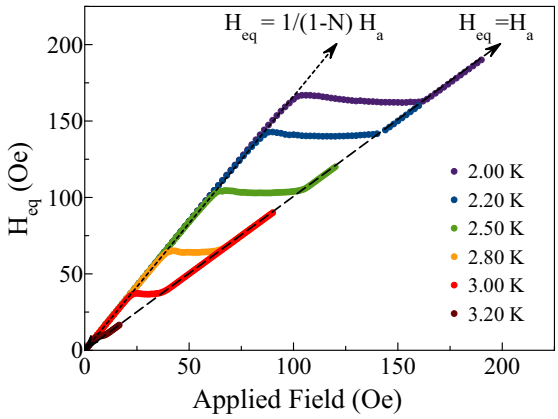

FIG. 6. Internal field at the equator as a function of applied field. In the Meissner state, $H_{\rm eq} = \frac{1}{1-N} H_a$ and the transition to the intermediatestate can be identified for applied fields where $H_{\rm eq}$ becomes approximately constant with $H_{cI} \leqslant H_{\rm eq} \leqslant H_c$. In the normal state, $H_{\rm eq} = H_a$.

Figure 6 shows the field at the equator, $H_{\rm eq}$, of the sample as a function of applied field. This plot matches the expected behavior of $H_{\rm eq}$ for a superconducting ellipsoid given by Refs. [31,32], where there is a linear increase in $H_{\rm eq}$, while in the Meissner state with $H_{\rm eq} = \frac{H_a}{1-N}$ as H_a is increased to $(1-N)\ H_{cI}$. In the intermediate state, $H_{\rm eq}$ stays relatively constant with some modification due to the thermodynamic critical field changing from H_c at low fields to H_{cI} near H_{cI}. Above H_{cI}, $H_{\rm eq}$ increases linearly with $H_{\rm eq} = H_a$.

The magnetic susceptibility in applied fields from 10–110 Oe was also measured as a function of temperature using the demagnetization factor found from our previous measurements and is shown in Fig. 7(a). The zero-field cooled (ZFC) measurements (closed circles) show a full magnetic flux expulsion with χ approaching (just below) -1 as T approaches zero, while the FC data (open circles) indicate there is some field being maintained in the sample. Small overlap regions in the intermediate state can be seen where the ZFC and FC results agree. $H_{\rm eq}$ as a function of temperature is shown in Fig. 7(b) again showing small regions of agreement between ZFC and FC. In these small regions of reversibility, H_{cI} can be mapped out as a function of temperature as shown in Fig. 7(c), which can be fit to the Ginzburg-Landau relation,

$$H_c(T) = H_c(0)\left(1 - \left(\frac{T}{T_c}\right)^2\right), \qquad (6)$$

[31,32], yielding $H_c(0) = 252 \pm 2$ Oe and $T_c = 3.249 \pm 0.004$ K.

Combining the results of our μSR measurements (triangles), magnetization versus applied field (black circles) and magnetic susceptibility versus temperature (blue open circles) yields the phase diagram shown in Fig. 8. Overlap regions between μSR and magnetization measurements show good agreement. A fit to Eq. (6) shows good agreement with the experimental data above approximately 0.5 K, with $H_c = 258.5 \pm 0.5$ Oe and $T_c = 3.234 \pm 0.003$ K. The low temperature μSR data shows a slightly flatter than quadratic behavior at low temperature.

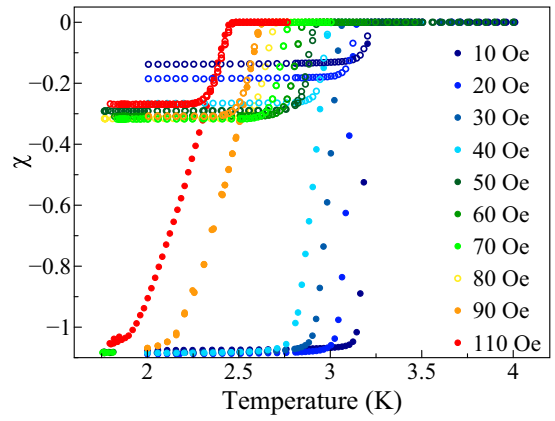

(a)

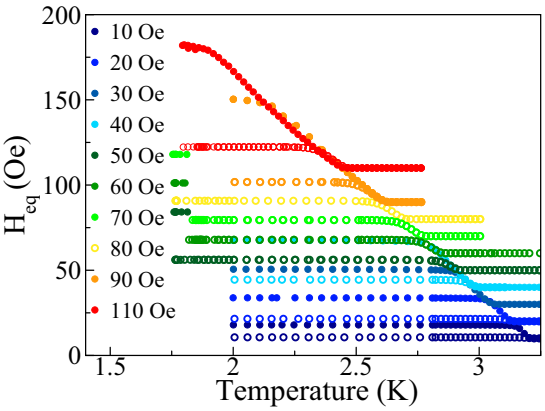

(b)

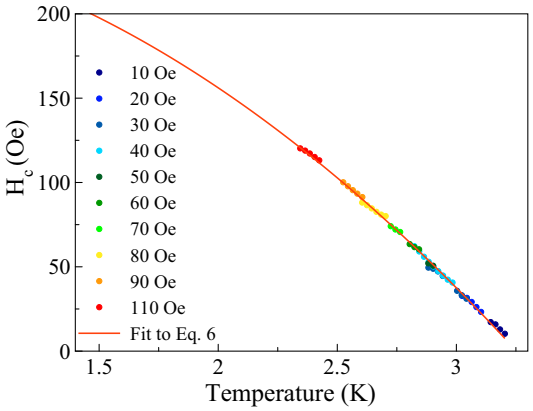

(c)

FIG. 7. (a) Magnetic susceptibility as a function of temperature for applied fields from 10–110 Oe. Zero field cooled (ZFC) (closed circles) and field cooled (FC) (open circle) data show small overlap regions. (b) Equatorial field as a function of temperature for applied fields from 10–110 Oe. ZFC (closed circles) and FC (open circles) show there are small overlap regions. (c) $H_c(T)$ may be mapped out by using data points where the ZFC and FC regions overlap and is fit to Eq. (6), yielding $H_c = 252 \pm 2$ Oe and $T_c = 3.249 \pm 0.004$ K.

The effect of pressure on the system was explored using a pressure cell inserted into the MPMS. Figure 9 shows the results of our magnetization measurements for ambient pressure ($\approx$10 kPa, blue circles) and 450 MPa (red circles) as well as fits to the ambient pressure (blue line) and 450 MPa (red

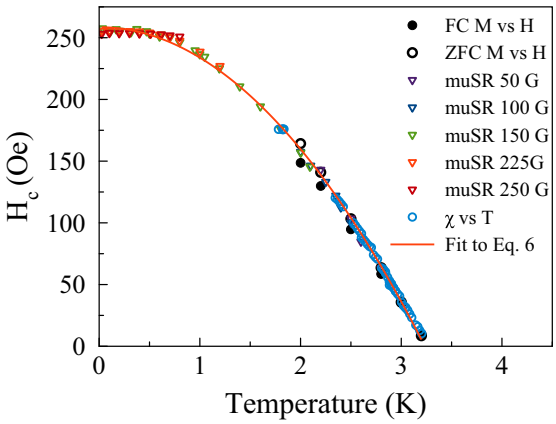

FIG. 8. The field versus temperature phase diagram combining together our μSR (open triangles), magnetization (black circles) and magnetic susceptibility (blue open circles) measurements. A fit to Eq. (6) over the full temperature range and all data sets gives $H_c = 258.6 \pm 0.5$ Oe and $T_c = 3.234 \pm 0.003$ K.

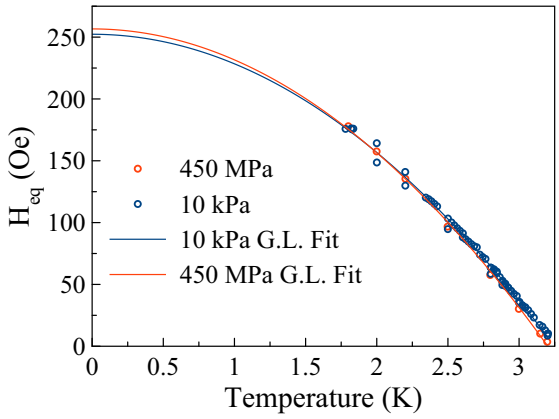

FIG. 9. The magnetic field versus temperature phase diagram from our magnetometry data at 10 kPa (blue circles) and 450 MPa (red circles). A fit to Eq. (6) to the data yields $H_c = 252 \pm 2$ Oe (257 ± 3 Oe) and $T_c = 3.234 \pm 0.004$ K (3.20 ± 0.01 K) for the 10 kPa (450 MPa) data.

line) data. Using Eq. (6), the magnetization measurements at 450 MPa give $H_c = 257 \pm 3$ Oe and $T_c = 3.20 \pm 0.01$ K, while the 10 kPa data gives $H_c = 252 \pm 2$ Oe and $T_c = 3.234 \pm 0.004$ K; a change in T_c of 34 ± 11 mK. Magnetization measurements cannot be performed in low enough temperature to determine if the difference in $H_c(0)$ of 5 ± 4 Oe from a fit to Eq. (6) between the 450 MPa data and ambient pressure data is real. The change in T_c is comparable to the change observed in the elemental type-I superconductors tin (IV), indium, and tantalum which have a decrease in T_c of about 20 mK under the same conditions [48]. This suggests that BeAu is far from a quantum critical point accessible by application of pressure.

IV. CONCLUSION

μSR and demagnetization corrected magnetization measurements were carried out on discs and an ellipsoid of polycrystalline BeAu. Our results show that BeAu is a type-I superconductor with $H_c \approx 258$ Oe and $T_c \approx 3.25$ K. The μSR and magnetization results show consistent values of $H_c(T)$ in the regions where they overlap. A Ginzburg-Landau fit [Eq. (6)] over the entire temperature range and all data sets give $H_c = 258.6 \pm 0.5$ Oe and $T_c = 3.234 \pm 0.003$ K. Magnetization measurements on an ellipsoid were taken in a pressure chamber at 450 MPa. Fitting only the magnetization data to Eq. (6) yields $H_c = 257 \pm 3$ Oe and $T_c = 3.20 \pm 0.01$ K for the 450 MPa data and H_c 252 ± 2 Oe and T_c 3.234 ± 0.004 K for the 10 kPa pressure data. The reduction in T_c under 450 MPa of pressure in BeAu is comparable to the decrease in T_c observed in the elemental type-I superconductors tin (IV), indium, and tantalum under the same conditions [48]. This suggests that BeAu is far from a quantum critical point accessible by the application of pressure.

Note added. Recently, we became aware of Ref. [59], which reports similar results on BeAu.

ACKNOWLEDGMENTS

We thank G. D. Morris, B. S. Hitti, and D. J. Arseneau for their assistance with the μSR measurements. We thank Paul Dube for their assistance with the magnetometry measurements at McMaster. Work at McMaster University was supported by the Natural Sciences and Engineering Research Council of Canada and the Canadian Foundation for Innovation. E.S. greatly appreciates the support provided by the Fulbright Canada Research Chair Award.

[1] E. Bauer and M. Sigrist, *Noncentrosymmetric Superconductors: Introduction and Overview* (Springer, Berlin, 2012).

[2] N. Hayashi, K. Wakabayashi, P. A. Frigeri, and M. Sigrist, Phys. Rev. B **73**, 024504 (2006).

[3] M. Sigrist, D. F. Agterberg, P. A. Frigeri, N. Hayashi, R. P. Kaur, A. Koga, I. Milat, K. Wakabayashi, and Y. Yanase, J. Magn. Magn. Mater. **310**, 536 (2007).

[4] T. Takimoto and P. Thalmeier, J. Phys. Soc. Jpn. **78**, 103703 (2009).

[5] I. Bonalde, W. Brämer-Escamilla, and E. Bauer, Phys. Rev. Lett. **94**, 207002 (2005).

[6] H. Mukuda, T. Fujii, T. Ohara, A. Harada, M. Yashima, Y. Kitaoka, Y. Okuda, R. Settai, and Y. Onuki, Phys. Rev. Lett. **100**, 107003 (2008).

[7] I. Bonalde, R. L. Ribeiro, W. Brämer-Escamilla, G. Mu, and H. H. Wen, Phys. Rev. B **79**, 052506 (2009).

[8] E. Bauer, G. Rogl, X.-Q. Chen, R. T. Khan, H. Michor, G. Hilscher, E. Royanian, K. Kumagai, D. Z. Li, Y. Y. Li, R. Podloucky, and P. Rogl, Phys. Rev. B **82**, 064511 (2010).

[9] M. Nishiyama, Y. Inada, and G.-q. Zheng, Phys. Rev. Lett. **98**, 047002 (2007).

[10] H. Q. Yuan, D. F. Agterberg, N. Hayashi, P. Badica, D. Vandervelde, K. Togano, M. Sigrist, and M. B. Salamon, Phys. Rev. Lett. **97**, 017006 (2006).

[11] M. Isobe, M. Arai, and N. Shirakawa, Phys. Rev. B **93**, 054519 (2016).

[12] V. K. Anand, A. D. Hillier, D. T. Adroja, A. M. Strydom, H. Michor, K. A. McEwen, and B. D. Rainford, Phys. Rev. B **83**, 064522 (2011).

[13] J. A. T. Barker, D. Singh, A. Thamizhavel, A. D. Hillier, M. R. Lees, G. Balakrishnan, D. M. Paul, and R. P. Singh, Phys. Rev. Lett. **115**, 267001 (2015).

[14] A. D. Hillier, J. Quintanilla, and R. Cywinski, Phys. Rev. Lett. **102**, 117007 (2009).

[15] Y. Iwamoto, Y. Iwasaki, K. Ueda, and T. Kohara, Phys. Lett. A **250**, 439 (1998).

[16] K. Sugawara, T. Sato, S. Souma, T. Takahashi, and A. Ochiai, Phys. Rev. B **76**, 132512 (2007).

[17] K. V. Samokhin and V. P. Mineev, Phys. Rev. B **77**, 104520 (2008).

[18] M. A. Khan, A. B. Karki, T. Samanta, D. Browne, S. Stadler, I. Vekhter, A. Pandey, P. W. Adams, D. P. Young, S. Teknowijoyo, K. Cho, R. Prozorov, and D. E. Graf, Phys. Rev. B **94**, 144515 (2016).

[19] D. Singh, A. D. Hillier, A. Thamizhavel, and R. P. Singh, Phys. Rev. B **94**, 054515 (2016).

[20] D. Singh, S. K. P., J. A. T. Barker, D. M. Paul, A. D. Hillier, and R. P. Singh, Phys. Rev. B **97**, 100505 (2018).

[21] P. K. Biswas, H. Luetkens, T. Neupert, T. Stürzer, C. Baines, G. Pascua, A. P. Schnyder, M. H. Fischer, J. Goryo, M. R. Lees, H. Maeter, F. Brückner, H.-H. Klauss, M. Nicklas, P. J. Baker, A. D. Hillier, M. Sigrist, A. Amato, and D. Johrendt, Phys. Rev. B **87**, 180503 (2013).

[22] G. M. Luke, Y. Fudamoto, K. M. Kojima, M. I. Larkin, J. Merrin, B. Nachumi, Y. J. Uemura, Y. Maeno, Z. Q. Mao, Y. Mori, H. Nakamura, and M. Sigrist, Nature **394**, 558 (1998).

[23] J. Xia, Y. Maeno, P. T. Beyersdorf, M. M. Fejer, and A. Kapitulnik, Phys. Rev. Lett. **97**, 167002 (2006).

[24] G. M. Luke, A. Keren, L. P. Le, W. D. Wu, Y. J. Uemura, D. A. Bonn, L. Taillefer, and J. D. Garrett, Phys. Rev. Lett. **71**, 1466 (1993).

[25] P. de Réotier, A. Huxley, A. Yaouanc, J. Flouquet, P. Bonville, P. Imbert, P. Pari, P. Gubbens, and A. Mulders, Phys. Lett. A **205**, 239 (1995).

[26] Y. Aoki, A. Tsuchiya, T. Kanayama, S. R. Saha, H. Sugawara, H. Sato, W. Higemoto, A. Koda, K. Ohishi, K. Nishiyama, and R. Kadono, Phys. Rev. Lett. **91**, 067003 (2003).

[27] Y. Aoki, T. Tayama, T. Sakakibara, K. Kuwahara, K. Iwasa, M. Kohgi, W. Higemoto, D. E. MacLaughlin, H. Sugawara, and H. Sato, J. Phys. Soc. Jpn. **76**, 051006 (2007).

[28] V. G. Yarzhemsky and V. I. Nefedov, Phys. Solid State **51**, 448 (2009).

[29] A. Bhattacharyya, D. Adroja, N. Kase, A. Hillier, J. Akimitsu, and A. Strydom, Sci. Rep. **5**, 12926 (2015).

[30] A. Amon, E. Svanidze, R. Cardoso-Gil, M. N. Wilson, H. Rosner, M. Bobnar, W. Schnelle, J. W. Lynn, R. Gumeniuk, C. Hennig, G. M. Luke, H. Borrmann, A. Leithe-Jasper, and Y. Grin, Phys. Rev. B **97**, 014501 (2018).

[31] P.-G. de Gennes, *Superconductivity of Metals and Alloys*, Advanced Book Classics (Advanced Book Program, Perseus Books, Reading, MA, 1999).

[32] M. Tinkham, *Introduction to Superconductivity*, 2nd ed. (McGraw-Hill, New York, 1975).

[33] *Collected Papers of L. D. Landau*, edited by D. T. Haar (Pergamon Press INC, New York, 1965), pp. 365–379.

[34] V. S. Egorov, G. Solt, C. Baines, D. Herlach, and U. Zimmermann, Phys. Rev. B **64**, 024524 (2001).

[35] E. Svanidze and E. Morosan, Phys. Rev. B **85**, 174514 (2012).

[36] A. Yamada, R. Higashinaka, T. D. Matsuda, and Y. Aoki, J. Phys. Soc. Jpn. **87**, 033707 (2018).

[37] J. Bekaert, S. Vercauteren, A. Aperis, L. Komendová, R. Prozorov, B. Partoens, and M. V. Milošević, Phys. Rev. B **94**, 144506 (2016).

[38] M. V. Salis, P. Rodière, H. Leng, Y. K. Huang, and A. de Visser, J. Phys.: Condens. Matter **30**, 505602 (2018).

[39] U. Gottlieb, J. C. Lasjaunias, J. L. Tholence, O. Laborde, O. Thomas, and R. Madar, Phys. Rev. B **45**, 4803 (1992).

[40] M. Kriener, T. Muranaka, J. Kato, Z.-A. Ren, J. Akimitsu, and Y. Maeno, Sci. Technol. Adv. Mater. **9**, 044205 (2008).

[41] M. Smidman, A. D. Hillier, D. T. Adroja, M. R. Lees, V. K. Anand, R. P. Singh, R. I. Smith, D. M. Paul, and G. Balakrishnan, Phys. Rev. B **89**, 094509 (2014).

[42] K. Wakui, S. Akutagawa, N. Kase, K. Kawashima, T. Muranaka, Y. Iwahori, J. Abe, and J. Akimitsu, J. Phys. Soc. Jpn. **78**, 034710 (2009).

[43] F. Honda, I. Bonalde, K. Shimizu, S. Yoshiuchi, Y. Hirose, T. Nakamura, R. Settai, and Y. Ōnuki, Phys. Rev. B **81**, 140507 (2010).

[44] R. Settai, I. Sugitani, Y. Okuda, A. Thamizhavel, M. Nakashima, Y. Ōnuki, and H. Harima, J. Magn. Magn. Mater. **310**, 844 (2007).

[45] N. Kimura, K. Ito, K. Saitoh, Y. Umeda, H. Aoki, and T. Terashima, Phys. Rev. Lett. **95**, 247004 (2005).

[46] T. Yasuda, H. Shishido, T. Ueda, S. Hashimoto, R. Settai, T. Takeuchi, T. D Matsuda, Y. Haga, and Y. Nuki, J. Phys. Soc. Jpn. **73**, 1657 (2004).

[47] Y. Mizuguchi, F. Tomioka, S. Tsuda, T. Yamaguchi, and Y. Takano, Appl. Phys. Lett. **93**, 152505 (2008).

[48] L. D. Jennings and C. A. Swenson, Phys. Rev. **112**, 31 (1958).

[49] A. Suter and B. M. Wojek, Physics Procedia **30**, 69 (2012).

[50] L. D. Landau and E. M. Lifshitz, *Electrodynamics of Continuous Media* (Pergamon Press INC, New York, 1983), p. 460.

[51] E. Andrew, Proc. R. Soc. London A **194**, 98 (1948).

[52] A. Fortini and E. Paumier, Phys. Rev. B **5**, 1850 (1972).

[53] J. D. Livingston, Phys. Rev. **129**, 1943 (1963).

[54] J. D. Livingston, J. Appl. Phys. **34**, 3028 (1963).

[55] R. P. Huebener, *Magnetic Flux Structures in Superconductors* (Springer-Verlag, Berlin, 1979).

[56] J. E. Sonier, J. H. Brewer, and R. F. Kiefl, Rev. Mod. Phys. **72**, 769 (2000).

[57] J. A. Osborn, Phys. Rev. **67**, 351 (1945).

[58] M. Beleggia, M. D. Graef, and Y. Millev, Philos. Mag. **86**, 2451 (2006).

[59] D. Singh, A. D. Hillier, and R. P. Singh, Phys. Rev. B **99**, 134509 (2019).

Appendix A

Josephson Junctions and SQUID Devices

A1 Josephson Junctions

If we consider two superconductors of the same material with separate wave-functions separated by a thin (with respect to the coherence length of the superconductors) insulating barrier we can construct a time-independent Shrödinger equation within the normal region for tunneling of Cooper pairs,

$$\frac{1}{2(2m_e)}\left(\frac{\hbar}{i}\nabla - 2e\vec{A}(r)\right)\psi(r) + 2e\phi(r)\psi(r) + V\psi(r) = 0 \tag{A.1}$$

where m_e and e are the mass and charge of the electron, ϕ(r) and $\vec{A}$(r) represent the electromagnetic field, V is the tunneling potential barrier, and ψ(r) the wavefunction. At each boundary, the wavefunction must be equal to the superconducting wavefunction in the respective superconductor,

$$\psi = \sqrt{n}\exp(i\theta), \tag{A.2}$$

where n is the density of the Cooper pairs and θ the phase. Assuming no electromagnetic field and using the definition of the supercurrent,

$$J_s = \frac{2(2e)}{(2m_e)} Re\left(\psi^\star \frac{\hbar}{i}\nabla\psi\right), \tag{A.3}$$

(emphasis is on the charge and mass of the Cooper pair) leads to [31],

$$J_s = J_c \sin\left(\theta_2 - \theta_1\right), \tag{A.4}$$

where θ_1 and θ_2 are the phases at the respective boundaries. This is known as the DC Josephson effect as it shows there will be a constant supercurrent in the absence of an electromagnetic field. Here J_c is called the critical current which depends upon the superconducting material, weak-link material, and the geometry of the weak link. In the

presence of an electromagnetic field we must consider the gauge-invariant phase,

$$\gamma\left(\vec{r},t\right)=\theta_2-\theta_1-\frac{2\pi}{\Phi_0}\int\vec{A}(r,t)\cdot d\vec{l} \tag{A.5}$$

leading to the relation,

$$J_S\left(\vec{r},t\right)=J_c\sin\left(\gamma\left(\vec{r},t\right)\right). \tag{A.6}$$

From Eq. A.5 it may be shown [31],

$$\frac{\partial\gamma}{\partial t}=\frac{2\pi}{\Phi_0}V(t), \tag{A.7}$$

where V(t) is the voltage applied across the junction. This is known as the AC Josephson effect as it shows a constant voltage produces an alternating supercurrent.

Let us consider the effect of an applied voltage of the form,

$$v(t)=V_0+V_s\cos\left(\omega_s t\right). \tag{A.8}$$

Through the use of a Fourier-Bessel expansion, to first order the supercurrent density is given by,

$$J_s=J_c\ \mathbf{J_0}\left(\frac{2\pi V_s}{\Phi_0}\right)\sin\left(\gamma(0)\right), \tag{A.9}$$

where $\mathbf{J_0}$ is the zeroth order Bessel Function of the first kind [31, 131]. That is, an AC voltage produces a direct current across the junction, to first order. Careful choice of the constant voltage V_0 removes the time dependence of the next higher order term, leading to a roughly constant DC.

We will take a second to examine the case of a ribbon of wire with a rectangular cross section which has a width much larger than both its height as well as the thickness of the Josephson Junction. In this case, it can be shown that the effect of the magnetic field is to make the current density oscillate as the width of the junction is transversed. Integrating Eq. A.4 leads to,

$$I_s=I_c\left|\frac{\sin(\frac{\pi\Phi}{\Phi_0})}{\frac{\pi\Phi}{\Phi_0}}\right|, \tag{A.10}$$

where Φ is the flux through the loop. This is analogous to the interference pattern produced by light shone through a single rectangular slit. We will ignore these geometry effects in the following discussions of the DC and AC Superconducting Quantum Interference Device (SQUID).

The last thing to determine is the voltage produced in a Josephson junction when a bias current is run through the junction. To find this the Resistively and Capacitively Shunted Junction (RSCJ) model is often used [131, 31] where the junction is set up in parallel with a resistor and capacitor. Often a Josephson junction is physically resistively shunted to avoid hysteresis in the I-V curve, while the junction itself will have a small self-capacitance, making this model physically relevant. Using Kirchoff's rules one can

show,

$$I = I_c \sin(\gamma) + C\frac{\partial V}{\partial t} + \frac{V}{R}, \tag{A.11}$$

where R is the resistance and C the capacitance. Inserting Eq. A.7 into the above leads to,

$$I = I_c \sin(\gamma) + \frac{\Phi_0 C}{2\pi}\frac{\partial^2 \gamma}{\partial t^2} + \frac{\Phi_0}{2\pi R}\frac{\partial \gamma}{\partial t}, \tag{A.12}$$

which when C = 0 has solution,

$$V = \frac{1}{R}\sqrt{I^2 - I_c^2}, I > I_c \tag{A.13}$$

and $V = 0$ when I is less than I_c. The result is qualitatively similar for $\frac{I_c R^2 C}{\Phi_0} \leq 1$. We can now examine how Josephson junctions are used in SQUID devices.

A2 DC SQUID

In a DC SQUID a bias current, I, is applied through the loop and a circulating current, J, is caused by the flux from the sample. Using the RSCJ model with equations A.7 and A.11 we can see that the current in each junction is given by,

$$\frac{I}{2} \pm J = I_c \sin(\gamma_i) + \frac{\Phi_0}{2\pi R}\frac{\partial \gamma_i}{\partial t} + \frac{\Phi_0\ C}{2\pi}\frac{\partial^2 \gamma_i}{\partial^2 t}, \tag{A.14}$$

for junctions 1 (+) and 2 (-). It can be shown [31] that the phase difference between the two junctions is given by,

$$\gamma_2 - \gamma_1 = \frac{2\pi}{\Phi_0}(\Phi_a + LJ) = \frac{2\pi}{\Phi_0}\Phi_{Tot} \tag{A.15}$$

where L is the inductance of the loop, Φ_a is the applied flux, and Φ_{Tot} is the total flux. Including the inductance of the loop it can be shown that for $2LI_c \geq \Phi_0$, the total flux is hysteric as a function of applied flux; a property which will be important for the RF SQUID but is usually undesirable for a DC SQUID. First, we consider the zero voltage bias case (derivatives = 0) with no inductance where adding the current through the two junctions leads to,

$$I = I_c \sin(\gamma_1) + I_c \sin(\gamma_2) = I_c \sin(\gamma_1) + I_c \sin\left(\gamma_1 + \frac{2\pi}{\Phi_0}\Phi_a\right). \tag{A.16}$$

The goal is to get an equation of the form Eq. A.11 and to this end we define $\gamma = \gamma_1 + \pi\frac{\Phi_a}{\Phi_0}$ leading to,

$$I = 2I_c \sin(\gamma)\cos\left(\frac{\pi\Phi_a}{\Phi_0}\right). \tag{A.17}$$

For the case of negligible inductance, the derivatives of γ_1 and γ_2 are equal, while again assuming the capacitance is negligible the total current through the DC SQUID is given

by,

$$I = 2I_c \sin(\gamma) \cos\left(\frac{\pi\Phi_a}{\Phi_0}\right) + \frac{\Phi_0}{2\pi R}\frac{\partial\gamma}{\partial t} \tag{A.18}$$

which using the same process as in Eq. A.13 has solution

$$V = \frac{1}{R}\sqrt{I^2 - I_c^2 \cos^2\left(\frac{\pi\Phi_a}{\Phi_0}\right)}, \tag{A.19}$$

that is, the voltage is periodic in the applied flux with period Φ_0. It can be shown that the peak-to-peak voltage is largest when the bias current is equal to $2\ I_c^2 \cos^2\left(\frac{\pi\Phi_a}{\Phi_0}\right)$ [31] and it is readily seen that the derivative attains a maximum at $(2n+1)\,\frac{\Phi_0}{4}, n = 0, 1, 2....$

Appendix B

Derivation of Scaling Relations

In this appendix we derive the scaling relations for the complex susceptibility which allow us to better access if our data follows a Havriliak-Negami form.

We begin with the Havriliak-Negami form [62],

$$\chi = \chi' - i\chi'' = \frac{\chi_0}{(1 + (i\omega\tau)^\alpha)^\gamma}, \tag{B.1}$$

then divide through by χ_0 and take the γth root leading to,

$$G\left(\chi_0, \chi', \chi'', \gamma\right) = \left(\frac{\chi' - i\chi''}{\chi_0}\right)^{1/\gamma} = \frac{1}{1 + (i\omega\tau)^\alpha}. \tag{B.2}$$

where we have defined, $\mathrm{G}(\chi_0, \chi', \chi'', \gamma)$ to be the left hand side of B.2. We now apply some identities from complex analys to break $\mathrm{G}(\chi_0, \chi', \chi'', \gamma)$ into real and imaginary parts,

$$G\left(\chi_0, \chi', \chi'', \gamma\right) = \left(\frac{\chi'^2 + \chi''^2}{\chi_0^2}\right)^{1/2\gamma} \left[\cos\left(\frac{1}{\gamma}\arctan\left(\frac{\chi''}{\chi'}\right)\right) - i\sin\left(\frac{1}{\gamma}\arctan\left(\frac{\chi''}{\chi'}\right)\right)\right]. \tag{B.3}$$

We can do the same thing with the right hand side (RHS) of Eq. B.2 leading to

$$\mathrm{Re}\left[\frac{1}{1 + (i\omega\tau)^\alpha}\right] = \frac{1 + (\omega\tau)^\alpha \cos\left(\frac{\pi\alpha}{2}\right)}{1 + (\omega\tau)^\alpha \cos\left(\frac{\pi\alpha}{2}\right) + (\omega\tau)^{2\alpha}}, \tag{B.4}$$

for the real component and,

$$\mathrm{Im}\left[\frac{1}{1 + (i\omega\tau)^\alpha}\right] = \frac{(\omega\tau)^\alpha \sin\left(\frac{\pi\alpha}{2}\right)}{1 + (\omega\tau)^\alpha \cos\left(\frac{\pi\alpha}{2}\right) + (\omega\tau)^{2\alpha}}, \tag{B.5}$$

for the imaginary component. Equating the real and imaginary parts of Eq. B.2 to Eq. B.4 and Eq. B.5, respectively, shows that the real and imaginary part of $\mathrm{G}(\chi_0, \chi', \chi'', \gamma)$ should follow a universal form. Therefore, applying the scaling relation $\mathrm{G}(\chi_0, \chi', \chi'', \gamma)$ to

our measured and fit quantities allows us to easily assess how well the AC susceptibility follows an HN form. We plot Eq. B.4 and Eq. B.5 below.

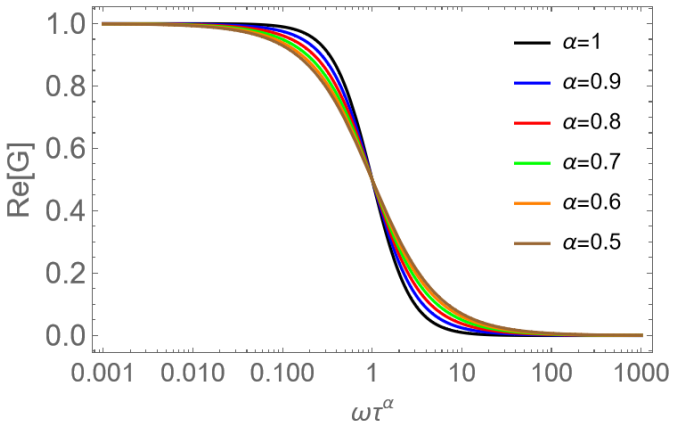

(A) Real part of the scaling relation $G(\chi_0, \chi', \chi'', \gamma)$

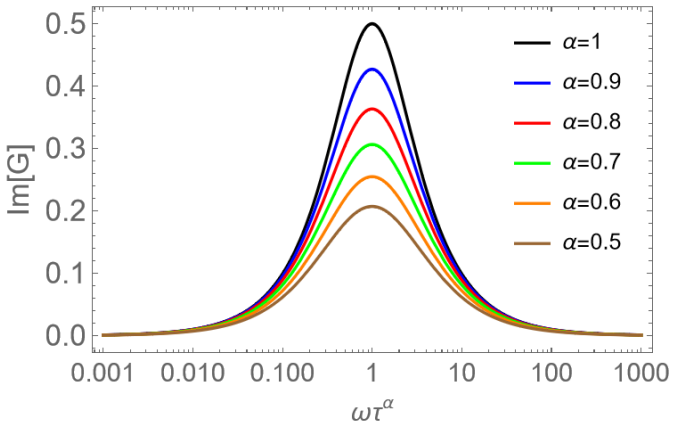

(B) Imaginary part of the scaling relation $G(\chi_0, \chi', \chi'', \gamma)$

Figure A2.1: Visualization of the scaling relations.

Bibliography

[1] A. A. Abrikosov. On the Magnetic properties of superconductors of the second group. *Sov. Phys. JETP* 5 (1957), 1174–1182.

[2] V. K. Anand, D. L. Abernathy, D. T. Adroja, A. D. Hillier, P. K. Biswas, and B. Lake. Muon spin relaxation and inelastic neutron scattering investigations of the all-in/all-out antiferromagnet $Nd_2Hf_2O_7$. *Phys. Rev. B* 95 (22 June 2017), 224420.

[3] V. K. Anand, A. K. Bera, J. Xu, T. Herrmannsdörfer, C. Ritter, and B. Lake. Observation of long-range magnetic ordering in pyrohafnate $Nd_2Hf_2O_7$: A neutron diffraction study. *Phys. Rev. B* 92 (18 Nov. 2015), 184418.

[4] P. W. Anderson. Ordering and Antiferromagnetism in Ferrites. *Phys. Rev.* 102 (4 May 1956), 1008–1013.

[5] C. Angell. Entropy and fragility in supercooling liquids. *Journal of Research of the National Institute of Standards and Technology* 102(2) (1997), 171.

[6] N. W. Ashcroft and N. D. Mermin. *Solid state physics*. Harcourt College, 1999.

[7] J. Bardeen, L. N. Cooper, and J. R. Schrieffer. Microscopic Theory of Superconductivity. *Phys. Rev.* 106 (1 Apr. 1957), 162–164.

[8] J. Beare, M. Nugent, M. N. Wilson, Y. Cai, T. J. S. Munsie, A. Amon, A. Leithe-Jasper, Z. Gong, S. L. Guo, Z. Guguchia, Y. Grin, Y. J. Uemura, E. Svanidze, and G. M. Luke. μSR and magnetometry study of the type-I superconductor BeAu. *Phys. Rev. B* 99 (13 Apr. 2019), 134510.

[9] J. Beare, S. M. Koohpayeh, Y. Cai, M. Nugent, M. Pula, S. Sharma, S. Yoon, S. R. Dunsiger, K. Kojima, and G. Luke. Magnetism in Tb2Ti2O7 with low defect concentration, unpublished. 2020.

[10] O. Benton. Quantum origins of moment fragmentation in $Nd_2Zr_2O_7$. *Phys. Rev. B* 94 (10 Sept. 2016), 104430.

[11] O. Benton. Ground-state phase diagram of dipolar-octupolar pyrochlores. *Phys. Rev. B* 102 (10 Sept. 2020), 104408.

[12] O. Benton, L. D. C. Jaubert, R. R. P. Singh, J. Oitmaa, and N. Shannon. Quantum Spin Ice with Frustrated Transverse Exchange: From a π-Flux Phase to a Nematic Quantum Spin Liquid. *Phys. Rev. Lett.* 121 (6 Aug. 2018), 067201.

[13] A. Bertin, P. Dalmas de Réotier, B. Fåk, C. Marin, A. Yaouanc, A. Forget, D. Sheptyakov, B. Frick, C. Ritter, A. Amato, C. Baines, and P. J. C. King. $Nd_2Sn_2O_7$: An all-in–all-out pyrochlore magnet with no divergence-free field and anomalously slow paramagnetic spin dynamics. *Phys. Rev. B* 92 (14 Oct. 2015), 144423.

[14] R. Böhmer, K. L. Ngai, C. A. Angell, and D. J. Plazek. Nonexponential relaxations in strong and fragile glass formers. *The Journal of Chemical Physics* 99(5) (1993), 4201–4209.

[15] P. Bonville, J. A. Hodges, E. Bertin, J.-P. Bouchaud, P. D. D. Réotier, L.-P. Regnault, H. M. Rønnow, J.-P. Sanchez, S. Sosin, A. Yaouanc, and et al. Transitions and Spin Dynamics at Very Low Temperature in the Pyrochlores Yb2Ti2O7 and Gd2Sn2O7. *Icame 2003* (2004), 103–111.

[16] P. Bonville, J. A. Hodges, M. Ocio, J. P. Sanchez, P. Vulliet, S. Sosin, and D. Braithwaite. Low temperature magnetic properties of geometrically frustrated Gd2Sn2O7and Gd2Ti2O7. *Journal of Physics: Condensed Matter* 15(45) (Oct. 2003), 7777–7787.

[17] S. T. Bramwell, S. R. Giblin, S. Calder, R. Aldus, D. Prabhakaran, and T. Fenell. Measurement of the charge and current of magnetic monopoles in spin ice. *Nature* 461 (Oct. 2009), 956–959.

[18] M. E. Brooks-Bartlett, S. T. Banks, L. D. C. Jaubert, A. Harman-Clarke, and P. C. W. Holdsworth. Magnetic-Moment Fragmentation and Monopole Crystallization. *Phys. Rev. X* 4 (1 Jan. 2014), 011007.

[19] Y. Cai, M. N. Wilson, A. M. Hallas, L. Liu, B. A. Frandsen, S. R. Dunsiger, J. W. Krizan, R. J. Cava, O. Rubel, Y. J. Uemura, and G. M. Luke. SR study of spin freezing and persistent spin dynamics in NaCaNi2F7. *Journal of Physics: Condensed Matter* 30(38) (Aug. 2018), 385802.

[20] Y. Cai. Frustrated Magnetism Studies in NaCaNi2F7, Er3Ga5O12 and ErMgGaO4. PhD thesis. 2019.

[21] I. A. Campbell, A. Amato, F. N. Gygax, D. Herlach, A. Schenck, R. Cywinski, and S. H. Kilcoyne. Dynamics in canonical spin glasses observed by muon spin depolarization. *Phys. Rev. Lett.* 72 (8 Feb. 1994), 1291–1294.

[22] B. Canals and C. Lacroix. Pyrochlore Antiferromagnet: A Three-Dimensional Quantum Spin Liquid. *Phys. Rev. Lett.* 80 (13 Mar. 1998), 2933–2936.

[23] B. Canals and C. Lacroix. Quantum spin liquid: The Heisenberg antiferromagnet on the three-dimensional pyrochlore lattice. *Phys. Rev. B* 61 (2 Jan. 2000), 1149–1159.

[24] J. Carrasquilla, Z. Hao, and R. G. Melko. A two-dimensional spin liquid in quantum kagome ice. *Nature Communications* 6(1) (2015).

[25] H. Casimir and F. D. Pré. Note on the thermodynamic interpretation of paramagnetic relaxation phenomena. *Physica* 5(6) (1938), 507–511.

[26] C. Castelnovo, R. Moessner, and S. Sondhi. Spin Ice, Fractionalization, and Topological Order. *Annual Review of Condensed Matter Physics* 3(1) (Mar. 2012), 35–55. ISSN: 1947-5462.

[27] C. Castelnovo, R. Moessner, and S. L. Sondhi. Magnetic monopoles in spin ice. *Nature* 451 (Jan. 2008), 42–45.

[28] A. Cavagna. Supercooled liquids for pedestrians. *Physics Reports* 476(4-6) (2009), 51–124.

[29] J. D. M. Champion, A. S. Wills, T. Fennell, S. T. Bramwell, J. S. Gardner, and M. A. Green. Order in the Heisenberg pyrochlore: The magnetic structure of $Gd_2Ti_2O_7$. *Phys. Rev. B* 64 (14 Sept. 2001), 140407.

[30] J. P. Clancy, J. P. C. Ruff, S. R. Dunsiger, Y. Zhao, H. A. Dabkowska, J. S. Gardner, Y. Qiu, J. R. D. Copley, T. Jenkins, and B. D. Gaulin. Revisiting static and dynamic spin-ice correlations in $Ho_2Ti_2O_7$ with neutron scattering. *Phys. Rev. B* 79 (1 Jan. 2009), 014408.

[31] J. Clarke and A. I. Braginski. *The SQUID handbook*. Vol. I. Wiley-VCH, 2005.

[32] R. Cywinski, S. H. Kilcoyne, and S. L. Lee. *Muon science: muons in physics, chemistry, and materials ; proceedings of the Fifty First Scottish Universities Summer School in Physics, St. Andrews, August 1998*. Scottish Universities Summer School in Physics.

[33] R. Cywinski and B. D. Rainford. Spin dynamics in the spin glass phase of Y(Mn1xAlx)2. *Hyperfine Interactions* 85(1) (1994), 215–220.

[34] R. M. D'Ortenzio, H. A. Dabkowska, S. R. Dunsiger, B. D. Gaulin, M. J. P. Gingras, T. Goko, J. B. Kycia, L. Liu, T. Medina, T. J. Munsie, D. Pomaranski, K. A. Ross, Y. J. Uemura, T. J. Williams, and G. M. Luke. Unconventional magnetic ground state in $Yb_2Ti_2O_7$. *Phys. Rev. B* 88 (13 Oct. 2013), 134428.

[35] P. Dalmas de Réotier, A. Yaouanc, L. Keller, A. Cervellino, B. Roessli, C. Baines, A. Forget, C. Vaju, P. C. M. Gubbens, A. Amato, and P. J. C. King. Spin Dynamics and Magnetic Order in Magnetically Frustrated $Tb_2Sn_2O_7$. *Phys. Rev. Lett.* 96 (12 Mar. 2006), 127202.

[36] A. Del Maestro and M. J. P. Gingras. Low-temperature specific heat and possible gap to magnetic excitations in the Heisenberg pyrochlore antiferromagnet $Gd_2Sn_2O_7$. *Phys. Rev. B* 76 (6 Aug. 2007), 064418.

[37] Z. Dun, X. Bai, J. A. M. Paddison, E. Hollingworth, N. P. Butch, C. D. Cruz, M. B. Stone, T. Hong, F. Demmel, M. Mourigal, and H. Zhou. Quantum Versus Classical Spin Fragmentation in Dipolar Kagome Ice $Ho_3Mg_2Sb_3O_{14}$. *Phys. Rev. X* 10 (3 Sept. 2020), 031069.

[38] S. R. Dunsiger, A. A. Aczel, C. Arguello, H. Dabkowska, A. Dabkowski, M.-H. Du, T. Goko, B. Javanparast, T. Lin, F. L. Ning, H. M. L. Noad, D. J. Singh, T. J. Williams, Y. J. Uemura, M. J. P. Gingras, and G. M. Luke. Spin Ice: Magnetic Excitations without Monopole Signatures Using Muon Spin Rotation. *Phys. Rev. Lett.* 107 (20 Nov. 2011), 207207.

[39] S. R. Dunsiger, R. F. Kiefl, J. A. Chakhalian, J. E. Greedan, W. A. Macfarlane, R. I. Miller, G. D. Morris, A. N. Price, N. P. Raju, J. E. Sonier, and et al. Magnetic field dependence of muon spin relaxation in geometrically frustrated Gd2Ti2O7. *Physical Review B* 73(17) (2006).

[40] S. R. Dunsiger, R. F. Kiefl, K. H. Chow, B. D. Gaulin, M. J. P. Gingras, J. E. Greedan, A. Keren, K. Kojima, G. M. Luke, W. A. Macfarlane, and et al. Low temperature spin dynamics of geometrically frustrated antiferromagnets Y2Mo2O7 and Y2Mo1.6Ti0.4O7 studied by muon spin relaxation. *Journal of Applied Physics* 79(8) (1996), 6636.

[41] S. R. Dunsiger, R. F. Kiefl, K. H. Chow, B. D. Gaulin, M. J. P. Gingras, J. E. Greedan, A. Keren, K. Kojima, G. M. Luke, W. A. MacFarlane, N. P. Raju, J. E. Sonier, Y. J. Uemura, and W. D. Wu. Muon spin relaxation investigation of the spin dynamics of geometrically frustrated antiferromagnets $Y_2Mo_2O_7$ and $Tb_2Mo_2O_7$. *Phys. Rev. B* 54 (13 Oct. 1996), 9019–9022.

[42] R. Dusad and J. C. Davis. Magnetic monopole noise. PhD thesis. 2020.

[43] R. Dusad, F. K. K. Kirschner, J. C. Hoke, B. R. Roberts, A. Eyal, F. Flicker, G. M. Luke, S. J. Blundell, and J. C. S. Davis. Magnetic monopole noise. *Nature* 571(7764) (July 2019), 234–239. ISSN: 1476-4687.

[44] M. D. Ediger, C. A. Angell, and S. R. Nagel. Supercooled Liquids and Glasses. *The Journal of Physical Chemistry* 100(31) (1996), 13200–13212.

[45] A. B. Eyvazov, R. Dusad, T. J. S. Munsie, H. A. Dabkowska, G. M. Luke, E. R. Kassner, J. C. S. Davis, and A. Eyal. Common glass-forming spin-liquid state in the pyrochlore magnets $Dy_2Ti_2O_7$ and $Ho_2Ti_2O_7$. *Phys. Rev. B* 98 (21 Dec. 2018), 214430.

[46] R. L. Fagaly. Superconducting quantum interference device instruments and applications. *Review of Scientific Instruments* 77(10) (2006), 101101.

[47] T. Fennell, O. A. Petrenko, B. Fåk, S. T. Bramwell, M. Enjalran, T. Yavors'kii, M. J. P. Gingras, R. G. Melko, and G. Balakrishnan. Neutron scattering investigation of the spin ice state in $Dy_2Ti_2O_7$. *Phys. Rev. B* 70 (13 Oct. 2004), 134408.

[48] T. Fennell, O. A. Petrenko, B. Fåk, J. S. Gardner, S. T. Bramwell, and B. Ouladdiaf. Neutron scattering studies of the spin ices $Ho_2Ti_2O_7$ and $Dy_2Ti_2O_7$ in applied magnetic field. *Phys. Rev. B* 72 (22 Dec. 2005), 224411.

[49] K. H. Fischer and J. Hertz. *Spin glasses*. Cambridge Univ. Press, 1999.

[50] J. C. Gallop and B. W. Petley. SQUIDs and their applications. *Journal of Physics E: Scientific Instruments* 9(6) (1976), 417–429.

[51] J. S. Gardner, B. D. Gaulin, S.-H. Lee, C. Broholm, N. P. Raju, and J. E. Greedan. Glassy Statics and Dynamics in the Chemically Ordered Pyrochlore Antiferromagnet $Y_2Mo_2O_7$. *Phys. Rev. Lett.* 83 (1 July 1999), 211–214.

[52] J. S. Gardner, M. J. P. Gingras, and J. E. Greedan. ChemInform Abstract: Magnetic Pyrochlore Oxides. *ChemInform* 41(39) (2010).

[53] V. N. Glazkov, M. E. Zhitomirsky, A. I. Smirnov, H.-A. Krug von Nidda, A. Loidl, C. Marin, and J.-P. Sanchez. Single-ion anisotropy in the gadolinium pyrochlores studied by electron paramagnetic resonance. *Phys. Rev. B* 72 (2 July 2005), 020409.

[54] J. B. Goodenough. Theory of the Role of Covalence in the Perovskite-Type Manganites[La, M(II)]MnO3. *Physical Review* 100(2) (1955), 564–573.

[55] C. Grey, A. Cheetham, and C. Dobson. Temperature-Dependent Solid-State 119Sn-MAS NMR of Nd2Sn2O7, Sm2Sn2O7, and Y1.8Sm0.2Sn2O7. Three Sensitive Chemical-Shift Thermometers. *Journal of Magnetic Resonance, Series A* 101(3) (1993), 299–306. ISSN: 1064-1858.

[56] P. C. Guruciaga, L. Pili, S. Boyeras, D. Slobinsky, S. A. Grigera, and R. A. Borzi. Anomalous out-of-equilibrium dynamics in the spin-ice material Dy2Ti2O7 under moderate magnetic fields. *Journal of Physics: Condensed Matter* 32(42) (July 2020), 425804.

[57] A. M. Hallas, A. M. Arevalo-Lopez, A. Z. Sharma, T. Munsie, J. P. Attfield, C. R. Wiebe, and G. M. Luke. Magnetic frustration in lead pyrochlores. *Phys. Rev. B* 91 (10 Mar. 2015), 104417.

[58] A. M. Hallas, A. Z. Sharma, Y. Cai, T. J. Munsie, M. N. Wilson, M. Tachibana, C. R. Wiebe, and G. M. Luke. Relief of frustration in the Heisenberg pyrochlore antiferromagnet Gd2Pt2O7. *Physical Review B* 94(13) (2016).

[59] A. Hallas. The Effect of Chemical Pressure on the Magnetic Ground States of Rare Earth Pyrochlores. PhD thesis. 2017.

[60] A. M. Hallas, J. Gaudet, and B. D. Gaulin. Experimental Insights into Ground-State Selection of Quantum XY Pyrochlores. *Annual Review of Condensed Matter Physics* 9(1) (2018), 105–124.

[61] M. J. Harris, S. T. Bramwell, D. F. McMorrow, T. Zeiske, and K. W. Godfrey. Geometrical Frustration in the Ferromagnetic Pyrochlore $Ho_2Ti_2O_7$. *Phys. Rev. Lett.* 79 (13 Sept. 1997), 2554–2557.

[62] S. Havriliak and S. Negami. A complex plane representation of dielectric and mechanical relaxation processes in some polymers. *Polymer (Guildf)* 8 (1967), 161–210.

[63] R. S. Hayano, Y. J. Uemura, J. Imazato, N. Nishida, T. Yamazaki, and R. Kubo. Zero-and low-field spin relaxation studied by positive muons. *Phys. Rev. B* 20 (3 Aug. 1979), 850–859.

[64] M. Hermele, M. P. A. Fisher, and L. Balents. Pyrochlore photons: The $U(1)$ spin liquid in a $S = \frac{1}{2}$ three-dimensional frustrated magnet. *Phys. Rev. B* 69 (6 Feb. 2004), 064404.

[65] B. C. den Hertog and M. J. P. Gingras. Dipolar Interactions and Origin of Spin Ice in Ising Pyrochlore Magnets. *Phys. Rev. Lett.* 84 (15 Apr. 2000), 3430–3433.

[66] C. Huang. Some experimental aspects of spin glasses: A review. *Journal of Magnetism and Magnetic Materials* 51(1-3) (1985), 1–74.

[67] Y.-P. Huang, G. Chen, and M. Hermele. Quantum Spin Ices and Topological Phases from Dipolar-Octupolar Doublets on the Pyrochlore Lattice. *Phys. Rev. Lett.* 112 (16 Apr. 2014), 167203.

[68] *Introduction to frustrated magnetism*. Springer-Verlag, 2013.

[69] L. D. C. Jaubert and P. C. W. Holdsworth. Magnetic monopole dynamics in spin ice. *Journal of Physics: Condensed Matter* 23(16) (2011), 164222.

[70] B. Javanparast, A. G. R. Day, Z. Hao, and M. J. P. Gingras. Order-by-disorder near criticality in XY pyrochlore magnets. *Phys. Rev. B* 91 (17 May 2015), 174424.

[71] J. Kanamori. Superexchange interaction and symmetry properties of electron orbitals. *Journal of Physics and Chemistry of Solids* 10(2-3) (1959), 87–98.

[72] E. Kassner. A Supercooled Liquid State in the Frustrated Pyrochlore Dy2Ti2O7. PhD thesis. 2015.

[73] E. R. Kassner, A. B. Eyvazov, B. Pichler, T. J. S. Munsie, H. A. Dabkowska, G. M. Luke, and J. C. S. Davis. Supercooled spin liquid state in the frustrated pyrochlore Dy2Ti2O7. *Proceedings of the National Academy of Sciences* 112(28) (2015), 8549–8554.

[74] A. Keren, P. Mendels, I. A. Campbell, and J. Lord. Probing the Spin-Spin Dynamical Autocorrelation Function in a Spin Glass above T_g via Muon Spin Relaxation. *Phys. Rev. Lett.* 77 (7 Aug. 1996), 1386–1389.

[75] R. Kubo and T. Toyabe. *Magnetic Resonance and Relaxation*. Ed. by R. Blinc. 1967.

[76] J. Lago, T. Lancaster, S. J. Blundell, S. T. Bramwell, F. L. Pratt, M. Shirai, and C. Baines. Magnetic ordering and dynamics in the XY pyrochlore antiferromagnet: a muon-spin relaxation study of Er2Ti2O7and Er2Sn2O7. *Journal of Physics: Condensed Matter* 17(6) (Jan. 2005), 979–988.

[77] E. Lhotel, S. Petit, S. Guitteny, O. Florea, M. Ciomaga Hatnean, C. Colin, E. Ressouche, M. R. Lees, and G. Balakrishnan. Fluctuations and All-In–All-Out Ordering in Dipole-Octupole $Nd_2Zr_2O_7$. *Phys. Rev. Lett.* 115 (19 Nov. 2015), 197202.

[78] E. Lhotel, S. Petit, M. C. Hatnean, J. Ollivier, H. Mutka, E. Ressouche, M. R. Lees, and G. Balakrishnan. Evidence for dynamic kagome ice. *Nature Communications* 9(1) (2018).

[79] C. Liu, G. B. Halász, and L. Balents. Competing orders in pyrochlore magnets from a Z_2 spin liquid perspective. *Phys. Rev. B* 100 (7 Aug. 2019), 075125.

[80] V. Lubchenko and P. G. Wolynes. Theory of Structural Glasses and Supercooled Liquids. *Annual Review of Physical Chemistry* 58(1) (2007). PMID: 17067282, 235–266.

[81] B. Z. Malkin, T. T. A. Lummen, P. H. M. van Loosdrecht, G. Dhalenne, and A. R. Zakirov. Static magnetic susceptibility, crystal field and exchange interactions in rare earth titanate pyrochlores. *Journal of Physics: Condensed Matter* 22(27) (June 2010), 276003.

[82] K. Matsuhira, Y. Hinatsu, and T. Sakakibara. Novel dynamical magnetic properties in the spin ice compound Dy2Ti2O7. *Journal of Physics: Condensed Matter* 13(31) (2001).

[83] K. Matsuhira, C. Paulsen, E. Lhotel, C. Sekine, Z. Hiroi, and S. Takagi. Spin Dynamics at Very Low Temperature in Spin Ice Dy2Ti2O7. *Journal of the Physical Society of Japan* 80(12) (2011), 123711.

[84] C. Mauws, A. M. Hallas, G. Sala, A. A. Aczel, P. M. Sarte, J. Gaudet, D. Ziat, J. A. Quilliam, J. A. Lussier, M. Bieringer, and et al. Dipolar-octupolar Ising antiferromagnetism in Sm2Ti2O7: A moment fragmentation candidate. *Physical Review B* 98(10) (2018).

[85] C. Mauws, J. Beare, M. Lee, M. Nugent, M. Rutherford, S. Sharma, Y. Su, L. J. Chang, S. Dunsiger, J. Gardner, G. Luke, and C. Weibe. Spin Glass state in the Gd2ScNbO7 Pyrochlore. 2021.

[86] C. Mauws, N. Hiebert, M. Rutherford, H. Zhou, Q. Huang, M. B. Stone, N. Butch, Y. Su, E. S. Choi, Z. Yamani, and et al. Magnetic Ordering in the Ising Antiferromagnetic Pyrochlore Nd2ScNbO7. *Journal of Physics: Condensed Matter* (2021).

[87] W. Meissner and R. Ochsenfeld. *Naturwissenschaften* 21(44) (1933), 787.

[88] R. G. Melko and M. J. P. Gingras. Monte Carlo studies of the dipolar spin ice model. *Journal of Physics: Condensed Matter* 16(43) (Oct. 2004), R1277–R1319.

[89] R. Moessner and J. T. Chalker. Properties of a Classical Spin Liquid: The Heisenberg Pyrochlore Antiferromagnet. *Phys. Rev. Lett.* 80 (13 Mar. 1998), 2929–2932.

[90] G. Moskal, A. Jasik, M. Mikuśkiewicz, and S. Jucha. Thermal resistance determination of Sm2Zr2O7 + 8YSZ composite type of TBC. *Applied Surface Science* 515 (2020), 145998. ISSN: 0169-4332.

[91] *Muon science: muons in physics, chemistry, and materials: proceedings of the fifty first Scottish Universities Summer School in Physics, St. Andrews, August 1998*. Scottish Universities Summer School in Physics, 2001.

[92] J. A. Mydosh. *Spin glasses: an experimental introduction*. Taylor and Francis, 1993.

[93] A. T. Ogielski. Dynamics of three-dimensional Ising spin glasses in thermal equilibrium. *Phys. Rev. B* 32 (11 Dec. 1985), 7384–7398.

[94] H. Onnes. Koninklijke Academie van Wetenschappen te Amsterdam. In: *Communications Leiden 120b:122b:124c*. 1911.

[95] J. A. Osborn. Demagnetizing Factors of the General Ellipsoid. *Phys. Rev.* 67 (11-12 June 1945), 351–357.

[96] J. A. M. Paddison, G. Ehlers, A. B. Cairns, J. S. Gardner, O. A. Petrenko, N. P. Butch, D. D. Khalyavin, P. Manuel, H. E. Fischer, H. Zhou, A. L. Goodwin, and J. R. Stewart. *Nature of Partial Magnetic Order in the Frustrated Antiferromagnet Gd2Ti2O7*. 2020.

[97] S. E. Palmer and J. T. Chalker. Order induced by dipolar interactions in a geometrically frustrated antiferromagnet. *Phys. Rev. B* 62 (1 July 2000), 488–492.

[98] V. Peçanha-Antonio, E. Feng, X. Sun, D. Adroja, H. C. Walker, A. S. Gibbs, F. Orlandi, Y. Su, and T. Brückel. Intermultiplet transitions and magnetic long-range order in Sm-based pyrochlores. *Physical Review B* 99(13) (2019).

[99] S. Petit, E. Lhotel, S. Guitteny, O. Florea, J. Robert, P. Bonville, I. Mirebeau, J. Ollivier, H. Mutka, E. Ressouche, C. Decorse, M. Ciomaga Hatnean, and G. Balakrishnan. Antiferroquadrupolar correlations in the quantum spin ice candidate $\mathbf{Pr_2Zr_2O_7}$. *Phys. Rev. B* 94 (16 Oct. 2016), 165153.

[100] S. Petit, E. Lhotel, and G. Balakrishnan. Observation of magnetic fragmentation in spin ice. *Nature Physics* (12) (Apr. 2016), 746–750.

[101] D. Pomaranski, L. R. Yaraskavitch, S. Meng, K. A. Ross, H. M. L. Noad, H. A. Dabkowska, B. D. Gaulin, and J. B. Kycia. Absence of Pauling's residual entropy in thermally equilibrated Dy2Ti2O7. *Nature Physics* 9(6) (2013), 353–356.

[102] A. P. Ramirez. Strongly Geometrically Frustrated Magnets. *Annual Review of Materials Science* 24(1) (1994), 453–480.

[103] A. P. Ramirez, A. Hayashi, R. J. Cava, R. Siddharthan, and B. S. Shastry. Zero-point entropy in 'spin ice'. *Nature* 399(6734) (1999), 333–335.

[104] J. G. Rau and M. J. P. Gingras. Magnitude of quantum effects in classical spin ices. *Phys. Rev. B* 92 (14 Oct. 2015), 144417.

[105] J. G. Rau and M. J. Gingras. Frustrated Quantum Rare-Earth Pyrochlores. *Annual Review of Condensed Matter Physics* 10(1) (2019), 357–386.

[106] P. D. D. Réotier and A. Yaouanc. Muon spin rotation and relaxation in magnetic materials. *Journal of Physics: Condensed Matter* 9(43) (1997), 9113–9166.

[107] P. D. D. Réotier, A. Maisuradze, and A. Yaouanc. Recent SR Studies of Insulating Rare-Earth Pyrochlore Magnets. *Journal of the Physical Society of Japan* 85(9) (2016), 091010.

[108] H. M. Revell, L. R. Yaraskavitch, J. D. Mason, K. A. Ross, H. M. L. Noad, H. A. Dabkowska, B. D. Gaulin, P. Henelius, and J. B. Kycia. Evidence of impurity and boundary effects on magnetic monopole dynamics in spin ice. *Nature Physics* 9(1) (2012), 34–37.

[109] J. Rodriguez-Carvajal. FULLPROF: a program for Rietveld refinement and pattern matching analysis. In: *satellite meeting on powder diffraction of the XV congress of the IUCr*. Vol. 127. Toulouse, France]. 1990.

[110] K. A. Ross, T. Proffen, H. A. Dabkowska, J. A. Quilliam, L. R. Yaraskavitch, J. B. Kycia, and B. D. Gaulin. Lightly stuffed pyrochlore structure of single-crystalline $Yb_2Ti_2O_7$ grown by the optical floating zone technique. *Phys. Rev. B* 86 (17 Nov. 2012), 174424.

[111] J. P. C. Ruff, R. G. Melko, and M. J. P. Gingras. Finite-Temperature Transitions in Dipolar Spin Ice in a Large Magnetic Field. *Phys. Rev. Lett.* 95 (9 Aug. 2005), 097202.

[112] A. Samartzis. Magnetic investigation of effective spin-1/2 magnetic insulators based on 3d and 4f magnetic ions. PhD thesis.

[113] L. Savary and L. Balents. Disorder-Induced Quantum Spin Liquid in Spin Ice Pyrochlores. *Phys. Rev. Lett.* 118 (8 Feb. 2017), 087203.

[114] A. Scheie, M. Sanders, X. Gui, Y. Qiu, T. R. Prisk, R. J. Cava, and C. Broholm. Beyond magnons in Nd_2ScNbO_7: An Ising pyrochlore antiferromagnet with all-in–all-out order and random fields. *Phys. Rev. B* 104 (13 Oct. 2021), 134418.

[115] J. Shi, Z. Tang, B. Zhu, P. Huang, D. Yin, C. Li, Y. Wang, and H. Wen. Dynamical magnetic properties of the spin ice crystal Dy2Ti2O7. *Journal of Magnetism and Magnetic Materials* 310(2, Part 2) (2007). Proceedings of the 17th International Conference on Magnetism, 1322–1324. ISSN: 0304-8853.

[116] A. H. Silver and J. E. Zimmerman. Quantum States and Transitions in Weakly Connected Superconducting Rings. *Physical Review* 157(2) (1967), 317–341.

[117] S. Singh, S. Saha, S. K. Dhar, R. Suryanarayanan, A. K. Sood, and A. Revcolevschi. Manifestation of geometric frustration on magnetic and thermodynamic properties of the pyrochlores $Sm_2X_2O_7$ (X = Ti, Zr). *Phys. Rev. B* 77 (5 Feb. 2008), 054408.

[118] J. Snyder, B. G. Ueland, J. S. Slusky, H. Karunadasa, R. J. Cava, and P. Schiffer. Low-temperature spin freezing in the $Dy_2Ti_2O_7$ spin ice. *Phys. Rev. B* 69 (6 Feb. 2004), 064414.

[119] J. Sonier. 2002.

[120] *Springer Handbook of Crystal Growth*. Springer, 2010.

[121] K. W. H. Stevens. Matrix Elements and Operator Equivalents Connected with the Magnetic Properties of Rare Earth Ions. *Proceedings of the Physical Society. Section A* 65(3) (1952), 209–215.

[122] J. R. Stewart, G. Ehlers, A. S. Wills, S. T. Bramwell, and J. S. Gardner. Phase transitions, partial disorder and multi-kstructures in Gd2Ti2O7. *Journal of Physics: Condensed Matter* 16(28) (July 2004), L321–L326.

[123] J. Stewart, A. Hillier, S. Kilcoyne, P. Manuel, M. Telling, and R. Cywinski. Moment localisation in -MnAl. *Journal of Magnetism and Magnetic Materials* 177-181 (1998), 602–604.

[124] V. L. Stolyarova, V. A. Vorozhtcov, A. L. Shilov, S. I. Lopatin, and S. M. Shugurov. Ceramics based on the Sm2O3–Y2O3 and Sm2O3–HfO2 systems at high temperatures: Thermodynamics and modeling. *Materials Chemistry and Physics* 252 (2020), 123240. ISSN: 0254-0584.

[125] A. Suter and B. Wojek. Musrfit: A Free Platform-Independent Framework for SR Data Analysis. *Physics Procedia* 30 (2012), 69–73.

[126] H. Takatsu, K. Goto, H. Otsuka, R. Higashinaka, K. Matsubayashi, Y. Uwatoko, and H. Kadowaki. AC Susceptibility of the Dipolar Spin Ice Dy2Ti2O7: Experiments and Monte Carlo Simulations. *Journal of the Physical Society of Japan* 82(10) (2013), 104710.

[127] T. Taniguchi, H. Kadowaki, H. Takatsu, B. Fåk, J. Ollivier, T. Yamazaki, T. J. Sato, H. Yoshizawa, Y. Shimura, T. Sakakibara, T. Hong, K. Goto, L. R. Yaraskavitch, and J. B. Kycia. Long-range order and spin-liquid states of polycrystalline $Tb_{2+x}Ti_{2-x}O_{7+y}$. *Phys. Rev. B* 87 (6 Feb. 2013), 060408.

[128] G. Tarjus, S. A. Kivelson, Z. Nussinov, and P. Viot. The frustration-based approach of supercooled liquids and the glass transition: a review and critical assessment. *Journal of Physics: Condensed Matter* 17(50) (Dec. 2005), R1143–R1182. ISSN: 1361-648X.

[129] M. Telling, C. Ritter, and R. Cywinski. Dynamic spin correlations in (Dy1 xYx)Mn2. *Journal of Magnetism and Magnetic Materials* 177-181 (1998). International Conference on Magnetism (Part II), 1480–1481. ISSN: 0304-8853.

[130] Z. Tian, Y. Kohama, T. Tomita, H. Ishizuka, T. H. Hsieh, J. J. Ishikawa, K. Kindo, L. Balents, and S. Nakatsuji. Field-induced quantum metal–insulator transition in the pyrochlore iridate Nd2Ir2O7. *Nature Physics* 12(2) (2015), 134–138.

[131] M. Tinkham. *Introduction to Superconductivity*. Dover Publications, 2015.

[132] K. Uematsu and H. Kawamura. Randomness-Induced Quantum Spin Liquid Behavior in the $s = 1/2$ Random-Bond Heisenberg Antiferromagnet on the Pyrochlore Lattice. *Phys. Rev. Lett.* 123 (8 July 2019), 087201.

[133] Y. J. Uemura, T. Yamazaki, D. R. Harshman, M. Senba, and E. J. Ansaldo. Muon-spin relaxation inAuFe andCuMn spin glasses. *Physical Review B* 31(1) (1985), 546–563.

[134] Y. Uemura. Zero-field muon spin relaxation reflecting dynamics of spin glass. *Solid State Communications* 36(4) (1980), 369–372. ISSN: 0038-1098.

[135] T. J. Williams. Electronic and Magnetic Properties of Ba(Fe,Co)2As2 and URu2Si2. PhD thesis. 2013.

[136] A. S. Wills, M. E. Zhitomirsky, B. Canals, J. P. Sanchez, P. Bonville, P. D. de Réotier, and A. Yaouanc. Magnetic ordering in Gd2Sn2O7: the archetypal Heisenberg pyrochlore antiferromagnet. *Journal of Physics: Condensed Matter* 18(3) (Jan. 2006), L37–L42.

[137] M. N. Wilson. Muon Spin Rotation Studies of URu2Si2 and Dichalcogenide Superconductors. PhD thesis. 2017.

[138] J. Xu, V. K. Anand, A. K. Bera, M. Frontzek, D. L. Abernathy, N. Casati, K. Siemensmeyer, and B. Lake. Magnetic structure and crystal-field states of the pyrochlore antiferromagnet $Nd_2Zr_2O_7$. *Phys. Rev. B* 92 (22 Dec. 2015), 224430.

[139] J. Xu, O. Benton, V. K. Anand, A. T. M. N. Islam, T. Guidi, G. Ehlers, E. Feng, Y. Su, A. Sakai, P. Gegenwart, and B. Lake. Anisotropic exchange Hamiltonian, magnetic phase diagram, and domain inversion of $Nd_2Zr_2O_7$. *Phys. Rev. B* 99 (14 Apr. 2019), 144420.

[140] J. Xu, O. Benton, A. T. M. N. Islam, T. Guidi, G. Ehlers, and B. Lake. Order out of a Coulomb Phase and Higgs Transition: Frustrated Transverse Interactions of $Nd_2Zr_2O_7$. *Phys. Rev. Lett.* 124 (9 Mar. 2020), 097203.

[141] J. Xu, A. T. M. N. Islam, I. N. Glavatskyy, M. Reehuis, J.-U. Hoffmann, and B. Lake. Field-induced quantum spin-$\frac{1}{2}$ chains and disorder in $Nd_2Zr_2O_7$. *Phys. Rev. B* 98 (6 Aug. 2018), 060408.

[142] J. Xu. Magnetic properties of rare earth zirconate pyrochlores. PhD thesis. 2017.

[143] Z. Xue, X. Wang, M. Shi, H. Yu, X. Zhang, and S. Zhang. *Thermal Conductivity and Sintering Behavior of Sm2Zr2O7 Ceramics with Y3+ Substitution for Different Lattices*. 2021.

[144] S. Yamashita, Y. Nakazawa, M. Oguni, Y. Oshima, H. Nojiri, Y. Shimizu, K. Miyagawa, and K. Kanoda. Thermodynamic properties of a spin-1/2 spin-liquid state in a -type organic salt. *Nature Physics* 4(6) (2008), 459–462.

[145] A. Yaouanc, P. Dalmas de Réotier, A. Bertin, C. Marin, E. Lhotel, A. Amato, and C. Baines. Evidence for unidimensional low-energy excitations as the origin of persistent spin dynamics in geometrically frustrated magnets. *Phys. Rev. B* 91 (10 Mar. 2015), 104427.

[146] A. Yaouanc, P. D. D. Réotier, V. Glazkov, C. Marin, P. Bonville, J. A. Hodges, P. C. M. Gubbens, S. Sakarya, and C. Baines. Magnetic Density of States at Low Energy in Geometrically Frustrated Systems. *Physical Review Letters* 95(4) (2005).

[147] L. R. Yaraskavitch, H. M. Revell, S. Meng, K. A. Ross, H. M. L. Noad, H. A. Dabkowska, B. D. Gaulin, and J. B. Kycia. Spin dynamics in the frozen state of the dipolar spin ice material Dy2Ti2O7. *Physical Review B* 85(2) (2012).

[148] T. Yavors'kii, T. Fennell, M. J. P. Gingras, and S. T. Bramwell. $Dy_2Ti_2O_7$ Spin Ice: A Test Case for Emergent Clusters in a Frustrated Magnet. *Phys. Rev. Lett.* 101 (3 July 2008), 037204.

[149] T. Yavors'kii, T. Fennell, M. J. P. Gingras, and S. T. Bramwell. Dy2Ti2O7Spin Ice: A Test Case for Emergent Clusters in a Frustrated Magnet. *Physical Review Letters* 101(3) (July 2008). ISSN: 1079-7114.